Backstress governs transient postseismic creep in the continental lithospheric mantle

Sheng Fan[1,2,3], Thomas Breithaupt[2], Claudia A. Trepmann[4], David Wallis[2]

[1]Center for High Pressure Science and Technology Advanced Research (HPSTAR), Beijing 100193, P. R. China

[2]Department of Earth Sciences, University of Cambridge, Cambridge CB2 3EQ, United Kingdom

[3]Department of Geology, University of Otago, Dunedin 9016, New Zealand

[4]Department of Earth and Environmental Sciences, Ludwig-Maximilians-Universität München, Munich 80333, Germany

Correspondence: Sheng Fan (sheng.fan@hpstar.ac.cn)

Abstract

Understanding the physical processes that control how the continental lithospheric mantle responds to sudden stress changes during the earthquake cycle is essential for interpreting postseismic deformation and constraining the rheological behaviour of the mantle. Laboratory studies have revealed that long-range elastic interactions among dislocations generate backstresses that strongly influence the mechanical response of olivine during transient creep, and the relevance of this mechanism to natural contexts can be confirmed by analysing the stress fields of dislocations in various tectonic settings. Here, we examine peridotites from the Finero Complex in the Ivrea-Verbano Zone, European Alps, which preserve microstructures formed during transient, earthquake-related deformation in a slice of exhumed continental lithospheric mantle. High-angular resolution electron backscatter diffraction reveals pronounced intragranular stress heterogeneity in olivine, with stresses varying by hundreds of megapascals over length scales on the order of 1–10 μm and correlated with elevated densities of geometrically necessary dislocations. These observations demonstrate that long-range dislocation interactions occur in naturally deformed olivine of the continental lithospheric mantle. Superimposing the grain size-stress data on deformation-mechanism maps indicates that a burst of dislocation glide dominates immediately after a stress increase, whereas both dislocation-mediated deformation and diffusion creep contribute at steady state, with diffusion creep relatively more important in finer-grained domains. These inferences are consistent with variations in intragranular substructure and crystallographic preferred orientation. Having demonstrated that long-range elastic interactions contribute to transient creep of the continental lithospheric mantle, we use a dislocation-based microphysical to explore the characteristics of such transients in contexts similar to those represented by the Finero peridotite. This analysis indicates that an earthquake-induced stress increase produces a short-lived reduction by 2–3 orders of magnitude in viscosity followed by progressive restrengthening as backstress builds up over plastic strains on the order of 10^{-3}. These results demonstrate that time-dependent microphysical models, rather than flow laws constructed for steady state alone, are required to describe the postseismic evolution of mantle viscosity.

Plain Language Summary

Earth's mantle does not only respond instantly to the stress changes caused by large earthquakes. Instead, it deforms over time, and understanding this behaviour is essential for interpreting how the mantle relaxes

after earthquakes. In this study, we examined peridotite rocks that once experienced earthquake-related deformation and were brought to Earth's surface from the mantle in the Western Alps. Using electron-microscopy techniques, we mapped distortions of the crystal structure of olivine, the dominant mineral in the upper mantle. These measurements reveal that the olivine crystals contain abundant dislocations, which are defects in the crystal structure that distort the crystal and thereby generate stresses. We also estimated the stresses applied to the bulk rock from the grain sizes of different rock types and compared them with theoretical models of how olivine deforms. The result shows that immediately after a sudden stress increase, deformation is controlled by the motion of dislocations. We then used a microphysical model to predict how the mantle would respond to an earthquake-like stress change. The model predicts that the mantle becomes briefly weaker and flows faster just after an earthquake, before gradually strengthening again as internal stresses rebuild. Our findings show that the upper mantle can experience short-lived weakening after seismic events, and that this behaviour is controlled by the way dislocations interact inside olivine grains.

Key points

1. Microscopic stress heterogeneity in mantle rocks shows that long-range dislocation interactions control transient creep after earthquakes.

2. After sudden stress increases, mantle rocks briefly weaken, then gradually strengthen as internal stresses increase.

3. Models that include strain- and time-dependent dislocation processes better explain post-seismic mantle flow than do steady-state laws.

1. Introduction

Earthquake cycles impose rapid changes in stress state that potentially extend across the full thickness of the lithosphere (Avouac, 2015; Campbell & Menegon, 2019; Ellis & Stöckhert, 2004; Hentschel et al., 2022; Hetland & Simons, 2010; Muto et al., 2019; Nüchter & Ellis, 2010; Wang et al., 2012). Experiments performed on a wide variety of materials demonstrate that stress changes induce transient creep, which manifests as evolution in viscosity as a function of strain towards a steady-state value (e.g., Andrade, 1910; Duval et al., 1983; Fan et al., 2020, 2021a; Glen, 1952; Hansen et al., 2019, 2021; Trepmann et al., 2013; Trepmann & Seybold, 2019; Weertman, 1978; Weertman & Weertman, 1975). Consequently, transient creep is a fundamental process in the evolution of the rheological behaviour of the lithosphere following major earthquakes (Ellis & Stöckhert, 2004; Masuti et al., 2016; Muto et al., 2019).

Flow laws, which are key to modelling the rheological behaviours of mantle flow, reflect our understanding of the physical processes involved in deformation (Breithaupt et al., 2023; Hansen et al., 2011; Hirth & Kohlstedt, 2003; Yabe et al., 2020). Many large-scale geodynamic models developed for predicting the postseismic rheological behaviour of the mantle are based on modified versions of steady-state flow laws (e.g., Masuti et al., 2016; Muto et al., 2019). Although frequently used, the relevance of steady-state flow laws for describing transient postseismic creep has been questioned by both the experimental and geodetic modelling communities as the rate-limiting microphysical processes likely

differ between transient and steady-state creep (e.g., Freed et al., 2010; Hansen et al., 2021; Nüchter & Ellis, 2010; Wallis et al., 2021).

The mechanical behaviours and microstructures of rocks provide information that is key to deciphering the processes associated with transient creep (Hansen et al., 2021; Hanson & Spetzler, 1994; Karato, 2008; Matysiak & Trepmann, 2015; Wallis et al., 2021, 2022; Wiesman et al., 2024). Laboratory experiments often reveal a decrease in the apparent viscosity of olivine-rich rock following a change in applied stress (Chopra, 1997; Hansen et al., 2021; Hanson & Spetzler, 1994; Misra & Murrell, 1965; Post, 1977; Smith & Carpenter, 1987). Moreover, Hansen et al. (2021) observed transient, time-dependent reverse strain following stress reductions during uniaxial compression of single crystals of olivine, revealing the influence of an internal backstress that acts in opposition to the stress driving deformation. Microstructural analyses of the deformed olivine from these experiments, along with a range of other deformation experiments on polycrystalline olivine samples, revealed highly heterogeneous distributions of intragranular residual stress generated by dislocations (Hansen et al., 2021; Wallis et al., 2017, 2020, 2021; Wiesman et al., 2024). This intragranular stress heterogeneity causes long-range elastic interactions among dislocations that generate backstress and thereby result in a specific type of transient creep termed kinematic hardening (Hansen et al., 2019, 2021; Wallis et al., 2017, 2020, 2021). Motivated by these observations, Breithaupt et al. (2023) developed a quantitative framework for the deformation of olivine based upon the evolution of dislocation density and associated backstress, which captures the key characteristics of both transient creep and steady-state flow.

Following these developments, an important next step is to explore the relevance of the backstress model to transient creep in nature. Wallis et al. (2022) demonstrated that olivine in peridotite from the oceanic lithosphere in the paleosubduction interface of the Oman-UAE ophiolite exhibits intragranular stress heterogeneity with characteristics similar to that developed in experimental samples. They used these observations to justify using the backstress model to predict instantaneous changes in viscosity across step changes in stress. However, there has been limited testing for the presence or characteristics of intragranular stress heterogeneity in samples with microstructural evidence for stress pulses caused by nearby earthquakes. Likewise, the characteristics of intragranular stress heterogeneity in olivine in peridotites from the continental lithosphere remain unconstrained. Furthermore, whilst Breithaupt et al. (2023) used their backstress model to predict the strain/time-dependent evolution of viscosity during transient creep for a generalised case in the lower lithosphere and asthenosphere, no studies have used the backstress model to investigate the strain/time-dependent evolution of viscosity constrained by observations from a specific geological example from the shallow lithosphere.

In this contribution, we address these points by providing microstructural observations of olivine from the Finero peridotite, Italy, to constrain the microphysical processes that contribute to the transient creep of the lithospheric mantle during postseismic deformation. In particular, we use high-angular resolution electron backscatter diffraction (HR-EBSD, Wallis et al., 2019; Wilkinson et al., 2006) to map densities of geometrically necessary dislocations (GND) and intragranular stress heterogeneity. These data test for the presence of long-range intragranular stress heterogeneity generated by dislocations to assess the relevance of the backstress model. Based on the microstructural observations, we use the backstress model of Breithaupt et al. (2023) to predict the time-dependent evolution of viscosity during postseismic transient creep of such rocks in the continental lithospheric mantle.

2. Geological context

We selected samples from well-preserved, unaltered peridotitic shear zones distributed across the Finero Complex within the Ivrea-Verbano Zone (IVZ), Western Italian Alps. Figure 1 summarises the geological context of the IVZ and the internal structure of the southwestern Finero Complex. The IVZ is interpreted to be the former accretionary prism of a subduction zone, in which mantle peridotite was tectonically mixed with metasedimentary rocks within the continental lower to middle crust (Quick et al., 1995). Subsequent post-Hercynian crustal extension, which started at no later than ca. 270–300 Ma (i.e., the Late Carboniferous–Early Permian), was associated with the widespread development of localized high-temperature shear zones (Brodie & Rutter, 1987; Langone et al., 2017; Rutter et al., 1993). The crustal extension and thinning continued through ca. 230–180 Ma (i.e., the Early Triassic–Late Jurassic), during which the microstructure of the peridotite was transformed through deformation in long-lived, seismically active shear zones during exhumation (Brodie & Rutter, 1987; Hodges & Fountain, 1984; Langone et al., 2018; Rutter et al., 1993; Schmid et al., 1987). Previous microstructural, petrological, and geochronological studies have identified three stages of metamorphism under peak to retrograde conditions coeval with ductile and brittle deformation of these shear zones, as follows.

(1) Granulite-facies conditions, at temperatures of 670–830ºC, are indicated by clinopyroxene-orthopyroxene thermometry of recrystallized protomylonitic clinopyroxene and orthopyroxene (Altenberger, 1995; Davidson & Lindsley, 1985; Gasparik, 1984; Lindsley, 1983; Wells, 1977). This temperature range is supported by Ti-in-zircon thermometry on magmatic and recrystallized zircons from the Mafic Granulite and Gabbro Unit (Langone et al., 2018).

(2) Amphibolite-facies conditions, at minimum temperatures of 630–650ºC, are indicated by single-pyroxene thermometry of recrystallized ultramylonitic clinopyroxene (Altenberger, 1995; Davidson & Lindsley, 1985). These conditions are consistent with temperatures of 500–650ºC and pressures of 400–600 MPa estimated by Kenkmann (2000) based on amphibole thermobarometry (Laird & Albee, 1981) and plagioclase–hornblende thermometry (Spear, 1980).

(3) Greenschist-facies conditions are constrained to temperatures less than 520ºC by the upper stability limit of antigorite coexisting with tremolite (Altenberger, 1995; Evans & Trommsdorff, 1970; Trommsdorff & Connolly, 1990).

Consequently, the Finero peridotite, the largest of the ultramafic lenses in the IVZ that were exhumed and cooled during the post-Hercynian crustal extension, preserves key microstructural records of shear-zone activity in peridotite under retrograde metamorphic conditions.

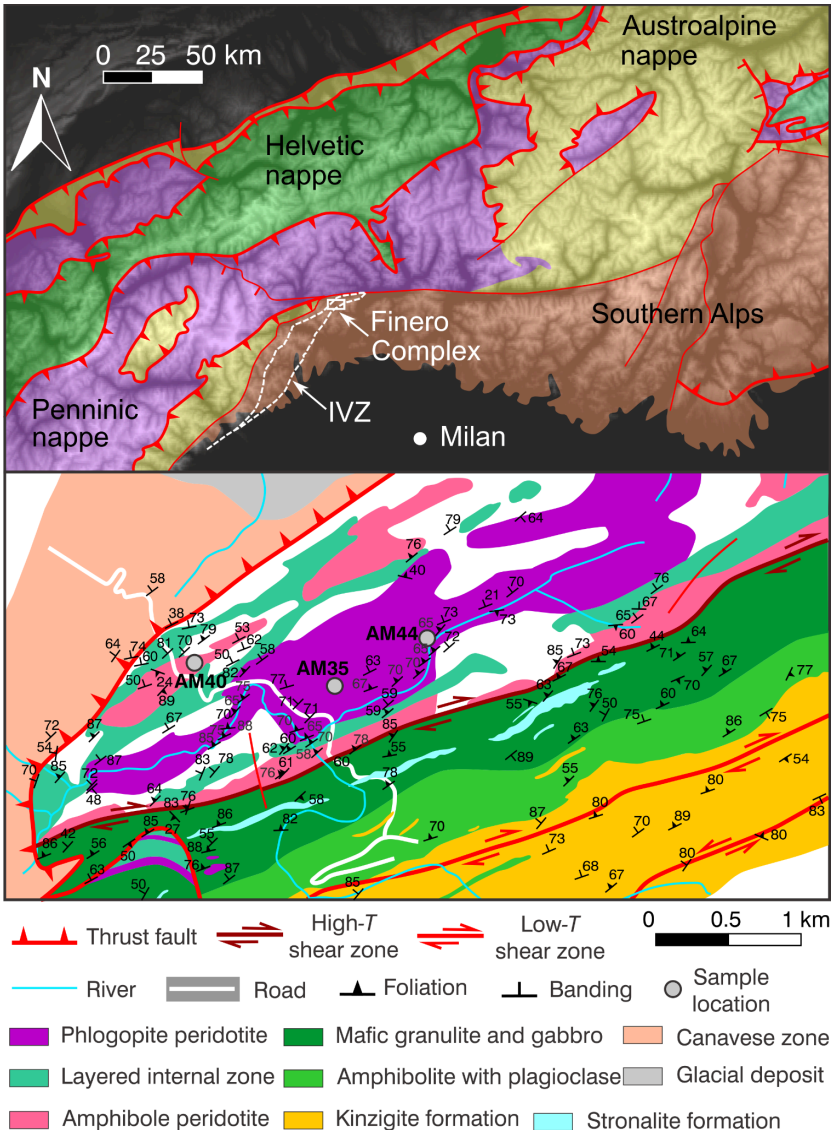

Figure 1. (a) Geological map of part of the Western Alps (modified after Neubauer, 2014) overlaid on a terrain elevation map with a horizontal resolution of 30 arc-seconds (Danielson & Gesch, 2011). White dashed lines indicate the extent of the Ivrea-Verbano Zone (IVZ); the white rectangle marks the location of the Finero Complex. **(b)** Geological map of the Finero Complex modified after Biedermann et al. (2020), Boriani (1995), Corvò et al. (2020), Giovanardi et al. (2014), Matysiak & Trepmann (2015), and Tommasi et al. (2017). Sample locations are from Matysiak & Trepmann (2015).

We use peridotite samples that were previously analysed by Matysiak & Trepmann (2015). These samples, including undeformed and deformed peridotites, were collected from or close to largely unaltered, outcrop-scale peridotitic shear zones distributed within an area of approximately 2 km^2 from the peridotite massif at the core of the Finero Complex (Fig. 1b; Matysiak & Trepmann, 2015). This core is mainly comprised of three lithological units; the Phlogopite Peridotite Unit (purple), the Layered Internal Zone (mint green), and the Amphibole Peridotite Unit (pink) (Fig. 1b) (Cawthorn, 1975; Vogt, 1962). These central units are bounded by the Insubric Fault Zone to the N-NW and the Mafic Granulite and Gabbro Unit (dark green) to the S-SE (Fig. 1b) (Giovanardi et al., 2014; Matysiak & Trepmann, 2015;

Rutter et al., 1993; Tommasi et al., 2017). Each lithological unit has subvertical contacts and contains widespread internal structures, such as layering/banding and/or foliation (Fig. 1b) (Biedermann et al., 2020; Boriani, 1995; Corvò et al., 2020; Matysiak & Trepmann, 2015; Tommasi et al., 2017). Two of the peridotite samples used in this study (AM35, AM44) were collected from the >500 m-thick Phlogopite Peridotite Unit, which exhibits decimeter-scale zones of ultramylonite (Giovanardi et al., 2014). This unit is predominantly composed of olivine (>85% by volume) along with diopside, enstatite, phlogopite, spinel, magnetite, and amphibole (Cawthorn, 1975; Vogt, 1962). The other sample (AM40) was collected from the Amphibole Peridotite Unit and Layered Internal Zone (Fig. 1b). The ~400 m-thick Amphibole Peridotite Unit is characterized by an absence of phlogopite, and a greater content of amphibole compared with the Phlogopite Peridotite Unit (Cawthorn, 1975; Vogt, 1962). The Layered Internal Zone has a thickness of 70–120 m and consists mainly of garnetiferous hornblendites, associated with garnet-bearing amphibole gabbros, anorthosites, pyroxenites, and peridotites in decreasing order of abundance (Giovanardi et al., 2014). Compared with the Amphibole Peridotite Unit and the Phlogopite Peridotite Unit, the Layered Internal Zone generally has less peridotite and pyroxenite (Giovanardi et al., 2014).

Matysiak & Trepmann (2015) conducted detailed microstructural analyses on seven samples, collected from the core of the Finero Complex (Fig. 1b), that consist of host-rock peridotite, along with protomylonitic, mylonitic, and ultramylonitic peridotite. Petrographic and electron backscatter diffraction (EBSD) data revealed contrasts in grain size and/or grain shape among different domains of the Finero peridotite (Matysiak & Trepmann, 2015), as follows.

(1) The host rock probably represents the original mantle peridotite and was annealed at a temperature of ~1000°C and a pressure of ~1 GPa (Lu et al., 1997; Siena & Coltorti, 1989). The host rock exhibits a homogeneous, foam-like structure with grain sizes (area-equivalent diameters) generally larger than 1 mm.

(2) Protomylonite is characterized by spatially localized aggregates of small grains (50–500 μm) that are present along sutured grain boundaries of large porphyroclasts or kink-band boundaries. Small grains and porphyroclasts exhibit intragranular distortion as deformation bands, kink bands, and subgrain boundaries. These microstructures indicate that the protomylonitic microstructure was formed by dislocation-mediated deformation and incipient dynamic recrystallization.

(3) Mylonite has an average grain size of ~100 μm and isolated millimetric porphyroclasts. The grain-size refinement is inferred to have occurred by dynamic recrystallization similar to, but more complete than, that affecting the protomylonite. The mylonitic matrix has a foam-like structure suggestive of possible static annealing after dynamic recrystallization.

(4) Ultramylonite is characterized by bands of aggregates of finer grains, with grain sizes of approximately 5–30 μm, that are distributed along the sutured grain boundaries of coarser grains (>50 μm).

The microstructural contrasts amongst annealed mylonite and strongly deformed protomylonite (and possibly ultramylonite) suggests spatially inhomogeneous, localised deformation, which likely reflects transient deformation related to multiple seismic cycles (Matysiak & Trepmann, 2015). Therefore, peridotite samples from Matysiak & Trepmann (2015) have the potential to preserve key microstructural signals related to the underlying mechanisms of transient creep of olivine in lithologies typical of the continental lithospheric mantle.

3 Microstructural analytical method

We focus on thin sections from three Finero peridotite samples: (1) AM35, containing host rock, (2) AM40, containing protomylonite, and (3) AM44, containing domains of protomylonite, mylonite, and ultramylonite. We repolished thin sections from Matysiak and Trepmann (2015) with 0.03 μm colloidal silica.

3.1 Conventional EBSD

3.1.1 EBSD data collection

We collected EBSD data from the thin sections using a Zeiss Gemini 300 scanning electron microscope with an Oxford Instruments Symmetry EBSD detector and AZtec 4 acquisition software at the University of Cambridge. We coated the thin sections with ~3 nm of carbon prior to EBSD data collection to reduce charging and acquired data under high vacuum at an accelerating voltage of 30 kV. We collected EBSD datasets from the host rock (AM35), protomylonite (AM40), mylonite (AM44), and ultramylonite (AM44) with step sizes of 30 μm, 11 μm, 2.5 μm, and 1 μm, respectively. All datasets were acquired using a camera gain of 1 and frame averaging of 2. For AM35, patterns were collected in sensitivity mode with 622 × 512 pixels; for AM40 and AM44, resolution mode was used to collect patterns with 1244 × 1024 pixels. The indexing rate of olivine across all datasets was greater than 93%.

3.1.2 EBSD data processing

We processed conventional EBSD data using the MTEX toolbox in MATLAB (Bachmann et al., 2010) with full datasets presented in Supporting Information S1. We identified olivine grains from raw EBSD data using a Voronoi decomposition algorithm (Bachmann et al., 2011) based on a threshold misorientation angle of 10° for grain boundaries. We applied noise reduction by removing clusters of fewer than four pixels with the same orientation that are likely to result from misindexing and by removing poorly constrained grains with <50% indexed pixel coverage.

We quantified the grain size, aspect ratio, and shape preferred orientation (SPO) of olivine. We measured grain size using the area-equivalent diameter, i.e., the diameter of a perfect circle that has the same area as the grain. We measured the aspect ratio from the quotient of the lengths of the long axis and short axis of an ellipse fit to each grain. We removed grains with aspect ratios less than 1.5 for SPO analyses as the angle between a given vector and the long axis of each grain estimated from the fitted ellipse has a low signal-to-noise ratio for grains with a convex hull close to a circle. Using the median grain size for a given domain, we estimated the applied stress with a grain-size piezometer calibrated on experimentally deformed Fo90 using EBSD (Qi et al., 2021).

We identified subgrain boundaries as boundaries with misorientation angles less than 10°. We calculated misorientation axes of subgrain boundaries and displayed them in pole figures in the sample reference frame and in inverse pole figures in the crystal reference frame. We removed subgrain boundaries with misorientation angles less than 2° for this analysis, as misorientation axes calculated from conventional EBSD data are typically imprecise when the associated misorientation angle is small (Fan et al., 2022; Prior, 1999). To visualise the crystallographic preferred orientation (CPO), we plotted one point per olivine grain. To better display the CPO pattern, we contoured the CPO data with a half-width of 7.5° based on multiples of uniform distribution (MUD). We quantified CPO intensity using the M-index (Skemer et al., 2005).

3.1.3 Using grain-boundary sphericity to identify recrystallized grains

We segregated recrystallized grains from remnant grains using grain-boundary sphericity, a method first developed for identifying recrystallized grains in deformed ice samples by Fan et al. (2021b). In brief, we first calculated the grain-boundary sphericity parameter, Ψ, from grain area, A, grain-boundary perimeter, P, and area-equivalent radius, R, following $\Psi = A/PR$, for each grain of olivine. Sphericity, Ψ, ranges between 0.5 for grains that are perfectly circular to 0 for grains with infinitely irregular boundaries. In general, two distinct linear trends are observed in sphericity-grain size space for deformed samples: (1) small grains follow a steep trend where Ψ decreases rapidly with increasing grain size, and (2) grains above a threshold grain size follow a trend where Ψ decreases more gradually with grain size. Decreasing sphericity up to the threshold grain size is interpreted as a signal of newly formed, small, near spherical, recrystallized grains that grow by strain-induced grain-boundary migration (GBM) and thereby develop increasingly irregular grain boundaries (Fan et al., 2021b). The gradual decrease in sphericity at larger grain sizes represents a population of original grains (i.e., remnant grains) that becomes increasingly irregular (at similar rates) due to the operation of dynamic recrystallization (Fan et al., 2021b). Thus, the intersection between these trends provides an approximate practical threshold for discriminating between recrystallized and remnant grains. Linear regression was used to fit the data from each domain, and the intersection of these trends is taken as the grain-size threshold. We report the best-fit threshold and its 95% confidence interval based on the uncertainty of the regression fits.

3.2 High-angular resolution EBSD (HR-EBSD)

We collected 56 additional EBSD datasets from the same thin sections for HR-EBSD analysis following the procedures described by Wallis et al. (2016, 2019). We acquired diffraction patterns using a camera gain of 1 and frame averaging of 30. Testing by Wiesman & Wallis (2026), using the same acquisition settings, indicates that averaging ≥ 10 frames is enough that the addition of more frames makes negligible difference to the results and therefore that the 30 frames used here are more than sufficient. The patterns were saved as 8-bit TIFF images with 1244 × 1024 pixels, at an accelerating voltage of 30 kV and a working distance of 25 mm using an Oxford Instruments Symmetry EBSD camera and AZtec 4 data acquisition software. The microscope-detector system was calibrated for HR-EBSD using a Si-wafer standard following Wilkinson et al. (2006). The position of the pattern centre was calibrated using diffraction patterns collected over a range of detector insertion distances (Maurice et al., 2011). Reference-frame conventions were validated using an approach similar to that of Britton et al. (2016).

We collected maps for HR-ESBD from within individual olivine grains in areas with a near absence of micrometre- to nanometre-scale scratches. For domains with different grain sizes, we utilized different combinations of map sizes and step sizes, with at least 50 × 50 points in each map, to optimise the characterization of substructures and micromechanical states. For the host rock (AM35), we collected 4 datasets with map sizes of 100 × 100 μm or 50 × 50 μm at step sizes of 1 μm or 0.5 μm, respectively. For the protomylonite (AM40), we collected 28 datasets with map sizes of 25 × 25 μm or 12.5 × 12.5 μm at step sizes of 0.5 μm or 0.25 μm, respectively. For the mylonite (AM44), we collected 14 datasets with a map size of 10 × 10 μm at a step size of 0.2 μm. For the ultramylonite (AM44), we collected 10 datasets with a map size of 5 × 5 μm at a step size of 0.1 μm. Three maps collected from the host rock (AM35) and three maps collected from the protomylonite (AM40) contain a few scratches, so data points affected by these scratches were removed.

We processed the raw diffraction patterns following procedures described by Britton & Wilkinson (2012a) and Wallis et al. (2016, 2019a) to calculate elastic-strain heterogeneity and lattice rotations, which we

used to calculate residual-stress heterogeneity and GND densities, respectively. In detail, we selected a high-quality diffraction pattern to be the reference pattern for each EBSD map, then cross-correlated the diffraction patterns from every other point within the EBSD map with the reference pattern. The cross-correlation compares 100 regions of interest, each containing 256 × 256 pixels, within each diffraction pattern to the corresponding region of interest in the reference diffraction pattern. The cross-correlation determines the shift in the position of each region of interest within the diffraction pattern. The deformation gradient tensor is fit to these shifts to characterise the distortion of each diffraction pattern relative to that at the reference point. The deformation gradient tensor was decomposed into the symmetric elastic strain tensor and antisymmetric rotation tensor using an advanced three-step remapping approach (Britton & Wilkinson, 2012b). This approach first estimates infinitesimal rotations through an initial cross-correlation pass, followed by a virtual pattern rotation to better align the test and reference patterns, and concludes with a second cross-correlation pass to more accurately capture elastic strains and fine-tune the rotation measurements. We calculated GND densities from spatial gradients in the components of the rotation tensor using Nye–Kröner analysis (Kröner, 1958; Nye, 1953) according to the method of Wallis et al. (2016). The noise level of GND density revealed by HR-EBSD depends on crystal orientation and step size, and is on the order of 10^{13} m^{-2} for our maps due to their relatively small step sizes (Wallis et al., 2016, 2019). We calculated residual stresses from the elastic strains using Hooke's law with the stiffness tensor of olivine (Abramson et al., 1997; Wallis et al., 2019; Wilkinson et al., 2006). The elastic strains, and hence also the stresses, were measured relative to the unknown strain state at the reference point. To provide an intuitive measure of stress heterogeneity that is independent of the choice of reference point, we normalised each component of the stress tensor, σ_{ij}, by subtracting the mean value of each component of the stress tensor, $\bar{\sigma}_{ij}$, from the measured components at each point within each map (e.g., Mikami et al., 2015; Wallis et al., 2019, 2022). We denote the normalised values as $\hat{\sigma}_{ij}$ and our analysis focuses on this quantity.

3.3 Statistics of stress heterogeneity

We use histograms (Sect. 3.3.1), normal probability plots (Sect. 3.3.2), and the restricted second moments (Sect. 3.3.3) of normalised shear stress, $\hat{\sigma}_{12}$, to quantify the intragranular stress heterogeneity in olivine within each domain. For each domain, the statistics were calculated using $\hat{\sigma}_{12}$ data aggregated from all the corresponding maps (full datasets in Supporting Information S2; Sect. 3.2). We chose $\hat{\sigma}_{12}$ for statistical analyses of stress heterogeneity because $\hat{\sigma}_{12}$ is the component of the stress tensor that is modified the least during the sample sectioning process and, being a shear stress, $\hat{\sigma}_{12}$ is particularly relevant to the glide of dislocations (Wallis et al., 2019).

3.3.1 Probability distributions

We interrogate the normalised stresses by considering their probability distributions. The distribution of probability, *P*, of each component of $\hat{\sigma}_{ij}$ characterises the stress heterogeneity. The distribution of $\hat{\sigma}_{ij}$ is usually characterised by a peak at 0 and tails extending to stresses with greater absolute values (Fig. 2a) (Jiang et al., 2013a; Wallis et al., 2021; Wilkinson et al., 2014). The shape of the distribution can provide information on the cause of the stresses. Measurement noise is typically normally distributed with stresses up to a few tens of megapascals (e.g., dashed black curve, Fig. 2a; c.f., Fig. 8a of Wallis et al., 2022). In contrast, broader distributions, particularly those with non-normal tails of $\hat{\sigma}_{ij}$ extending to greater stress magnitudes (e.g., solid red curve Fig. 2a) are indicative of significant stress heterogeneity arising from dislocations.

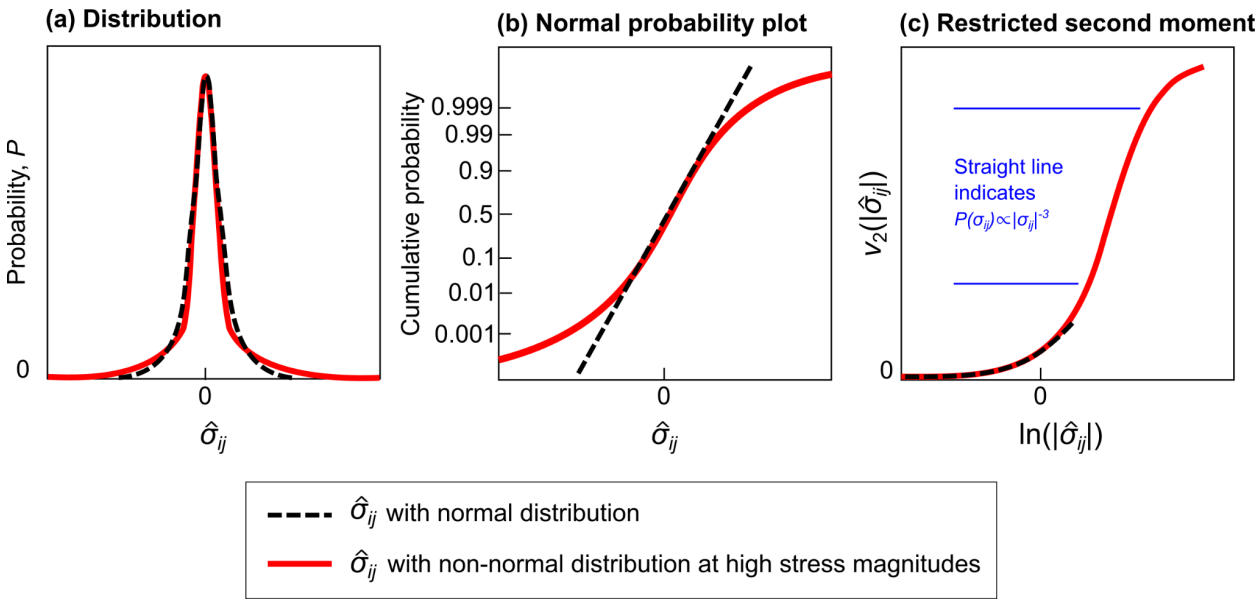

Figure 2. Schematic drawing showing **(a)** the probability distribution of each component of the normalised residual stress tensor, $\hat{\sigma}_{ij}$, **(b)** a normal probability plot of $\hat{\sigma}_{ij}$, and **(c)** the restricted second moment of $|\hat{\sigma}_{ij}|$, $v_2(|\hat{\sigma}_{ij}|)$, as a function of the natural logarithm of $|\hat{\sigma}_{ij}|$, $\ln|\hat{\sigma}_{ij}|$, for idealised stress fields with a perfect normal distribution of $\hat{\sigma}_{ij}$ (dashed black curves) or with a non-normal distribution, in which probability decays as the inverse cube of $\hat{\sigma}_{ij}$ at high stress magnitudes (solid red curves).

3.3.2 Normal probability plot

We further interrogated the form of the probability distribution of $\hat{\sigma}_{ij}$ with a normal probability plot, which allows assessment of whether a distribution follows, or deviates from, a normal distribution (Jiang et al., 2013a; Wallis et al., 2021; Wilkinson et al., 2014). On a normal probability plot, the cumulative-probability axis is scaled such that the cumulative probability falls on a straight line (dashed black line; Fig. 2b) if $\hat{\sigma}_{ij}$ is normally distributed. For deformed crystals containing pronounced stress heterogeneity, the probability distribution of $\hat{\sigma}_{ij}$ usually departs from a straight line at high stress magnitudes indicating that the tails do not follow a normal distribution (compare the solid red curve with the dashed black line in Fig. 2b) (Jiang et al., 2013a; Wallis et al., 2021; Wilkinson et al., 2014).

3.3.3 Restricted second moments of the stress distributions

Residual stress heterogeneity within crystals can be imparted by one or more of several potential causes, including the stress fields of dislocations, changes in pressure and temperature, and chemical reactions of minerals (Holzhausen & Johnson, 1979). We can utilize the probability distribution of each component of the residual stress tensor, $P(\hat{\sigma}_{ij})$, to test whether the stress heterogeneity contains a contribution from the stress fields of dislocations (e.g., Wallis et al., 2021; Wilkinson et al., 2014). If the stress heterogeneity is due to dislocation stress fields, the high-stress portion of the probability distribution $P(\hat{\sigma}_{ij})$ should decay with the cube of the stress, i.e., $P(\sigma_{ij}) \propto |\sigma_{ij}|^{-3}$, and specifically

$$P(\sigma_{ij}) \rightarrow G^2 \, |b|^2 \, C_\sigma \, \langle \rho \rangle \, |\sigma_{ij}|^{-3}, \tag{1}$$

where G is the material dependant shear modulus; $|b|$ is the magnitude of the Burgers vector; ρ is the density of dislocations, and C_σ is the shear contrast factor depending on the types of dislocation, their orientation, and the considered component of σ_{ij} (e.g., Kalácska et al., 2017; Wallis et al., 2021; Wilkinson et al., 2014).

The relation between $P(\sigma_{ij})$ and $|\sigma_{ij}|^{-3}$ can be quantitatively assessed for empirical distributions through the restricted second moment, v_2,

$$v_2(\sigma_{ij}) = \int_{-\sigma}^{+\sigma} P(\sigma_{ij})\, {\sigma_{ij}}^2 \, \mathrm{d}\sigma_{ij}, \tag{2}$$

which quantifies the shape of $P(\sigma_{ij})$ based on the integral over restricted ranges of stress (Wilkinson et al., 2014). If the probability distribution of stress follows $P(\sigma_{ij}) \propto |\sigma_{ij}|^{-3}$, then a plot of v_2 against the logarithm of the corresponding stress component, $\ln|\hat{\sigma}_{ij}|$, should fall on a straight line (Kalácska et al., 2017; Wallis et al., 2021; Wilkinson et al., 2014). Consequently, the straight form of the plot of $v_2(|\hat{\sigma}_{ij}|)$ versus $\ln|\hat{\sigma}_{ij}|$ can be used to identify the presence of stress fields generated by dislocations (Fig. 2c).

3.4 Oxidation decoration

Portions of host rock from sample AM35 and protomylonite from AM44 were prepared for dislocation decoration following the approach of Kohlstedt et al. (1976). Each specimen was heated in air at 900°C for 45 minutes, allowing dislocations within olivine to become decorated by oxidation. Following decoration, the samples have a thin oxidised surface rind, which was removed by polishing with 0.03 µm colloidal silica for ~30 minutes. This step exposed fresh olivine in which the decorated dislocations were retained. To minimise charging during electron imaging, the polished surfaces were coated with ~6 nm of carbon.

The decorated microstructures were examined using forescatter images in a Quanta-650F field emission gun scanning electron microscope equipped with a Oxford Instruments Symmetry S3 EBSD detector at the Department of Earth Sciences in the University of Cambridge. Operating conditions included an accelerating voltage of 30 kV and an aperture size of 100 µm. Image contrast was subsequently adjusted to maximise the visibility of the oxidised dislocations.

4. Results

4.1 Microstructural analysis using visible-light and electron microscopy

We analyse olivine grains from different domains, including host rock, protomylonite, mylonite, and ultramylonite (Figs. 3, 4, 5; Sect. 2). We base our quantitative microstructural analysis on much (> 5 times) larger areas than the maps in Figs. 4 and 5, which are smaller subsets presented for visual clarity. The full maps are available in Supporting Information S1. Microstructures of orthopyroxene, clinopyroxene, and spinel (Figs. 4a, 4f, 5a, 5f), which are also components of the Finero peridotite, are beyond the scope of this paper due to their lesser volume fractions and have been described elsewhere (Matysiak & Trepmann, 2015; Tommasi et al., 2017).

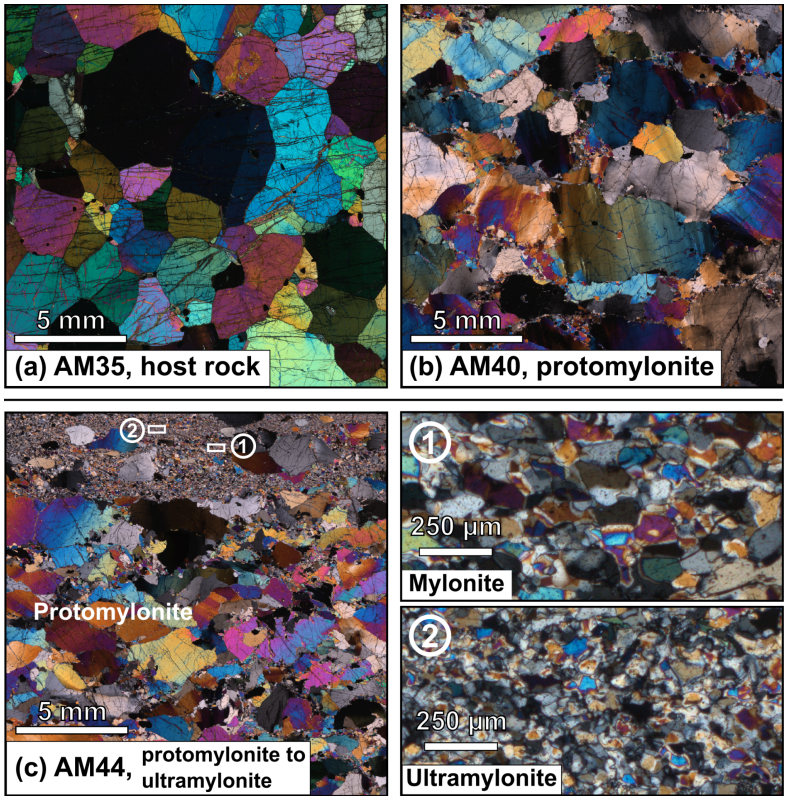

Figure 3. Polarised light photomicrographs (with crossed polarisers) of (**a**) AM35, containing host rock, (**b**) AM40, containing protomylonite, and (**c**) AM44, containing protomylonite, mylonite, and ultramylonite.

4.1.1 Host rock

Olivine grains within the host rock exhibit a foam-like microstructure with straight or slightly curved grain boundaries and polygonal grain shapes (Figs. 3a, 4b, 4c). The SPO of olivine grains with aspect ratios greater than 1.5 is characterised by two maxima at ~90º to each other (Fig. 4b). The distribution of grain sizes on a logarithmic scale is slightly skewed, with a median grain size of ~1100 µm (Fig. 4d). Subgrain boundaries are present within a small fraction of grains (Fig. 4c). The CPO is characterised by distinct orthogonal clusters of [100], [010], and [001] (Fig. 4e). One maximum of long axes in the SPO is approximately parallel to the maximum of [100] in the CPO and the other is approximately parallel to the maximum of [001] (Figs. 4b and 4e). Misorientation axes of subgrain boundaries are distributed between [001] and [010] with the maximum near [001] (Fig. 4e).

4.1.2 Protomylonite

Olivine within the protomylonite consists of large grains with more irregular grain boundaries interlocking with networks of smaller grains with more regular grain boundaries (Figs. 3b, 4g, 4h). The SPO of grains with aspect ratios greater than 1.5 is characterised by a maximum subparallel to the X axis (Fig. 4g). Subgrain boundaries are common (Fig. 4h).

Fig. 4j presents the median value of grain-boundary sphericity against grain size (hollow squares). We first identify two grain-size domains that exhibit distinct sphericity-grain size trends: grains smaller than 200 µm, for which sphericity decreases sharply with increasing grain size, and grains larger than 1000 µm, for which sphericity decreases more gradually with increasing grain size. The best fits to the two

linear trends identified from the sphericity−grain size data intersect at a grain size of 292 μm (thick cross mark; Fig. 4j) and therefore we use this value as a cut-off grain size to segregate recrystallized grains from remnants of original grains. The grain-size distribution of recrystallized grains is close to log-normal with a median grain size of 67 μm (Fig. 4k). This value is similar to a value of 63 μm from the method of Cross et al. (2017). This median grain size corresponds to an estimated differential stress of ~20 MPa (Sect. 3.1.2). Recrystallized grains and remnant grains have similar CPO with [100] subparallel to the X axis and [001] subparallel to the Z axis (Figs. 4g, 4l). The CPO of the remnant grains is stronger than that of the recrystallized grains with values of M-index of approximately 0.12 and 0.06, respectively. Misorientation axes of subgrain boundaries in recrystallized grains are distributed between [001] and [010] with the maximum near [010] (Fig. 4l). Those in remnant grains have maxima near [001] and [010] (Fig. 4l).

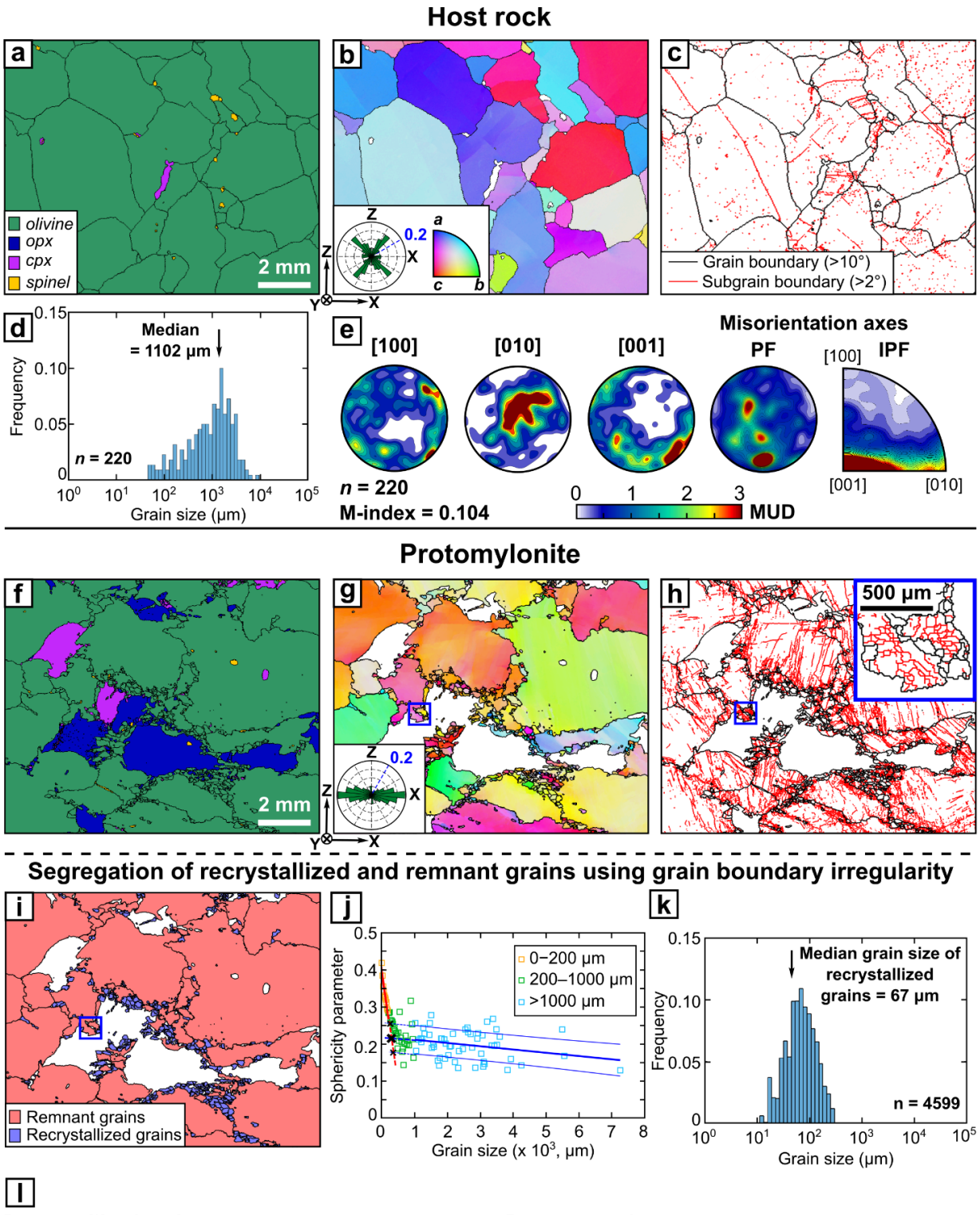
Host rock
a
olivine
opx
cpx
spinel
2 mm
b
Z
X
Y
0.2
a
c
b
c
Grain boundary (>10°)
Subgrain boundary (>2°)
d
Median
= 1102 µm
Frequency
n = 220
Grain size (µm)
e
[100]
[010]
[001]
PF
Misorientation axes
[100] IPF
[001]
[010]
n = 220
M-index = 0.104
0 1 2 3
MUD
Protomylonite
f
2 mm
g
0.2
h
500 µm
Segregation of recrystallized and remnant grains using grain boundary irregularity
i
Remnant grains
Recrystallized grains
j
0–200 µm
200–1000 µm
>1000 µm
Sphericity parameter
Grain size (x 10³, µm)
k
Median grain size of
recrystallized
grains = 67 µm
n = 4599
Frequency
Grain size (µm)
l
Recrystallized grains
[100]
[010]
[001]
Misorientation axes
PF
[100] IPF
[001]
[010]
n = 4599, M-index = 0.059
Remnant grains
[100]
[010]
[001]
Misorientation axes
PF
[100] IPF
[001]
[010]
n = 286, M-index = 0.119

Figure 4. Microstructural analyses of host rock (**a–e**) and protomylonite (**f–l**). Microstructural statistics are based on areas that are much larger than the subareas presented in (**a–c**) and (**f–h**). (**a**) and (**f**) are phase maps. (**b**) and (**g**) are orientation maps, in which the colour map indicates the crystallographic axes that are parallel to a specific direction as shown by the black arrows to the lower left of the box. To clearly illustrate grain orientations, (**b**) is coloured by the inverse pole figure referred to the Y axis, whereas (**g**) is coloured in reference to the Z axis. The SPO of olivine grains with aspect ratios greater than 1.5 is inset in the lower left of each of these subfigures. **(c)** and **(h)** are boundary maps. (**d**) is the grain-size distribution of olivine in host rock plotted on a logarithmic grain-size scale. The median grain size is marked by a black arrow. (**e**) and (**l**) are pole figures of [100], [010], and [001] axes along with pole figures (PF) and inverse pole figures (IPF) of the misorientation axes of subgrain boundaries. (**i**) is a map of recrystallized and remnant olivine grains, which are segregated by the grain-boundary sphericity method (Fan et al., 2021b). (**j**) is a scatter plot of median sphericity parameter, Ψ, for each grain-size interval with a bin width of 20 μm. We fit separate linear relationships between sphericity and grain size for smaller grains (d < 200 μm) and larger grains (d > 1000 μm). Thick lines are linear best fits and thin lines are the upper and lower bounds of the 95% confidence intervals of the fits. Crosses mark the intersections of each of the corresponding lines from different grain-size classes.

4.1.3 Mylonite and ultramylonite

In mylonite, olivine grain boundaries are typically straight or slightly curved, while olivine phase boundaries exhibit more irregular shapes (Figs. 3c, 5a–5c). In ultramylonite, olivine grains have irregular grain boundaries and elongate shapes; also the phase boundaries are irregular (Figs. 3c, 5f–5h). The SPO of olivine grains is characterised by a maximum subparallel to the X axis (Figs. 5b, 5g). Subgrain boundaries are present within a few grains (Figs. 5c, 5h). The grain-size distributions are approximately log-normal with median grain sizes of 31 μm in the mylonite and 16 μm in the ultramylonite (Fig. 5d, 5i), corresponding to estimated stresses of ~40 MPa and ~80 MPa, respectively (Sect. 3.1.2). These stress estimates are upper bounds due to the potential effect of secondary phases pinning grain boundaries and thereby inhibiting grain growth. The CPO of the mylonite is similar to that of the protomylonite, with a maximum of [100] parallel to the X axis, but it is weaker in strength with an M-index of approximately 0.01. The ultramylonite lacks a discernible CPO and has an M-index of 0.005. The misorientation axes of subgrain boundaries in olivine within the mylonite and ultramylonite exhibit near-random distributions (Figs. 5e, 5j).

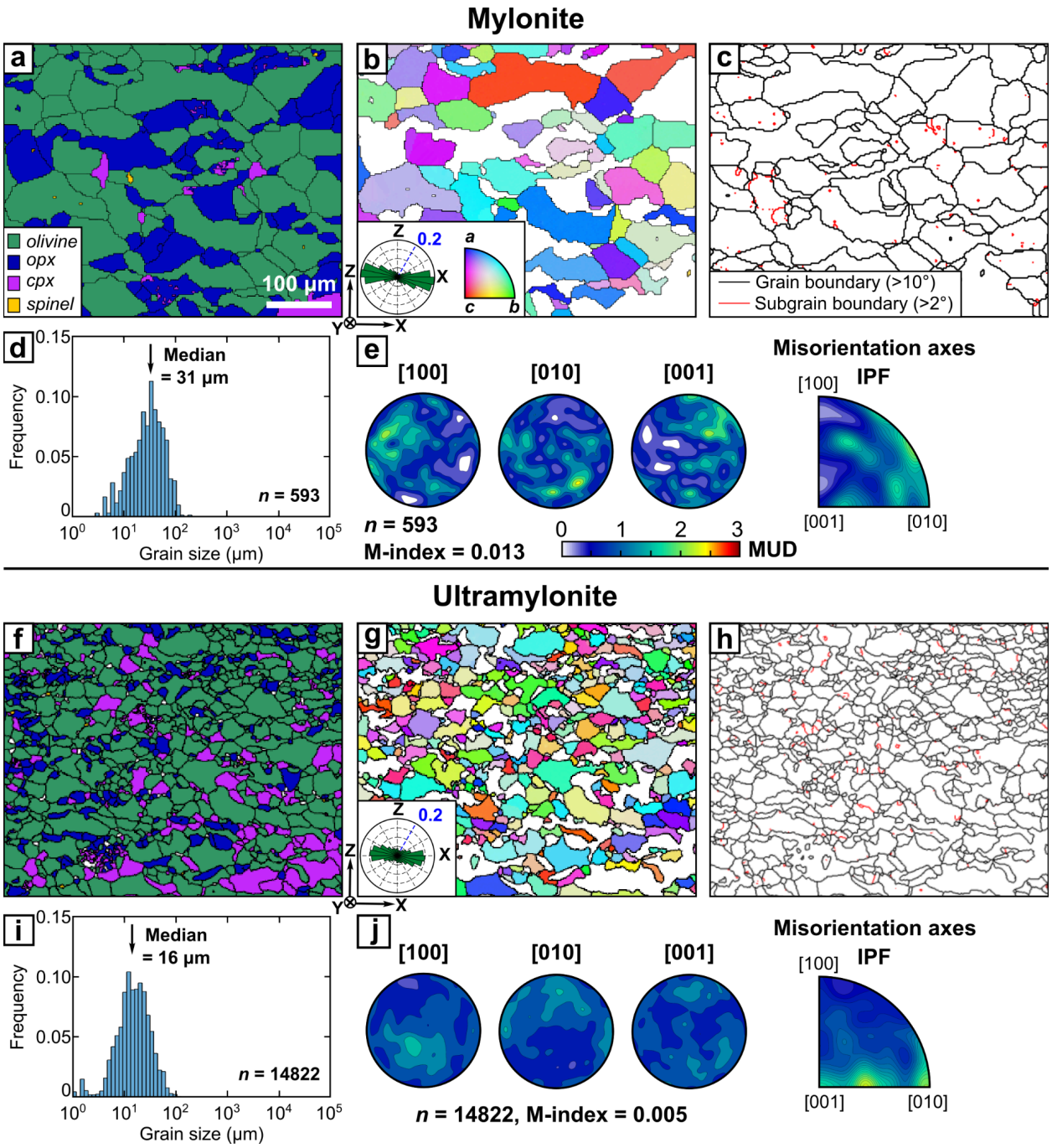

Figure 5. Microstructural analyses of mylonite (**a–e**) and ultramylonite (**f–j**). Descriptions of (**a–e**) and (**f-j**) are the same as the descriptions of (**a-e**) in Fig. 4, except (**b**) and (**g**) are coloured by the inverse pole figure referred to the Z axis.

4.2 Intragranular microstructural and stress analysis from HR-EBSD data

We acquired HR-EBSD maps from 56 areas within host rock, protomylonite, mylonite, and ultramylonite (Sect. 3.2). Figures 6–10 present representative datasets selected to illustrate the range of degrees of intragranular deformation within each rock type. All the HR-EBSD data are available in Supporting Information S2. In each of Figures 6–10, we present (a) forescattered electron images that demonstrate the

surface topography and quality with a small amount of orientation contrast (Britton et al., 2018), (b) maps of the logarithm of the total density of geometrically necessary dislocations (GNDs), (c) maps of each in-plane component of the normalised stress tensor ($\hat{\sigma}_{ij}$), (d) raw diffraction patterns of the reference points (illustrated as pink dots in c) that demonstrate the data quality, and (e) crystal orientations displayed in pole figures.

4.2.1 Densities of geometrically necessary dislocations (GNDs)

The densities and distributions of GNDs in olivine vary between different microstructural domains. Olivine grains in the host rock generally exhibit an apparent GND density below ~10^{13} m^{-2} (Fig. 6b). A few bands with GND densities at 10^{13}–$10^{13.5}$ m^{-2} can be traced within individual grains (e.g., AM35-03, AM35-04; Fig. 6b). The protomylonite contains some grains with low apparent GND densities (close to or less than 10^{13} m^{-2}) (e.g., AM40-10; Fig. 7b. AM40-19; Fig. 8b). However, many other grains in the protomylonite are dissected by discrete bands with elevated GND densities ≥$10^{13.5}$ m^{-2} (Figs. 7b, 8b). These bands are either parallel to each other (e.g., AM40-04, AM40-08; Fig. 7b) or intersect (e.g., AM40-01; Fig. 7b. AM40-13, AM40-16; Fig. 8b). Patches with elevated GND density ($10^{13.5}$–10^{14} m^{-2}) are infrequent but do not contain discrete bands (e.g., AM40-18; Fig. 8b). Olivine grains within mylonite and ultramylonite generally do not exhibit distinct bands with elevated GND densities, but do exhibit more diffuse linear structures locally (e.g., AM44-08, AM44-13; Fig. 9b. AM44-17, AM44-19; Fig. 10b). Instead, the mylonite and ultramylonite exhibit broader areas that have GND densities varying between $10^{13.5}$ and 10^{14} m^{-2} (Figs. 9b, 10b).

4.2.2 Spatial heterogeneity of residual stress

Olivine grains in the host rock exhibit a relatively homogeneous stress distribution, having standard deviations of approximately 40–70 MPa across each map, with occasional stress concentrations (Fig. 6c). In contrast, pronounced stress concentrations within olivine grains are common in the protomylonite, mylonite, and ultramylonite (Figs. 7c–10c). The protomylonite contains many bands of elevated stresses on the order of several hundred megapascals that vary sharply over a few micrometres (e.g., AM40-04, Fig. 7c. AM40-13, AM40-16; Fig. 8c). Many areas within protomylonite, mylonite and ultramylonite contain diffuse (i.e., without a clear linear structure) spatial distributions of smooth stress heterogeneity, with stresses varying by hundreds of megapascals over length scales on the order of 1–10 μm (e.g., AM40-10, Fig. 7c; AM40-18, Fig. 8c; AM44-08, AM44-13, Fig. 9c; AM44-15, AM44-17, Fig. 10c).

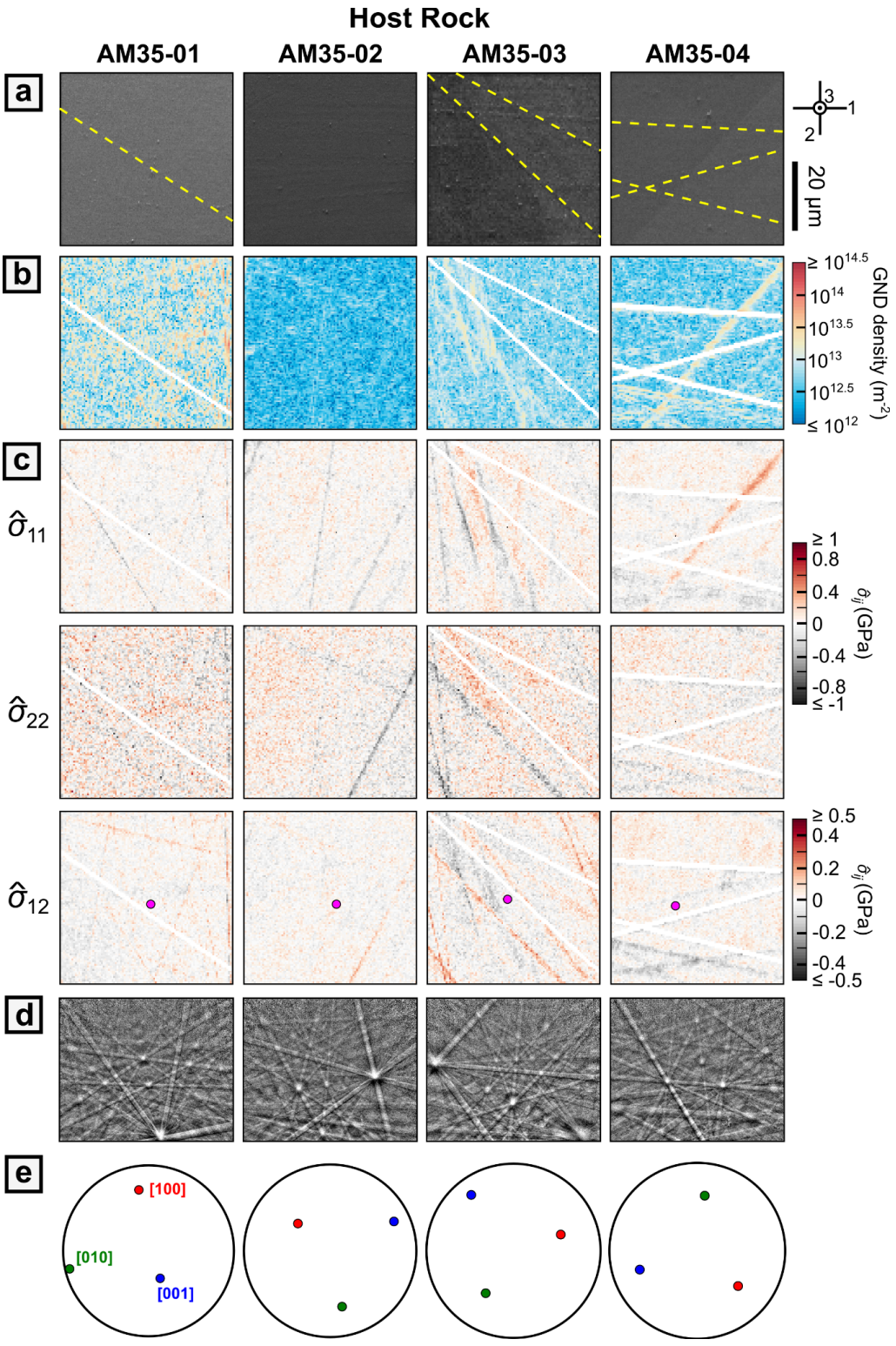

Figure 6. HR-EBSD data collected from the host rock. (**a**) Forescattered electron images. Dashed yellow lines indicate surface scratches with corresponding pixels removed from analyses. (**b**) The logarithm of the total densities of geometrically necessary dislocations (GNDs) estimated from lattice rotations measured by HR-EBSD. (**c**) Maps of each component of the normalised residual stress tensors ($\hat{\sigma}_{11}$,$\hat{\sigma}_{22}$,

and $\hat{\sigma}_{12}$) calculated by subtracting the mean value within each grain. In (**b**) and (**c**), white areas indicate pixels corresponding to surface scratches or pixels that failed the quality criteria for the cross-correlation analysis (Britton & Wilkinson, 2011); these pixels were removed from our analysis. (**d**) Raw diffraction patterns of the reference points (pink dots in (**c**)). (**e**) Pole figures illustrating crystal orientations.

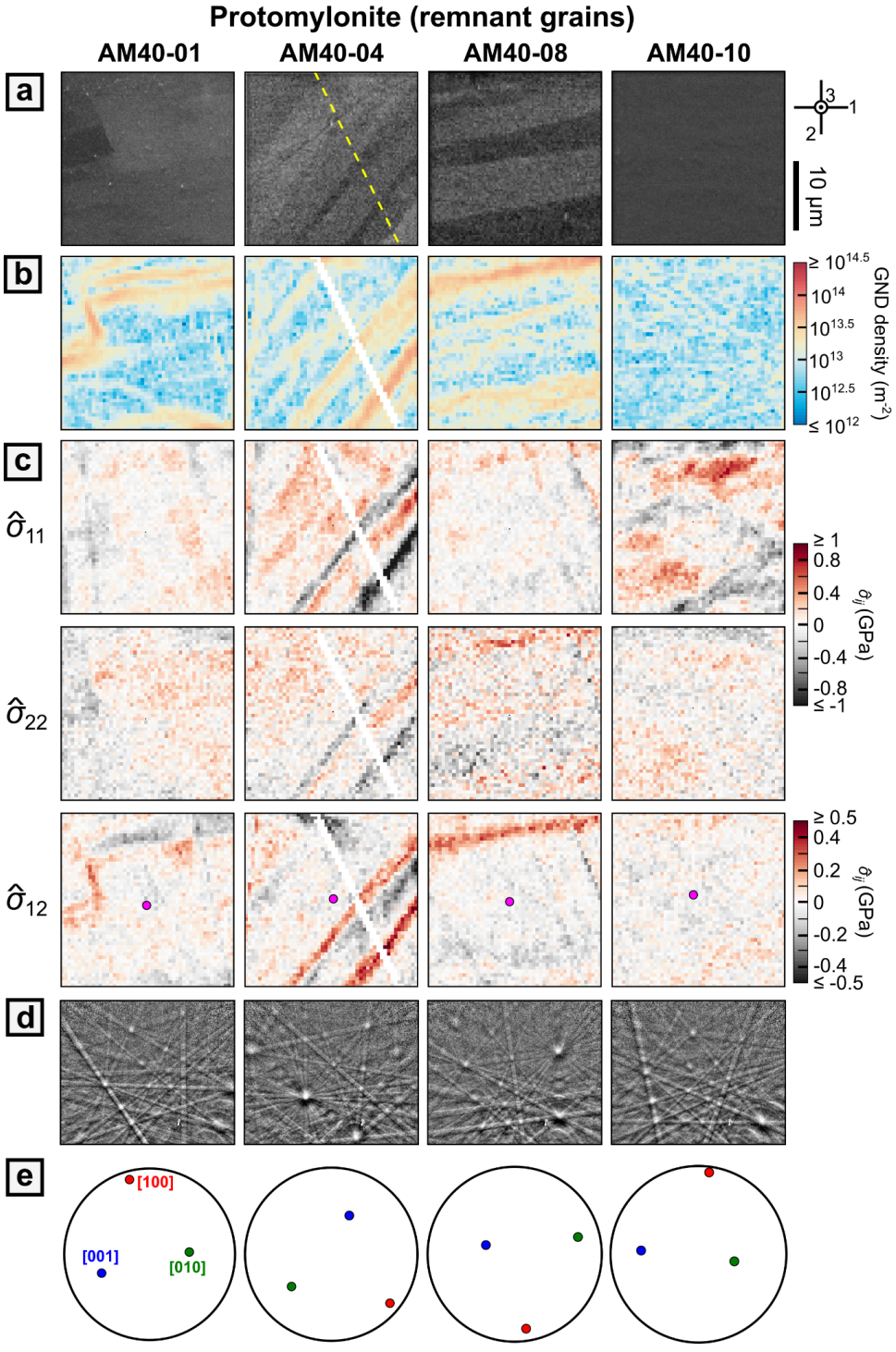

Figure 7. HR-EBSD data collected from the remnant grains within protomylonite (AM40). Descriptions of (**a**)–(**e**) are the same as Fig. 6.

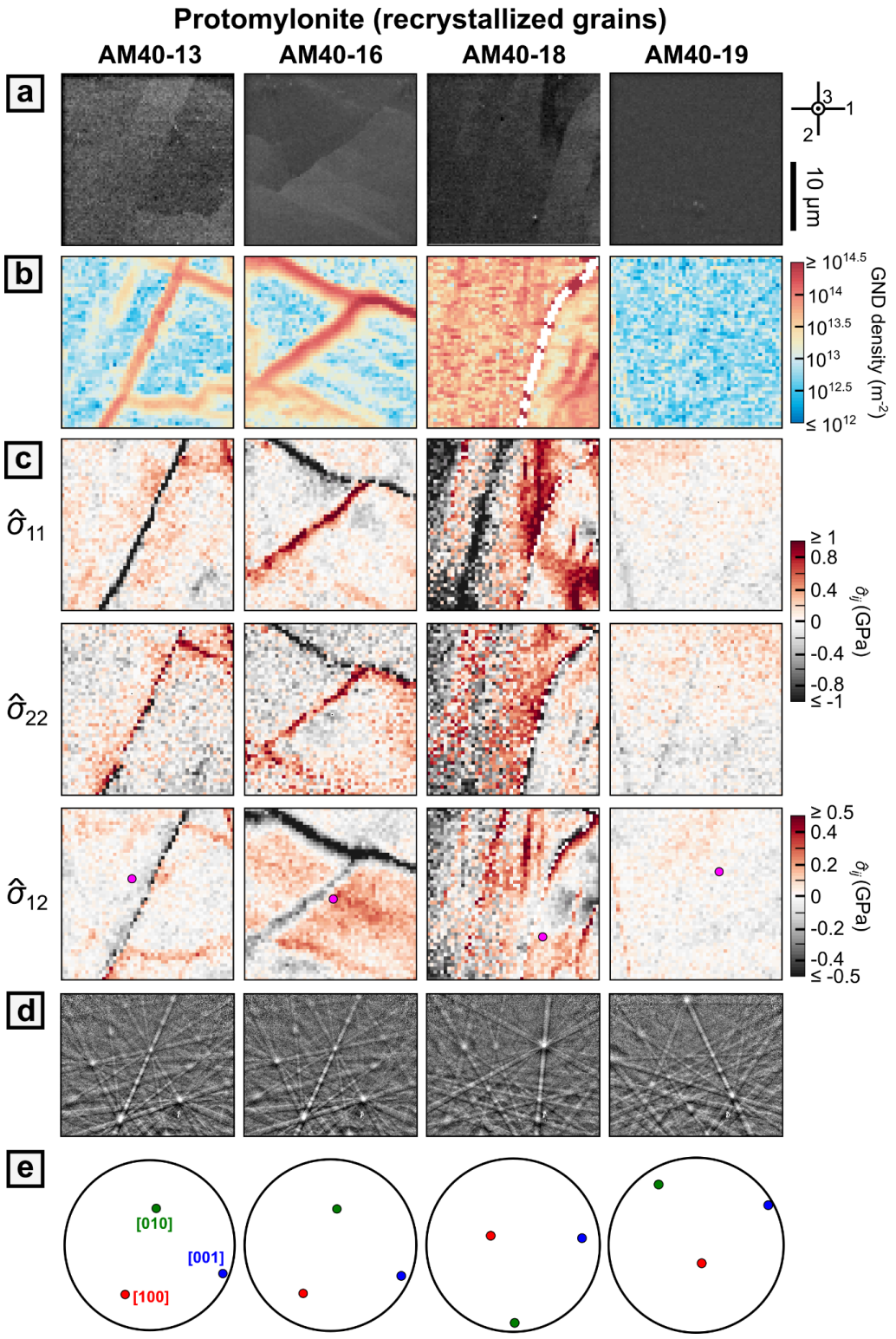

Figure 8. HR-EBSD data collected from the recrystallized grains within protomylonite (AM40). Descriptions of (**a**)–(**e**) are the same as Fig. 6.

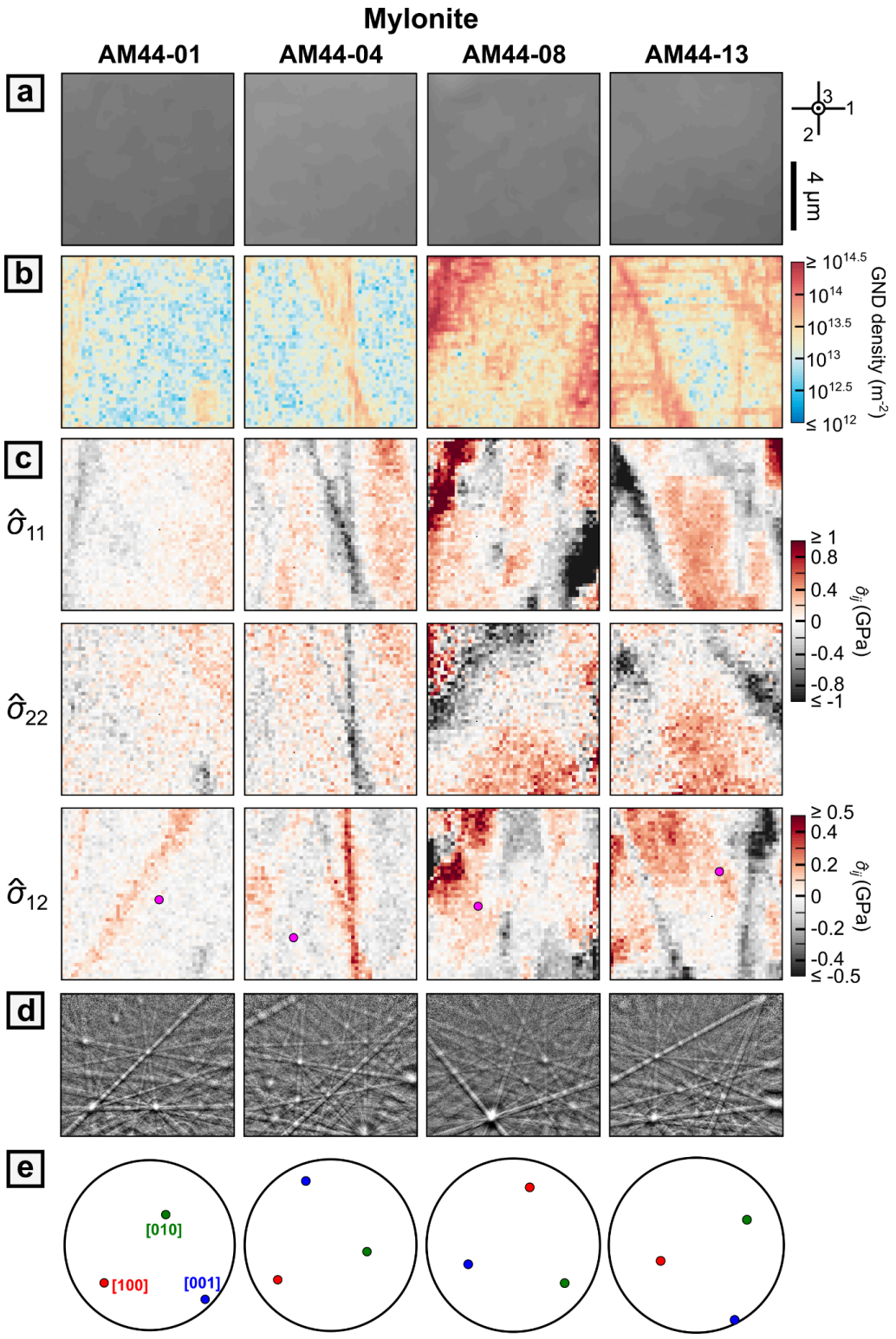

Figure 9. HR-EBSD data collected from the mylonite (AM44). Descriptions of (**a**)–(**e**) are the same as Fig. 6.

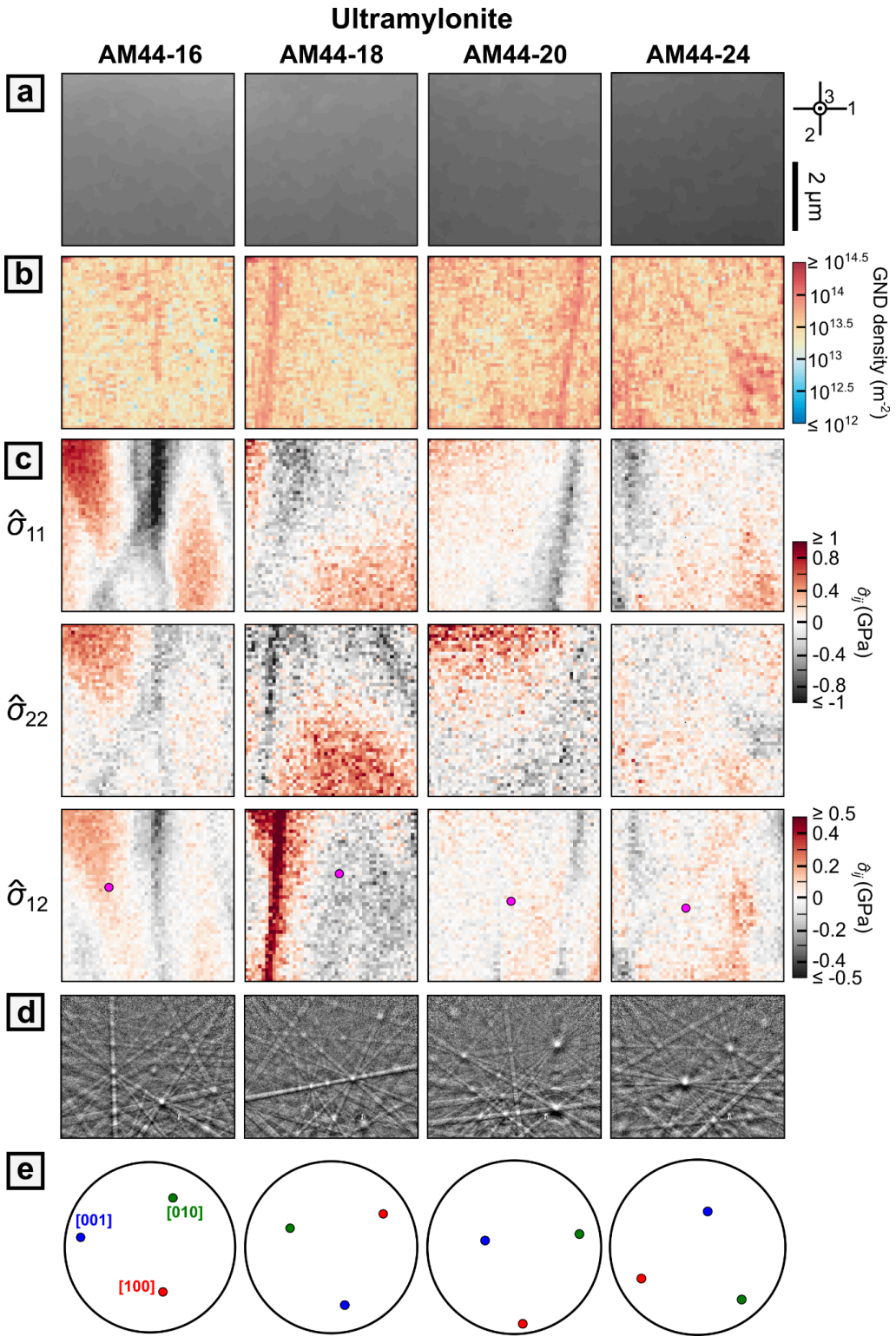

Figure 10. HR-EBSD data collected from the ultramylonite (AM44). Descriptions of (**a**)–(**e**) are the same as Fig. 6.

4.3 Statistics of intragranular stress heterogeneity

Relative to the distribution of $\hat{\sigma}_{12}$ in the host rock, the distributions in the protomylonite, mylonite, and ultramylonite are broader (Fig. 11a). Specifically, the 99th percentile of the distribution of $\hat{\sigma}_{12}$ in the host rock is 150 MPa, whereas those of the more deformed domains are in the range 250–370 MPa (Fig. 11b).

We explore the forms of the distributions of $\hat{\sigma}_{12}$ using normal probability plots and the restricted second moment. Normal probability plots of $\hat{\sigma}_{12}$ (Fig. 11b) exhibit two main characteristics that are common across the data from all domains. First, the distributions of $\hat{\sigma}_{12}$ at magnitudes less than approximately 100 MPa fall on straight lines, indicating that they are well described by normal distributions. Second, in contrast, the tails of the distributions at greater stress magnitudes deviate from the straight lines and extend to greater stress magnitudes than predicted by the normal distributions fit to the data at low stress magnitudes indicated by dashed lines. However, compared with the host rock, the protomylonite, mylonite, and ultramylonite show a greater degree of the deviation of tails away from normal distributions (Fig. 11b). We plot the restricted second moment as a function of the natural logarithm of $|\hat{\sigma}_{12}|$ for all domains in Fig. 11c. The data from each domain follow linear relationships at stress magnitudes greater than ~200 MPa. However, for protomylonite, mylonite, and ultramylonite the straight-line proportion has a gradient that is 4–6 times greater, and extends to greater stress magnitudes, compared with that of the host rock (Fig. 11c).

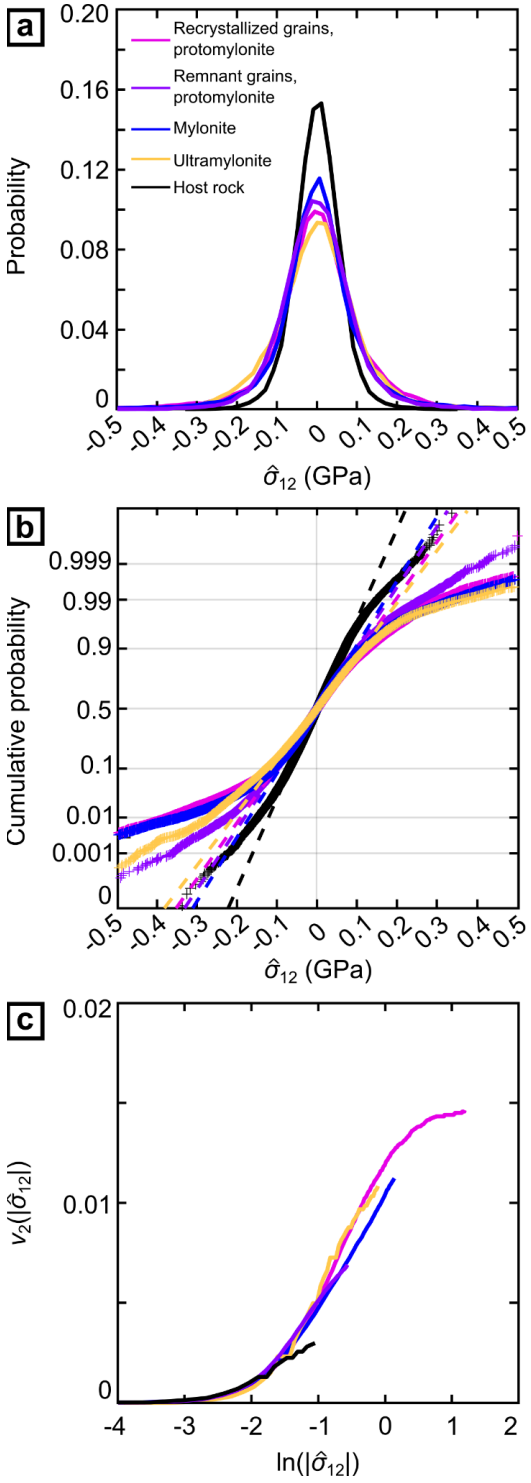

Figure 11. Statistical analyses of normalised shear stress, $\hat{\sigma}_{12}$, for different domains. (**a**) Histograms showing probability distributions of $\hat{\sigma}_{12}$. (**b**) Normal probability plots of $\hat{\sigma}_{12}$. (**c**) Restricted second moment as a function of the natural logarithm of $|\hat{\sigma}_{12}|$.

4.4 Decorated dislocations

Figure 12 presents forescattered electron images of decorated dislocations in olivine from host rock and protomylonite samples. In both lithologies, dislocations are bright dots or short lines with varying orientations, and some occur in subgrain boundaries expressed as linear arrays of closely spaced dislocations. Where dislocations intersect the sample surface at oblique angles, they typically appear as short lines (Figs. 12b and 12f). Both straight and locally curved dislocations are evident, and in some grains they are arranged into alternating bands of higher and lower density across micrometre length scales (Figs. 12c and 12e). Dislocation densities are greater in the protomylonite (Figs. 12c–12f) than in the host rock (Figs. 12a and 12b). The average density of dislocations is 1.7×10^{11} m^{-2} in the host rock, corresponding to an estimated stress of 28 MPa, and is 1.1×10^{12} m^{-2} in protomylonite, corresponding to an estimated stress of 105 MPa.

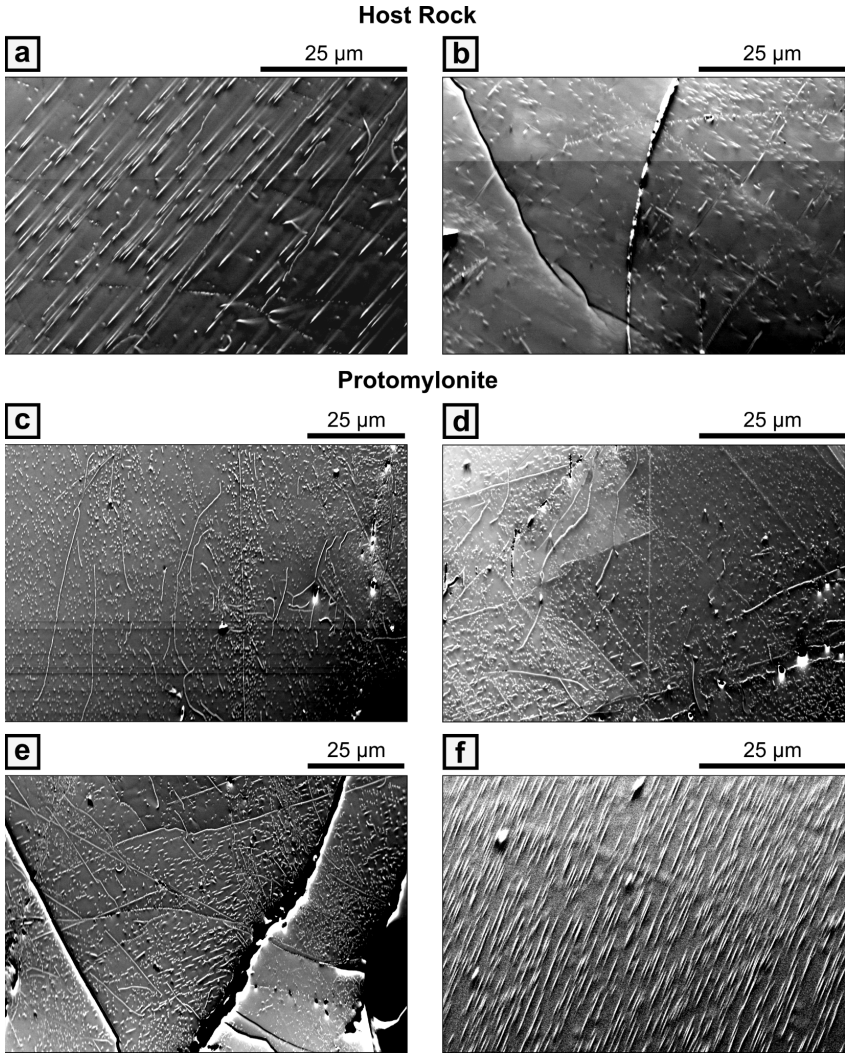

Figure 12. Forescattered electron images of dislocations in olivine decorated by oxidation.

5. Discussion

5.1 Inferences of deformation mechanisms and recrystallization processes

5.1.1 Dislocation-mediated deformation

Dislocation microstructures are pervasive in olivine grains in the Finero peridotite, ranging from the relatively undeformed host rock through protomylonite and mylonite to ultramylonite. Oxidation decoration revealed abundant dislocations in the host rock and protomylonite (Sect. 4.4) and HR-EBSD data reveal GNDs in each microstructural domain (Sect. 4.2.1). Deformation lamellae are also common in the protomylonite (Matysiak & Trepmann, 2015). Likewise, visible-light and EBSD analyses (Sect. 4.1) reveal that subgrain boundaries are present across all domains and reflect recovery processes, by which dislocations rearrange to form lower-energy configurations (Urai et al., 1986). In the host rock, misorientation axes of subgrain boundaries parallel to [001] indicate activity of the (010)[100] slip system during early, high-temperature deformation (Sect. 4.1.1). In contrast, alongside misorientation axes parallel to [001], the protomylonite and mylonite also have misorientation axes of subgrain boundaries parallel to [010] (Sect. 4.1.2 and 4.1.3). Taken together with CPOs that have [100] approximately parallel to the lineation and [001] approximately normal to the foliation (i.e., E-type CPOs, Sect. 4.1.2 and 4.1.3), these observations indicate activity of the [100](001) slip system during deformation of the mylonitic rocks.

Together, these observations support the deformation-history model proposed by Matysiak & Trepmann, (2015). This model suggests that formation of the mylonitic series in the Finero peridotite involved an initial phase of low-temperature plasticity (i.e., dislocation glide) during transient seismic stress pulses, followed by more prolonged dislocation creep during the subsequent postseismic stress relaxation.

5.1.2 Dynamic recrystallization

Olivine grains within protomylonite, mylonite, and ultramylonite have average grain sizes that are smaller than those of the host rock (Figs. 4 and 5; Sect. 4), indicating the operation of grain-size reduction processes (Biedermann et al., 2020; Matysiak & Trepmann, 2015). Olivine grains within the protomylonite have (1) a core-and-mantle structure, i.e., networks of small, recrystallized grains interlocking with large, remnant grains, (2) subgrains, which have sizes similar to those of recrystallized grains, at the margins of remnant grains, and (3) similar CPO between recrystallized and remnant grains (Figs. 4f–4l; Sect. 4.1.2). Previous studies on rock-forming minerals, ice, and metals suggest that core-and-mantle structures, networks of subgrains, and similar CPO between recrystallized and remnant grains are common microstructural signals of subgrain rotation recrystallization (Fan et al., 2020; Halfpenny et al., 2006; Poirier & Nicolas, 1975; Ponge & Gottstein, 1998; Urai et al., 1986; White, 1976). Olivine grains with irregular grain boundaries are common in the protomylonite (Figs. 4, 5; Sects. 4.1.2, 4.1.3; Matysiak & Trepmann, 2015). Irregular grain boundaries are commonly interpreted to result from strain-induced grain-boundary migration (Fan et al., 2020; Hirth & Tullis, 1992; Karato, 1988; Stipp et al., 2010). During strain-induced grain-boundary migration, grain boundaries are driven by intergranular heterogeneity in strain energy to migrate into the adjacent grain with the greatest strain-energy density (Urai et al., 1986). These interpretations of dynamic-recrystallization processes inferred from microstructural observations align with previous studies conducted on the Finero peridotite (Kenkmann & Dresen, 2002; Matysiak & Trepmann, 2015).

5.1.3 Grain-size sensitive deformation mechanisms

The sequence of deformation microstructures suggests a contribution of grain-boundary sliding (GBS) in the finer-grained domains. Olivine within both the host rock and protomylonite exhibits well-defined CPO (Figs. 4e, 4l; Sects. 4.1.1, 4.1.2). For the protomylonite, recrystallized olivine grains have a weaker CPO intensity (here defined as a lower value of M-index) compared to the remnant grains (Fig. 4l; Sect. 4.1.2). Moreover, olivine grains within the mylonite and ultramylonite have CPOs that are close to random, in contrast to protomylonite with a well-defined CPO (Figs. 4l, 5e, 5i; Sects. 4.1.2, 4.1.3). These observations indicate that additional processes and/or deformation mechanisms are progressively more involved in the deformation of the increasingly fine-grained portions of the protomylonite, mylonite, and ultramylonite. Previous studies on minerals have observed recrystallized daughter grains with weaker CPO compared to neighbouring parent grains, and this relationship is commonly interpreted to be the result of subgrain rotation followed by further reorientation during deformation involving GBS (Bestmann & Prior, 2003; Fan et al., 2020; Fliervoet et al., 1997; Jiang et al., 2000; Storey & Prior, 2005; Warren & Hirth, 2006). Deformation that involves GBS and progresses to high strains must also involve motion of point defects (diffusion creep) and/or dislocations (dislocation accommodated grain-boundary sliding, disGBS) to allow shape changes of the grains (Raj & Ashby, 1971). Grain shape and SPO data are not sufficient to distinguish between these additional mechanisms of intracrystalline deformation, because they both can produce grains with elongate shapes and a strong SPO, as is the case in this study (Figs. 4–5; Sects. 4.1.2, 4.1.3; Ashby & Verrall, 1973; Wheeler, 2010). However, diffusion creep often results in a lack of CPO (Ashby & Verrall, 1973; Boullier & Gueguen, 1975), whilst disGBS usually produces a CPO (Hansen et al., 2012). Therefore, the lack of olivine CPO within ultramylonite suggests the operation of diffusion creep in these fine-grained domains (Warren & Hirth, 2006). Overall, the microstructures suggest that progressive grain-size reduction by subgrain-rotation recrystallization caused a progressive switch from dislocation-mediated deformation in the coarser-grained material to an increasing contribution of diffusion creep in the finer-grained domains. Nonetheless, the intragranular substructures observed in the mylonite and ultramylonite, as revealed by the EBSD and HR-EBSD data, indicate that dislocation-mediated deformation still made a partial contribution to strain accommodation in these domains. These constraints enable us to further explore the contribution of dislocation-mediated deformation and diffusion creep to the deformation of Finero peridotite in the following sections.

5.2 Spatial distributions of geometrically necessary dislocations and stress heterogeneity

Olivine grains within protomylonite, mylonite, and ultramylonite generally exhibit greater heterogeneity of GND density and residual stress compared to host rock (compare Figs. 7–10 with Fig. 6; Sect. 4.2). This observation suggests that the dislocation structures, as indicated by areas with elevated GND densities (Figs. 7–10), in protomylonite, mylonite, and ultramylonite result from a distinct phase of deformation and are not inherited from the host rock. Areas containing clear dislocation structures typically have elevated GND densities that are up to ~10^{14} m^{-2} (Figs. 7–10); these magnitudes are close to those of datasets collected from other natural samples (i.e., Oman-UAE ophiolite; Wallis et al., 2022), but are less than those of datasets collected from experimentally deformed samples (< ~10^{15} m^{-2}) (e.g., Wallis et al., 2020, 2021).

We note that our measured GND densities ($10^{13.5}$–10^{14} m^{-2}) are greater than the average dislocation densities (10^{12}–10^{13} m^{-2}; Section 4.4 and Matysiak & Trepmann (2015)) measured by oxidation decoration. Following Wallis et al. (2022) and Wiesman et al. (2024), we provide two explanations to rationalise the difference between GND density and decorated-dislocation density:

(1) Decorated dislocations and GND density measure different populations of dislocations. The densities calculated from decorated dislocations are those of free dislocations within subgrain interiors, whereas the densely packed dislocations along subgrain boundaries cannot be reliably measured. In contrast, GND densities determined from orientation data include dislocations in subgrain boundaries due to their influence on lattice curvature. Moreover, GND measurements can reveal dislocations that do not thread to sample surfaces during decoration (Wallis et al., 2016).

(2) GND maps have a noise background. Previous studies suggest GND density measured from undeformed silicon and olivine single crystals using HR-ESBD technique is on the order of 10^{12}–10^{13} m^{-2} at step sizes of 0.1–1 μm as used in this study (Jiang et al., 2013b; Ruggles et al., 2016; Wallis et al., 2019; Wallis et al., 2016). Dislocations within subgrain interiors can sometimes be resolved by HR-EBSD but they are often below the noise level. We suggest the apparent GND density below 10^{13} m^{-2} (corresponding to the blue colour in Figs. 6b–10b) results from noise. Areas with GND densities above $10^{13}m^{-2}$ (corresponding to the brown to red colour in Figs. 6b–10b) are robust measurements above the noise level.

The spatial distributions of GND density and stress heterogeneity observed from olivine grains within the Finero peridotite are similar to those obtained from naturally and experimentally deformed samples reported in previous studies (Wallis et al., 2017, 2021, 2022; Wiesman et al., 2024). Residual stress is heterogeneous in deformed domains, varying in magnitude by hundreds of megapascals over distances of a few micrometres (Figs. 7c–10c; Sect. 4.2.2). Moreover, areas of localised, elevated stresses are generally spatially correlated to structures with elevated GND densities (Figs. 7–10). Together, these observations suggest that dislocations are the main source of intragranular stress heterogeneity (Britton et al., 2013; Britton & Wilkinson, 2012b; Hansen et al., 2021; Wallis et al., 2020, 2021) and we explore this interpretation in more detail below.

5.3 Origins of stress heterogeneity

We apply statistical analysis to infer the origin of stress heterogeneity observed in Finero peridotite (Fig. 11; Sect. 4.3). The probability distribution of normalised shear stress, $\hat{\sigma}_{12}$, is broader for olivine within protomylonite, mylonite, and ultramylonite compared to that within the host rock (Fig. 11a; Sect. 4.3). This observation is similar to previous experimental studies, where deformed olivine aggregates have greater stress heterogeneity compared with undeformed samples that underwent the same decompression and cooling (Wallis et al., 2020, 2021). The shape of the normal probability plot (Fig. 11b) can test how close the distribution of stress (Fig. 11a) is to a normal distribution (Sect. 3.3.1). Whilst the central portions of the stress distributions fall on a straight line indicating that they are normally distributed, all microstructural domains exhibit tails that deviate from a straight line (i.e., depart from a normal distribution) and extend to greater stress magnitudes. This effect is widely observed in minerals and metals containing dislocations (e.g., Jiang et al., 2013a; Kalácska et al., 2017; Wallis et al., 2021; Wilkinson et al., 2014). Analysis of the restricted second moment of a stress distribution (Fig. 11c) further assesses the source of intragranular stress by focusing on the form of the tails at high stress magnitudes (Sect. 3.3.1). On the plot of restricted second moment as a function of the natural logarithm of $|\hat{\sigma}_{12}|$, $\ln(|\hat{\sigma}_{12}|)$, the stress distributions fall on straight lines at stress magnitudes greater than ~200 MPa (Fig. 11c; Sect. 4.3). This observation indicates that the high-stress portions of the probability distributions, $P(\sigma)$, decay with $|\sigma|^{-3}$; this form is expected of stress fields of a population of dislocations (Eq. (1); Sect. 3.3.1; Kalácska et al., 2017; Wilkinson et al., 2014). The straight-line proportions for olivine within

protomylonite, mylonite, and ultramylonite are 4–6 times steeper than that of the host rock (Fig. 11c; Sect. 4.3). The slope is proportional to the total dislocation density (Kalácska et al., 2017; Wilkinson et al., 2014). Therefore, this difference in slope is consistent with the factor of six difference in the density of decorated dislocations between the host rock and protomylonite (Sect. 4.4). The curve for recrystallized grains in the protomylonite departs from a straight line above ~1.2 GPa. This phenomenon is commonly observed and has been inferred to result from the averaging of stresses with the highest magnitudes close to the cores of dislocations over the finite interaction volume illuminated by the electron beam in the SEM (Kalácska et al., 2017; Wallis et al., 2021, 2022). Lastly, correlation of the spatial distributions of GND density and intragranular stress heterogeneity also indicates that dislocations are a key source of stress heterogeneity (Sect. 5.2). As the typical length scale of stress heterogeneity in the mylonitic domains is on the order of a few micrometres, whilst the average dislocation spacing is less than a micrometre, the stress heterogeneity constitutes long-range internal stress, by which the dislocations undergo long-range elastic interactions.

5.4 Implications for transient creep during post-seismic deformation

Matysiak & Trepmann (2015) inferred that many of the microstructural elements recorded in the mylonitic rocks of the Finero peridotite formed as a result of sudden increases in differential stress and subsequent relaxation related to seismic cycles during exhumation. Our new data, which focus on characterising the intragranular deformation of olivine, reveal that the dislocations generated during this deformation imparted long-range internal stresses that cause kinematic hardening due to backstress that manifests from long-range elastic interactions (Hansen et al., 2019, 2021; Wallis et al., 2020, 2021). This finding allows us to use a recent model of transient creep (Breithaupt et al., 2023) based on the evolution of backstress generated by dislocations to explore the mechanical behaviour of continental lithospheric mantle during transient creep following sudden increases of stress imposed by earthquakes. The analysis that follows utilises observations from the Finero peridotite as a guide to parameter values but is intended to provide a simple exposition of the basic characteristics of transient creep in such contexts more generally. We note that other processes, such as diffusive or elastically accommodated grain-boundary sliding (Faul & Jackson, 2015; Raj & Ashby, 1971), may also contribute to transients but we focus here on the contribution from dislocation processes to understand this component in isolation. This analysis builds on that of Wallis et al. (2022), who investigated only the instantaneous change in viscosity following a step-change in stress, by exploring the subsequent evolution of mechanical behaviour with strain and time.

5.4.1 Brief introduction of the microphysical model for transient creep

The viscosities, and underlying microphysics, of olivine between the beginning of transient creep and steady state at the end of transient creep are fundamentally different (Hansen et al., 2019, 2021). Consequently, flow laws originally developed to describe steady state are insufficient to assess the rheological evolution of olivine during the transient creep. We apply the microphysical model proposed by Breithaupt et al. (2023), with parameter values summarised in Table 1, to estimate the viscosity change of olivine during the earthquake cycle by considering the impact of long-range interactions due to evolving dislocation density. This model describes the behaviours formerly associated with the distinct deformation mechanisms of low-temperature plasticity (e.g., Hansen et al., 2019), dislocation creep (e.g., Keefner et al., 2011), and dislocation-accommodated grain-boundary sliding (e.g., Hansen et al., 2011), using a single set of equations based on the underlying shared microphysics of dislocation generation, motion, and recovery.

The first key element of this microphysical model is a transient-creep flow law based on the Orowan equation (Orowan, 1934). The Orowan equation (Eq. (3)) describes the strain rate produced by dislocations, $\dot{\varepsilon}_{\text{disl}}$, as a function of ρ, $|b|$, and the glide dislocation velocity, v which is proportional to the $\sinh(\cdot)$ of the effective stress, σ_{eff} (Hansen et al., 2019, 2021).

$$\dot{\varepsilon}_{\text{disl}} = \rho\, b\, v \tag{3}$$

Dislocation motion is sensitive to σ_{eff}, which is the difference between applied stress, σ, the Taylor stress, σ_ρ, and the threshold stress, σ_d, i.e., $\sigma_{\text{eff}} = \sigma - \sigma_\rho - \sigma_d$.

σ_ρ describes the cumulative effects of stress fields generated by dislocations (Taylor, 1934). In other words, σ_ρ acts as a long-range internal backstress arising from dislocation interactions that oppose further dislocation motion (Hansen et al., 2021; Wallis et al., 2020). The magnitude of this backstress is given by:

$$\sigma_\rho = \alpha\, \mu\, b\, \sqrt{\rho}. \tag{4}$$

where α is a constant, μ is the elastic shear modulus.

The threshold stress, σ_d, describes the minimum applied stress required for a dislocation loop to expand within a grain (Gribb & Cooper, 1998):

$$\sigma_d = \beta\, \mu\, b\, d^{-1}, \tag{5}$$

where β is a constant, d is grain size.

Combining the Orowan equation (Orowan, 1934) with the equations for estimating the net glide velocity of dislocations (Breithaupt et al., 2023; Hansen et al., 2019, 2021) gives

$$\dot{\varepsilon}_{\text{disl}} = A'(T)\, \sigma_\rho^2\, \sinh\left(\frac{\sigma - \sigma_\rho - \sigma_d}{\sigma_{\text{ref}}(T)}\right). \tag{6}$$

$A'(T)$ is a temperature-dependent rate coefficient:

$$A'(T) = A'^{*} \exp\left(-\frac{Q_{\text{disl}}}{\mathrm{R}\, T}\right), \tag{7}$$

where A'^{*} is a pre-exponential constant, Q_{disl} is the activation energy of dislocation glide in the absence of an effective stress, and R is the gas constant.

$\sigma_{\text{ref}}(T)$ is a temperature dependent reference stress that depends on the lattice resistance to dislocation glide (i.e., Peierls stress), σ_P^*:

$$\sigma_{\text{ref}}(T) = \sigma_P^*\, \frac{\mathrm{R}\, T}{Q_{\text{disl}}}. \tag{8}$$

The second key element of this microphysical model is to describe the evolving effect of dislocation stress fields, conveniently summarised by the rate of change of σ_ρ, $\dot{\sigma}_\rho$. $\dot{\sigma}_\rho$ is expressed as the difference

between the rate of change of bulk stress due to dislocation storage, $\dot{\sigma}_{\mathrm{storage}}$, and that due to recovery of dislocations, $\dot{\sigma}_{\mathrm{recovery}}$:

$$\dot{\sigma}_\rho = \dot{\sigma}_{\mathrm{storage}} - \dot{\sigma}_{\mathrm{recovery}}. \tag{9}$$

Dislocation storage describes the increase in ρ due to the expansion of dislocation loops with increasing plastic strain:

$$\dot{\sigma}_{\mathrm{storage}} = M(\sigma_\rho + \sigma_d)\sigma_\rho^{-1}\dot{\varepsilon}_{\mathrm{disl}}, \tag{10}$$

where M is a modulus associated with the evolution of $\dot{\sigma}_\rho$.

The recovery of dislocations decreases ρ via static recovery, i.e., annihilation of dislocations:

$$\dot{\sigma}_{\mathrm{recovery}} = \dot{\sigma}_{\mathrm{static}} = M\left(R'_{\mathrm{pipe}}(T)\,\sigma_\rho^5 + R'_{\mathrm{gb}}(T)\,\sigma_\rho^3\,\sigma_d\right), \tag{11}$$

where $R'_{\mathrm{pipe}}(T)$ and $R'_{\mathrm{gb}}(T)$ are temperature-dependant rate coefficients for static recovery facilitated by pipe diffusion, i.e., diffusion of vacancies along dislocation cores, and grain-boundary diffusion, i.e., diffusion of vacancies along grain boundaries, respectively:

$$R'_X(T) = R'^*_X \exp\left(-\frac{Q_{\mathrm{disl}}}{\mathrm{R}\,T}\right), \tag{12}$$

where R'^*_X is a pre-exponential constant for each of the recovery mechanisms, i.e., pipe diffusion and grain-boundary diffusion. For simplicity, we follow Breithaupt et al. (2023) and assume the same Q_{disl} for pipe diffusion and grain boundary diffusion since they are empirically similar (Frost & Ashby, 1982; Ohuchi et al., 2011), together with the assumption that dislocation recovery and glide processes have the same activation energy.

Combining Equations (9)–(11) gives:

$$\dot{\sigma}_\rho = M\left(\frac{\sigma_\rho + \sigma_d}{\sigma_\rho}\,\dot{\varepsilon}_{\mathrm{disl}} - R'_{\mathrm{pipe}}(T)\,\sigma_\rho^5 - R'_{\mathrm{gb}}(T)\,\sigma_\rho^3\,\sigma_d\right). \tag{13}$$

Equations (6) and (13) constitute the model for both transient and steady-state dislocation-accommodated deformation detailed by Breithaupt et al. (2023). In the model, the transient viscosity is primarily controlled by the properties of dislocation glide (Equation (6)), in agreement with the experimental findings of Hansen et al. (2021). In contrast, the steady-state viscosity is controlled by the properties of dislocation recovery mechanisms (Equation (13)). If the dominant recovery mechanism is static recovery facilitated by pipe diffusion, then the steady-state deformation corresponds to dislocation creep (Breithaupt et al., 2023). In contrast, if static recovery is instead facilitated by grain-boundary diffusion, then dislocation-mediated deformation is predicted to be grain-size dependent, consistent with observations of grain-size sensitive dislocation creep (Hansen et al., 2011). This deformation regime is usually termed dislocation-accommodated grain boundary sliding (disGBS), but we note that sliding on the grain boundaries makes a minor contribution to the overall strain (Langdon, 2006). Although the grain-size sensitivity of this regime has been historically attributed to stress concentrations at

grain-boundaries (Langdon, 1994), in the microphysical framework proposed by Breithaupt et al. (2023), it instead arises from enhancement of vacancy diffusion at grain boundaries.

Table 1 Model parameters

Parameter	Value	Reference
A'^{*}	$10^{6.94}$ MPa^{-2}s^{-1}	Breithaupt et al., (2023)
A_{dif}	$10^{7.6}$ MPa^{-1}μm^{3}s^{-1}	Hansen et al. (2011)
Q_{disl}	450 kJmol^{-1}	Breithaupt et al., (2023)
Q_{dif}	375 kJmol^{-1}	Hansen et al. (2011)
R	8.314×10^{-3} kJmol^{-1}K^{-1}	Moldover et al. (1988)
σ_{P}^{*}	3.1 GPa	Hansen et al. (2019)
α	2.46	Breithaupt et al., (2023)
β	2	Bai & Kohlstedt (1992)
μ	65 GPa	Bai & Kohlstedt (1992)
b	5×10^{-10} m	Bai & Kohlstedt (1992)
M	135 GPa	Hansen et al. (2019)
R'^{*}_{pipe}	$10^{-0.95}$ MPa^{-5}s^{-1}	Breithaupt et al., (2023)
R'^{*}_{gb}	$10^{3.53}$ MPa^{-5}s^{-1}	Breithaupt et al., (2023)

5.4.2 Deformation-mechanism maps

We use deformation-mechanism maps (De Bresser et al., 2001; Frost & Ashby, 1982) to constrain the relative contributions of dislocation-mediated deformation and diffusion creep to the total strain rate at the beginning of transient creep and at steady state (Figs. 13a, 13b). We choose a temperature, T, of 800ºC, which is representative of that during deformation of the Finero peridotite (Altenberger, 1995; Lu et al., 1997).

On each map, we plot stress–grain size data for ultramylonite (yellow), mylonite (blue), recrystallized grains in protomylonite (pink), remnant grains in protomylonite (purple), and host rock (black) (Figs. 13a, 13b). At the beginning of transient deformation, the applied stress for protomylonite, mylonite, and ultramylonite during the stress pulse is constrained by the value of 105 MPa estimated from dislocation density in the protomylonite (Fig. 13a; Sect. 4.4). This microstructural domain is the least modified during subsequent relaxation insofar as it preserves slip bands and kinks, which are indicative of low-temperature plasticity, in remnant grains that were formed under high stress and not erased during subsequent relaxation by dislocation-mediated deformation (Matysiak & Trepmann, 2015). If dislocation density in remnant grains of the protomylonite was modified by static annealing then the value of 105 MPa represents a lower bound. At the steady state, we assume that host rock, remnant grains in protomylonite, mylonite, and ultramylonite are subject to the same stress as the recrystallized grains in protomylonite (Fig. 13b). This is because for mylonite and ultramylonite, the mixing of olivine with other phases (Figs. 5a, 5f; Sect. 4.1.3) has potential to pin grain boundaries and maintain a grain size that is less than the piezometric value (Herwegh et al., 2011). The occurrence of this effect is supported by the

difference between the 67 μm median size of recrystallized olivine in the protomylonite, which has mostly monophase grain boundaries and the median grain sizes of 31 μm and 16 μm of olivine in the mylonite and ultramylonite, which has abundant interphase boundaries (Sect. 4.1). Consequently, the grain-size piezometer developed for pure olivine (Qi et al., 2021) should overestimate the stress in mylonite and ultramylonite. We suggest that the pinning effect is less significant in protomylonite as most of the recrystallized olivine grains are in contact with olivine (Fig. 4f; Sect. 4.1.2). Thus, we suggest that the mylonite, ultramylonite, and protomylonite, which are within a distance of a few millimetres (Fig. 3c), were subject to similar stress. We interpret that the value of the background stress should be close to the 28 MPa estimated from dislocation density in the host rock, which was unaffected by stress pulses and the 20 MPa estimated from the grain size of recrystallized olivine within the protomylonite, which represents the value that stress relaxed back to after the stress pulse. The consistency of these two values suggests that ~20–30 MPa was the background stress both before and after the stress pulse.

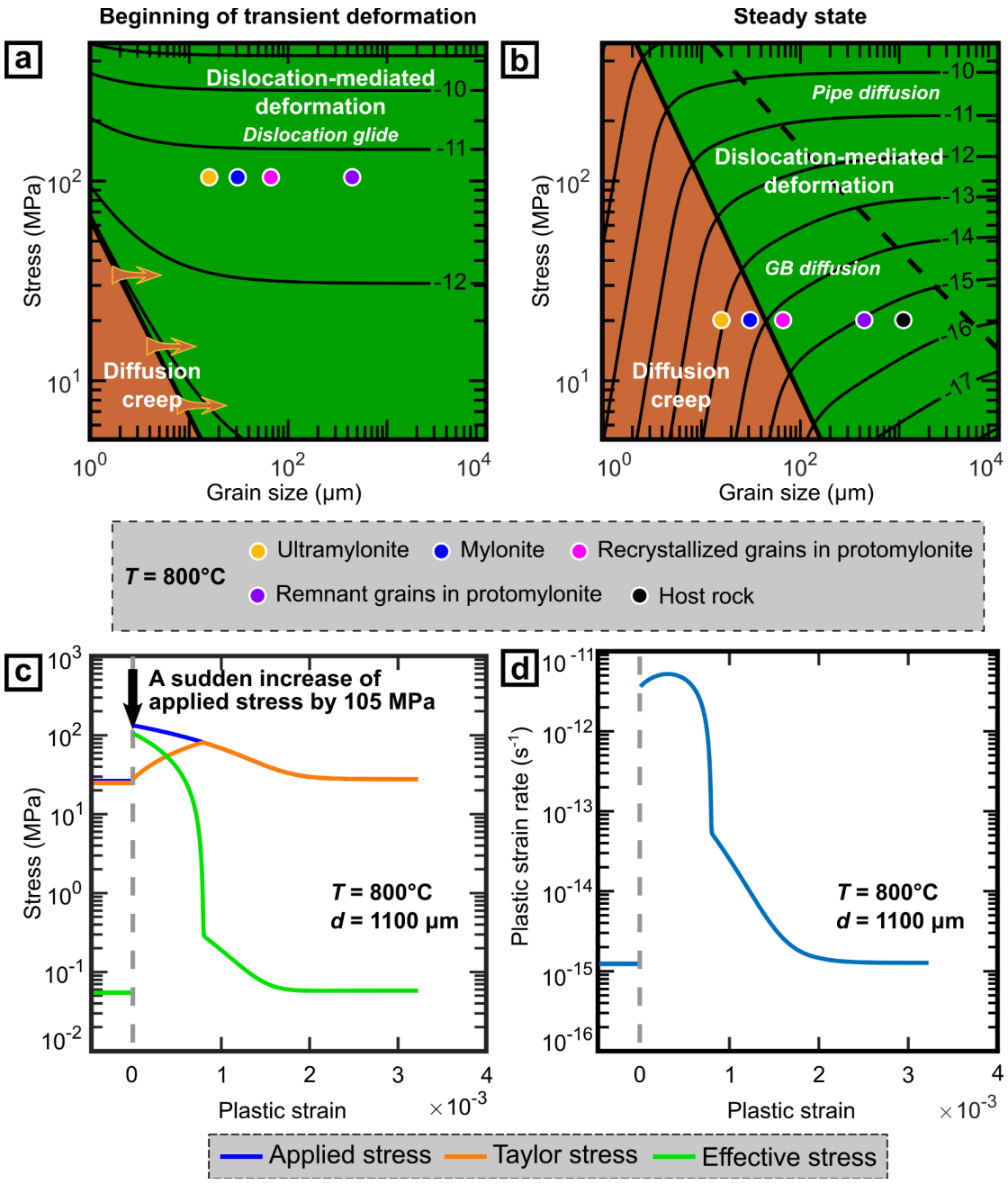

Figure 13. Modelling results using a new microphysical model (Breithaupt et al., 2023) for the transient creep of olivine. **(a)** Deformation-mechanism map at the beginning of transient creep. **(b)** Deformation-mechanism map at steady state. The thick solid black line represents the deformation-mechanism boundary, at where the strain rate of dislocation-mediated deformation equals the strain rate of diffusion creep. The thick dashed black line represents the dislocation recovery-mechanism boundary, where recovery by pipe diffusion balances that facilitated by grain-boundary diffusion. Points represent stress and grain size for ultramylonite, mylonite, recrystallized grains in protomylonite, remnant grains in protomylonite, and host rock. **(c)** The transient evolution of applied stress, Taylor stress, and effective stress as a function of plastic strain. **(d)** The transient evolution of plastic strain rate as a function of plastic strain.

5.4.3 Deformation mechanisms at the beginning of transient creep

Figure 13a presents the deformation-mechanism map for the beginning of transient creep. For each pair of σ and d, we use the dislocation glide flow law (Equation 6) to estimate the dislocation-mediated strain rate. We assume a ρ of 1.7×10^{11} m^{-2}, adopted from the average density of dislocations in the host rock, at the beginning of transient creep.

A flow law that describes transient diffusion creep of olivine in the time domain has not yet been experimentally established. Therefore, we applied a diffusion-creep flow law constrained by steady-state data from dry olivine (Hirth & Kohlstedt, 2003) to estimate the minimum strain rate of diffusion creep, $\dot{\varepsilon}_{\mathrm{dif}}$:

$$\dot{\varepsilon}_{\mathrm{dif}} = A_{\mathrm{dif}}\,\sigma\,d^{-3}\exp\left(-\frac{Q_{\mathrm{dif}}}{\mathrm{R}\,T}\right), \tag{14}$$

where A_{dif} is a pre-exponential constant for diffusion creep and Q_{dif} is the activation energy for diffusion creep (Table 1). This flow law may underestimate the contribution of diffusion creep to the total strain rate at the beginning of transient creep (as indicated by the horizontal brown arrows in Fig. 13a). At the beginning of transient creep, the stress–grain size data of olivine grains in different microstructural domains lie at the right side of the deformation-mechanism boundary (Fig. 13a), indicating a significant contribution of dislocation-mediated deformation.

5.4.4 Deformation mechanisms at steady state

Figure 13b shows the deformation-mechanism map at steady state. We combine Equations (6) and (13) to estimate the strain rate for dislocation-mediated deformation. At steady state, $\dot{\sigma}_{\rho}$ is zero. Therefore, Equations (6) and (13) contain four unknown parameters, including $\dot{\varepsilon}_{\mathrm{disl}}$, σ, σ_{ρ}, which is a function of ρ (Eq. (4)), and σ_d, which is a function of d (Eq. (5)). For each pair of given σ and d, we can then solve for the steady-state values of $\dot{\varepsilon}_{\mathrm{disl}}$ and σ_{ρ}. We applied the same approach described in Sect. 5.4.3 to estimate the strain rate of diffusion creep at steady state.

At steady state, the stress–grain size data of host rock (black dot) and remnant olivine grains in protomylonite (purple dot) lie at the right side of the deformation-mechanism boundary, indicating a significant contribution of dislocation-mediated deformation. The stress–grain size data of olivine grains in ultramylonite (yellow dot) lie at the left side of the deformation-mechanism boundary, indicating a significant contribution of diffusion creep. The stress–grain size data for mylonite (blue dot) and recrystallized olivine grains in protomylonite (pink dot) lie close to the deformation-mechanism boundary, with the former slightly within the diffusion-creep regime and the latter slightly within the dislocation-mediated deformation regime. This observation suggests diffusion creep and dislocation-mediated deformation both had non-negligible contributions to the deformation of protomylonite and mylonite at steady state, but the contribution from diffusion creep is relatively more significant in domains with smaller grain sizes. In all cases, the dominant recovery mechanism for dislocation-mediated deformation is static recovery facilitated by grain-boundary diffusion.

Observations from deformation-mechanism maps indicate a non-negligible contribution of dislocation-mediated deformation at the beginning of transient creep (Figs. 13a; Sect. 5.4.3). At steady state, dislocation-mediated deformation remains an important contributor to deformation; however, its relative contribution decreases with decreasing grain size, consistent with the microstructural evidence

(Fig. 13b; Sect. 5.1.3 and the first paragraph in Sect. 5.4.4). This interpretation is further supported by (1) the observations of dislocations and dislocation substructures (i.e., subgrain boundaries and structures with elevated GND densities) (Figs. 4h, 5c, 5h, 7b–10b, 12; Sects. 5.1.2, 5.2), and (2) the interpretation from the statistics of stress heterogeneity that dislocations are a key source of intragranular stress heterogeneity in all microstructural domains (Sect. 5.3).

5.4.5 The evolution of viscosity during transient creep

We use the coarse grain size of the host rock and remnant grains of the protomylonite as an example to demonstrate the predicted viscosity evolution during the first instance of transient creep following a nearby seismic event, i.e., a sudden increase of applied stress. We choose T of 800ºC (Sect. 5.4.2). We assume that the grain size of the host rock (d = 1100 μm) does not change during a single transient-creep event due to the small strains involved.

We assume that, before a seismic event, the system has reached steady state, manifested as a dynamic balance between the change rate of applied stress, $\dot{\sigma}$, and the change rate of back stress, conveniently $\dot{\sigma}_\rho$. Based on Hooke's law, $\dot{\sigma}$ is a function of elastic strain rate, $\dot{\varepsilon}_e$:

$$\dot{\sigma} = \mu \dot{\varepsilon}_e. \tag{15}$$

The sum of $\dot{\varepsilon}_e$ and plastic strain rate, $\dot{\varepsilon}_p$, is the total strain rate and is referred to as a background strain rate, $\dot{\varepsilon}_{bg}$,

$$\dot{\varepsilon}_{\mathrm{bg}} = \dot{\varepsilon}_e + \dot{\varepsilon}_p. \tag{16}$$

We hold the background strain rate constant throughout the transient at a value of $10^{-14.9}$ s^{-1}, corresponding to σ of ~28 MPa estimated from the dislocation density of host rock (Sect. 4.4). $\dot{\varepsilon}_p$, comprises strain rates contributed by dislocation-mediated deformation and diffusion creep:

$$\dot{\varepsilon}_p = \dot{\varepsilon}_{\mathrm{disl}} + \dot{\varepsilon}_{\mathrm{dif}}, \tag{17}$$

where $\dot{\varepsilon}_{\mathrm{disl}}$ and $\dot{\varepsilon}_{\mathrm{dif}}$ can be calculated by Equation (6) and Equation (14), respectively. Combining Equations (15)–(17) gives:

$$\dot{\sigma} = \mu(\dot{\varepsilon}_{\mathrm{bg}} - \dot{\varepsilon}_p)\,. \tag{18}$$

We solve Equations (13) and (18) simultaneously in MATLAB using the built-in ordinary differential equation solver *ode15s* to calculate the evolution of two interdependent variables, which are σ and σ_ρ. σ at steady state before a seismic event, i.e., $\sigma^{\varepsilon_p<0}$, is ~28 MPa (Fig. 13c). σ_{eff} is on the order of 10^{-2} MPa (Fig. 13c).

We imposed an additional applied stress, $\Delta\sigma$, of 105 MPa, as estimated from the dislocation density in protomylonite (Sect. 4.4), to simulate a sudden stress increase following a seismic event (indicated by a black arrow at ε_p of 0, Fig. 13c):

$$\sigma^{\varepsilon_p=0} = \sigma^{\varepsilon_p<0} + \Delta\sigma. \tag{19}$$

At a given $\varepsilon_p > 0$, we solve Equations (13) and (18) simultaneously using numerical integration to calculate σ and σ_ρ.

Figure 13c presents the model predictions. Following its initial imposed increase, σ decreases with increasing strain and reaches a steady state over a plastic strain interval of ~2×10^{-3}. Meanwhile, σ_ρ increases following the seismic event, due to increasing dislocation density, until it is similar in value to the applied stress, before decreasing with further plastic strain and eventually reaching a steady-state value similar to σ. The evolution of σ_{eff} reflects differences between the evolution of σ and σ_ρ. σ_{eff} steps up three orders of magnitude immediately following the seismic event, before decreasing with plastic strain and eventually reaching steady state. These observations suggest that seismic events will introduce a significant increase in effective stress by temporarily breaking the balance between the applied stress, which induces plastic deformation, and the Taylor stress, which resists the applied stress and plastic deformation.

$\dot{\varepsilon_p}$ is dependent on σ_{eff} (Equations. (6), (17)). Figure 13d reveals that, following the seismic event, $\dot{\varepsilon_p}$ increases instantly by ~3 orders of magnitude to ~3×10^{-12} s^{-1} due to the increase in σ_{eff}, before continuing to increase over the initial 4×10^{-4} plastic strain to 5×10^{-12} s^{-1} as the number of dislocations available to generate strain increases. With subsequent plastic strain, $\dot{\varepsilon_p}$ decreases rapidly as σ_ρ increases, the applied stress relaxes, and hence the effective stress decreases rapidly (Figure 13c). This phase is followed by a more gradual decrease in $\dot{\varepsilon_p}$ as the σ_ρ and applied stress relax in tandem, eventually reaching steady state after a plastic strain of ~2×10^{-3}. These behaviours mirror those in load-relaxation experiments on olivine, which exhibit either both phases of relaxation or only the last phase depending on the crystal orientation(s) and deformation conditions (Cooper et al., 2016; Hansen et al., 2021; Hein et al., 2025; Ohuchi et al., 2024).

Together, model predictions (Sect. 5.4) and microstructural analyses (Sects. 5.1–5.3) suggest that the lithospheric mantle, which is usually at a steady state, is characterised by low effective stress and therefore is sensitive to a sudden change of stress introduced by seismic events. The lithospheric mantle exhibits a transient reduction in viscosity of 2–3 orders of magnitude during post-seismic deformation and the subsequent evolution is controlled, at least in part, by long-range elastic interactions among dislocations. The strains over which postseismic relaxation occurs are on the order of 10^{-3}, which is small relative to the strains required for the grain-size reduction and phase mixing (Tasaka et al., 2017; Wiesman et al., 2023) evident in the shear zones of the Finero peridotite. This difference suggests that additional processes, such as steady-state creep and or local frictional sliding may also have contributed to the finite strains recorded in the Finero shear zones.

6. Conclusions

1. In the protomylonitic peridotite (coarser-grained domains), olivine grains exhibit subgrains and a strong CPO. These features demonstrate that deformation was largely accommodated by dislocation-mediated deformation. In the mylonitic to ultramylonitic peridotite, the CPO of olivine is weak to absent, consistent with significant contribution of diffusion creep. However, HR-EBSD reveals GNDs and stress fields of dislocations, implying a contribution of dislocation-mediated deformation.
2. HR-EBSD maps of olivine reveal that pronounced intragranular stress heterogeneity is spatially correlated with regions of elevated GND density and the form of the probability distributions of the stress heterogeneity is consistent with that expected of a population of dislocations. The typical length scale of stress heterogeneity is a few micrometres, which is greater than the average

dislocation spacing and therefore constitutes long-range internal stress. These observations provide direct evidence that long-range elastic interactions among dislocations occurred in olivine deformed in the continental lithospheric mantle. The similarity of these characteristics to those observed in laboratory experiments (Hansen et al., 2021; Wallis et al., 2017, 2020, 2021; Wiesman et al., 2024) confirms that dislocation backstress and associated kinematic hardening are relevant in the continental lithospheric mantle.

3. Deformation-mechanism maps indicate a shift in the dominant deformation mechanism from the beginning to the end of the transient creep. At the beginning, the grain size-stress data for ultramylonite, mylonite, and recrystallized grains in protomylonite plot within the dislocation-mediated deformation field, indicating that dislocation-mediated deformation is the dominant immediately after a stress increase. At steady state, the host rock and remnant grains in the protomylonite lie within the dislocation-mediated deformation regime, the recrystallised grains in the protomylonite plot just inside the dislocation-mediated deformation field, the mylonite plots slightly within the diffusion-creep regime, and the ultramylonite lies well inside the diffusion-creep regime. This distribution indicates that although dislocation-mediated deformation continues to contribute to deformation across all domains, its relative significance decreases with decreasing grain size. In all cases, the dominant dislocation recovery mechanism is predicted to be static recovery facilitated by grain-boundary diffusion.
4. Applying a dislocation-based microphysical model to the Finero peridotite data predicts a significant evolution in mantle viscosity following a stress increase. Our results demonstrate that the strength of the lithospheric mantle after major earthquakes is highly transient and sensitive to stress changes. Immediately after a sudden stress increase, the effective viscosity of the olivine-rich mantle drops, reflecting a transient weakening. As plastic strain accumulates, dislocation density rises and internal backstress builds up, gradually reducing the effective stress and causing the mantle to re-strengthen towards a new steady state. Consequently, conventional steady-state flow laws alone are insufficient to describe the behaviour. Instead, incorporating transient-creep mechanisms and dislocation backstress is essential for accurately modelling postseismic mantle flow and viscosity evolution.

Data Availability Statement

All data used in this study are openly available from Figshare (Fan et al., 2026).

Acknowledgements

This work was supported by a fellowship from the Royal Commission for the Exhibition of 1851 (T.B.), a UK Research and Innovation Future Leaders Fellowship (MR/V021788/1; D.W.), and the Netherlands Organisation for Scientific Research, User Support Programme Space Research (ENW.GO.001.005; D.W. and T.B.). Microscopy was carried out at the Wolfson Electron Microscopy Suite at the University of Cambridge, which receives funding from the Cambridge Royce facilities Grant EP/P024947/1 and Sir Henry Royce Institute recurrent Grant EP/R00661X/1.

Declaration of competing interest

The authors declare no competing interests.

References

Abramson, E. H., Brown, J. M., Slutsky, L. J., & Zaug, J. (1997). The elastic constants of San Carlos olivine to 17 GPa. *Journal of Geophysical Research: Solid Earth*, *102*(6), 12253–12263. https://doi.org/10.1029/97jb00682

Altenberger, U. (1995). Long-term deformation and fluid-enhanced mass transport in a Variscan peridotite shear zone in the Ivrea Zone, northern Italy: a microtextural, petrological and geochemical study of a reactivated shear zone. *Geologische Rundschau*, *84*(3), 591–606. https://doi.org/10.1007/BF00284523

Andrade, E. N. D. C. (1910). On the viscous flow in metals, and allied phenomena. *Proceedings of the Royal Society of London. Series A, Containing Papers of a Mathematical and Physical Character*, *84*(567), 1–12. https://doi.org/10.1098/rspa.1910.0050

Ashby, M. F., & Verrall, R. A. (1973). Diffusion-accommodated flow and superplasticity. *Acta Metallurgica*, *21*(2), 149–163. https://doi.org/10.1016/0001-6160(73)90057-6

Avouac, J. P. (2015). From geodetic imaging of seismic and aseismic fault slip to dynamic modeling of the seismic cycle. *Annual Review of Earth and Planetary Sciences*, *43*, 233–271. https://doi.org/10.1146/annurev-earth-060614-105302

Bachmann, F., Hielscher, R., & Schaeben, H. (2010). Texture Analysis with MTEX – Free and Open Source Software Toolbox. *Solid State Phenomena*, *160*, 63–68. https://doi.org/10.4028/www.scientific.net/SSP.160.63

Bachmann, Florian, Hielscher, R., & Schaeben, H. (2011). Grain detection from 2d and 3d EBSD data—Specification of the MTEX algorithm. *Ultramicroscopy*, *111*(12), 1720–1733. https://doi.org/10.1016/j.ultramic.2011.08.002

Bai, Q., & Kohlstedt, D. L. (1992). High-temperature creep of olivine single crystals, 2. dislocation structures. *Tectonophysics*, *206*(1–2), 1–29. https://doi.org/10.1016/0040-1951(92)90365-D

Bestmann, M., & Prior, D. J. (2003). Intragranular dynamic recrystallization in naturally deformed calcite marble: Diffusion accommodated grain boundary sliding as a result of subgrain rotation

recrystallization. *Journal of Structural Geology*, *25*(10), 1597–1613. https://doi.org/10.1016/S0191-8141(03)00006-3

Biedermann, A. R., Kunze, K., & Zappone, A. S. (2020). Crystallographic preferred orientation, magnetic and seismic anisotropy in rocks from the Finero peridotite, Ivrea-Verbano Zone, Northern Italy – Interplay of anisotropy contributions from different minerals. *Tectonophysics*, *782–783*(April), 228424. https://doi.org/10.1016/j.tecto.2020.228424

Boriani, A. (1995). *Carta geologica della Valle Cannobina: Geological map of Valle Cannobina, scale 1:25000*.

Boullier, A. M., & Gueguen, Y. (1975). SP-Mylonites: Origin of some mylonites by superplastic flow. *Contributions to Mineralogy and Petrology*, *50*(2), 93–104. https://doi.org/10.1007/BF00373329

Breithaupt, T., Katz, R. F., Hansen, L. N., & Kumamoto, K. M. (2023). Dislocation theory of steady and transient creep of crystalline solids: Predictions for olivine. *Proceedings of the National Academy of Sciences*, *120*(8). https://doi.org/10.1073/pnas.2203448120

Britton, B., Holton, I., Meaden, G., & Dingley, D. (2013). High angular resolution electron backscatter diffraction: measurement of strain in functional and structural materials. *Microscopy and Analysis*, *27*(4), 8.

Britton, T. B., & Wilkinson, A. J. (2011). Measurement of residual elastic strain and lattice rotations with high resolution electron backscatter diffraction. *Ultramicroscopy*, *111*(8), 1395–1404. https://doi.org/10.1016/j.ultramic.2011.05.007

Britton, T. Ben, Goran, D., & Tong, V. S. (2018). Space rocks and optimising scanning electron channelling contrast. *Materials Characterization*, *142*, 422–431. https://doi.org/10.1016/j.matchar.2018.06.001

Britton, T.B., & Wilkinson, A. J. (2012a). High resolution electron backscatter diffraction measurements of elastic strain variations in the presence of larger lattice rotations. *Ultramicroscopy*, *114*, 82–95. https://doi.org/10.1016/j.ultramic.2012.01.004

Britton, T.B., & Wilkinson, A. J. (2012b). Stress fields and geometrically necessary dislocation density

distributions near the head of a blocked slip band. *Acta Materialia*, *60*(16), 5773–5782. https://doi.org/10.1016/j.actamat.2012.07.004

Britton, T.B., Jiang, J., Guo, Y., Vilalta-Clemente, A., Wallis, D., Hansen, L. N., et al. (2016). Tutorial: Crystal orientations and EBSD — Or which way is up? *Materials Characterization*, *117*, 113–126. https://doi.org/10.1016/j.matchar.2016.04.008

Brodie, K. H., & Rutter, E. H. (1987). Deep crustal extensional faulting in the Ivrea Zone of Northern Italy. *Tectonophysics*, *140*(2–4), 193–212. https://doi.org/10.1016/0040-1951(87)90229-0

Campbell, L. R., & Menegon, L. (2019). Transient High Strain Rate During Localized Viscous Creep in the Dry Lower Continental Crust (Lofoten, Norway). *Journal of Geophysical Research: Solid Earth*, *124*(10), 10240–10260. https://doi.org/10.1029/2019JB018052

Cawthorn, R. G. (1975). The Amphibole Peridotite-Metagabbro Complex, Finero, Northern Italy. *The Journal of Geology*, *83*(4), 437–454. https://doi.org/10.1086/628121

Chopra, P. N. (1997). High-temperature transient creep in olivine rocks. *Tectonophysics*, *279*(1–4), 93–111. https://doi.org/10.1016/S0040-1951(97)00134-0

Cooper, R. F., Stone, D. S., & Plookphol, T. (2016). Load relaxation of olivine single crystals. *Journal of Geophysical Research: Solid Earth*, *121*(10), 7193–7210. https://doi.org/10.1002/2016JB013425

Corvò, S., Langone, A., Padrón-Navarta, J. A., Tommasi, A., & Zanetti, A. (2020). Porphyroclasts: Source and sink of major and trace elements during deformation-induced metasomatism (finero, ivrea-verbano zone, Italy). *Geosciences (Switzerland)*, *10*(5). https://doi.org/10.3390/geosciences10050196

Cross, A. J., Prior, D. J., Stipp, M., & Kidder, S. (2017). The recrystallized grain size piezometer for quartz: An EBSD-based calibration. *Geophysical Research Letters*, *44*(13), 6667–6674. https://doi.org/10.1002/2017GL073836

Danielson, J. J., & Gesch, D. B. (2011). *Global multi-resolution terrain elevation data 2010 (GMTED2010): U.S. Geological Survey Open-File Report 2011–1073* (pp. 1–26).

Davidson, P. M., & Lindsley, D. H. (1985). Thermodynamic analysis of quadrilateral pyroxenes.

Contributions to Mineralogy and Petrology, *91*(4), 390–404. https://doi.org/10.1007/BF00374695

De Bresser, J. H. P., Ter Heege, J. H., & Spiers, C. J. (2001). Grain size reduction by dynamic recrystallization: Can it result in major rheological weakening? *International Journal of Earth Sciences*, *90*(1), 28–45. https://doi.org/10.1007/s005310000149

Duval, P., Ashby, M. F., & Anderman, I. (1983). Rate-controlling processes in the creep of polycrystalline ice. *Journal of Physical Chemistry*, *87*(21), 4066–4074. https://doi.org/10.1021/j100244a014

Ellis, S., & Stöckhert, B. (2004). Elevated stresses and creep rates beneath the brittle-ductile transition caused by seismic faulting in the upper crust. *Journal of Geophysical Research: Solid Earth*, *109*(5). https://doi.org/10.1029/2003JB002744

Evans, B. W., & Trommsdorff, V. (1970). Regional metamorphism of ultramafic rocks in the Central Alps : parageneses in the system CaO-MgO-SiO2-H2O. *Schweizerische Mineralogische Und Petrographische Mitteilungen*, *50*, 481–492.

Fan, S., Hager, T. F., Prior, D. J., Cross, A. J., Goldsby, D. L., Qi, C., et al. (2020). Temperature and strain controls on ice deformation mechanisms: insights from the microstructures of samples deformed to progressively higher strains at −10, −20 and −30 °C. *The Cryosphere*, *14*(11), 3875–3905. https://doi.org/10.5194/tc-14-3875-2020

Fan, S., Cross, A. J., Prior, D. J., Goldsby, D. L., Hager, T. F., Negrini, M., & Qi, C. (2021). Crystallographic Preferred Orientation (CPO) Development Governs Strain Weakening in Ice: Insights From High‐Temperature Deformation Experiments. *Journal of Geophysical Research: Solid Earth*, *126*(12). https://doi.org/10.1029/2021JB023173

Fan, S., Prior, D. J., Cross, A. J., Goldsby, D. L., Hager, T. F., Negrini, M., & Qi, C. (2021). Using grain boundary irregularity to quantify dynamic recrystallization in ice. *Acta Materialia*, *209*, 116810. https://doi.org/10.1016/j.actamat.2021.116810

Fan, S., Wheeler, J., Prior, D. J., Negrini, M., Cross, A. J., Hager, T. F., et al. (2022). Using Misorientation and Weighted Burgers Vector Statistics to Understand Intragranular Boundary Development and Grain Boundary Formation at High Temperatures. *Journal of Geophysical Research: Solid Earth*,

127(8). https://doi.org/10.1029/2022JB024497

Fan, S., Breithaupt, T., Trepmann, C. A., & Wallis, D. (2026). Data for "Backstress governs transient postseismic creep in the continental lithospheric mantle" [Data set]. Figshare. https://doi.org/10.6084/m9.figshare.31164136

Faul, U., & Jackson, I. (2015). Transient Creep and Strain Energy Dissipation: An Experimental Perspective. *Annual Review of Earth and Planetary Sciences*, *43*(1), 541–569. https://doi.org/10.1146/annurev-earth-060313-054732

Fliervoet, T. F., White, S. H., & Drury, M. R. (1997). Evidence for dominant grain-boundary sliding deformation in greenschist- and amphibolite-grade polymineralic ultramylonites from the Redbank Deformed Zone, Central Australia. *Journal of Structural Geology*, *19*(12), 1495–1520. https://doi.org/10.1016/S0191-8141(97)00076-X

Freed, A. M., Herring, T., & Bürgmann, R. (2010). Steady-state laboratory flow laws alone fail to explain postseismic observations. *Earth and Planetary Science Letters*, *300*(1–2), 1–10. https://doi.org/10.1016/j.epsl.2010.10.005

Frost, H. J., & Ashby, M. F. (1982). *Deformation mechanism maps: the plasticity and creep of metals and ceramics*. Pergamon Press. Retrieved from https://engineering.dartmouth.edu/defmech/

Gasparik, T. (1984). Two-pyroxene thermobarometry with new experimental data in the system CaO-MgO-Al2O3-SiO2. *Contributions to Mineralogy and Petrology*, *87*(1), 87–97. https://doi.org/10.1007/BF00371405

Giovanardi, T., Mazzucchelli, M., Zanetti, A., Langone, A., Tiepolo, M., & Cipriani, A. (2014). Occurrence of phlogopite in the Finero Mafic layered complex. *Central European Journal of Geosciences*, *6*(4), 588–613. https://doi.org/10.2478/s13533-012-0186-8

Glen, J. W. (1952). Experiments on the Deformation of Ice. *Journal of Glaciology*, *2*(12), 111–114. https://doi.org/10.1017/s0022143000034067

Gribb, T. T., & Cooper, R. F. (1998). Low-frequency shear attenuation in polycrystalline olivine: Grain boundary diffusion and the physical significance of the Andrade model for viscoelastic rheology.

Journal of Geophysical Research: Solid Earth, *103*(B11), 27267–27279. https://doi.org/10.1029/98jb02786

Halfpenny, A., Prior, D. J., & Wheeler, J. (2006). Analysis of dynamic recrystallization and nucleation in a quartzite mylonite. *Tectonophysics*, *427*(1–4), 3–14. https://doi.org/10.1016/j.tecto.2006.05.016

Hansen, L. N., Zimmerman, M. E., & Kohlstedt, D. L. (2011). Grain boundary sliding in San Carlos olivine: Flow law parameters and crystallographic-preferred orientation. *Journal of Geophysical Research: Solid Earth*, *116*(8), 1–16. https://doi.org/10.1029/2011JB008220

Hansen, L N, Zimmerman, M. E., & Kohlstedt, D. L. (2012). The influence of microstructure on deformation of olivine in the grain-boundary sliding regime. *Journal of Geophysical Research*, *117*(B9), 117–149.

Hansen, Lars N., Kumamoto, K. M., Thom, C. A., Wallis, D., Durham, W. B., Goldsby, D. L., et al. (2019). Low-Temperature Plasticity in Olivine: Grain Size, Strain Hardening, and the Strength of the Lithosphere. *Journal of Geophysical Research: Solid Earth*, *124*(6), 5427–5449. https://doi.org/10.1029/2018JB016736

Hansen, Lars N., Wallis, D., Breithaupt, T., Thom, C. A., & Kempton, I. (2021). Dislocation Creep of Olivine: Backstress Evolution Controls Transient Creep at High Temperatures. *Journal of Geophysical Research: Solid Earth*, *126*(5), 1–21. https://doi.org/10.1029/2020JB021325

Hanson, D. R., & Spetzler, H. A. (1994). Transient creep in natural and synthetic, iron-bearing olivine single crystals: Mechanical results and dislocation microstructures. *Tectonophysics*, *235*(4), 293–315. https://doi.org/10.1016/0040-1951(94)90191-0

Hein, D., Hansen, L., & Dillman, A. M. (2025, October 2). Mimicking postseismic creep in the laboratory: testing dislocation-based models for transient creep in the upper mantle. Preprints. https://doi.org/10.22541/essoar.175941674.47414922/v1

Hentschel, F., Janots, E., Magnin, V., Brückner, L. M., & Trepmann, C. A. (2022). Transient deformation and long-term tectonic activity in the Eastern Alps recorded by mylonitic pegmatites. *Journal of Structural Geology*, *155*. https://doi.org/10.1016/j.jsg.2021.104507

Herwegh, M., Linckens, J., Ebert, A., Berger, A., & Brodhag, S. H. (2011). The role of second phases for controlling microstructural evolution in polymineralic rocks: A review. *Journal of Structural Geology*, *33*(12), 1728–1750. https://doi.org/10.1016/j.jsg.2011.08.011

Hetland, E. A., & Simons, M. (2010). Post-seismic and interseismic fault creep II: Transient creep and interseismic stress shadows on megathrusts. *Geophysical Journal International*, *181*(1), 99–112. https://doi.org/10.1111/j.1365-246X.2009.04482.x

Hirth, G., & Kohlstedt, D. (2003). Rheology of the upper mantle and the mantle wedge: A view from the experimentalists. In *Geophysical Monograph Series* (Vol. 138, pp. 83–105). https://doi.org/10.1029/138GM06

Hirth, G., & Tullis, J. (1992). Dislocation creep regimes in quartz aggregates. *Journal of Structural Geology*, *14*(2), 145–159. https://doi.org/10.1016/0191-8141(92)90053-Y

Hodges, K. V., & Fountain, D. M. (1984). Pogallo Line, South Alps, northern Italy: An intermediate crystal level, low-angle normal fault? *Geology*, *12*(3), 151. https://doi.org/10.1130/0091-7613(1984)12%3C151:PLSANI%3E2.0.CO;2

Holzhausen, G. R., & Johnson, A. M. (1979). The concept of residual stress in rock. *Tectonophysics*, *58*(3–4), 237–267. https://doi.org/10.1016/0040-1951(79)90311-1

Jiang, J., Britton, T. B., & Wilkinson, A. J. (2013a). Mapping type III intragranular residual stress distributions in deformed copper polycrystals. *Acta Materialia*, *61*(15), 5895–5904. https://doi.org/10.1016/j.actamat.2013.06.038

Jiang, J., Britton, T. B., & Wilkinson, A. J. (2013b). Measurement of geometrically necessary dislocation density with high resolution electron backscatter diffraction: Effects of detector binning and step size. *Ultramicroscopy*, *125*, 1–9. https://doi.org/10.1016/j.ultramic.2012.11.003

Jiang, Z., Prior, D. J., & Wheeler, J. (2000). Albite crystallographic preferred orientation and grain misorientation distribution in a low-grade mylonite: Implications for granular flow. *Journal of Structural Geology*, *22*(11–12), 1663–1674. https://doi.org/10.1016/S0191-8141(00)00079-1

Kalácska, S., Groma, I., Borbély, A., & Ispánovity, P. D. (2017). Comparison of the dislocation density

obtained by HR-EBSD and X-ray profile analysis. *Applied Physics Letters*, *110*(9). https://doi.org/10.1063/1.4977569

Karato, S. (1988). The role of recrystallization in the preferred orientation of olivine. *Physics of the Earth and Planetary Interiors*, *51*(1–3), 107–122. https://doi.org/10.1016/0031-9201(88)90029-5

Karato, S. (2008). *Deformation of Earth Materials*. Cambridge University Press. https://doi.org/10.1017/CBO9780511804892

Keefner, J. W., Mackwell, S. J., Kohlstedt, D. L., & Heidelbach, F. (2011). Dependence of dislocation creep of dunite on oxygen fugacity: Implications for viscosity variations in Earth's mantle. *Journal of Geophysical Research*, *116*(B5), B05201. https://doi.org/10.1029/2010JB007748

Kenkmann, T. (2000). Processes controlling the shrinkage of porphyroclasts in gabbroic shear zones. *Journal of Structural Geology*, *22*(4), 471–487. https://doi.org/10.1016/S0191-8141(99)00177-7

Kenkmann, T., & Dresen, G. (2002). Dislocation microstructure and phase distribution in a lower crustal shear zone - An example from the Ivrea-Zone, Italy. *International Journal of Earth Sciences*, *91*(3), 445–458. https://doi.org/10.1007/s00531-001-0236-9

Kohlstedt, D. L., Goetze, C., Durham, W. B., & Vander Sande, J. (1976). New technique for decorating dislocations in olivine. *Science*, *191*(4231), 1045–1046. https://doi.org/10.1126/science.191.4231.1045

Kröner, E. (1958). Continuum theory of dislocations and self‐stresses. *Ergebnisse Der Angewandten Mathematik*, *5*, 1327–1347.

Laird, J., & Albee, A. L. (1981). Pressure, temperature, and time indicators in mafic schist; their application to reconstructing the polymetamorphic history of Vermont. *American Journal of Science*, *281*(2), 127–175. https://doi.org/10.2475/ajs.281.2.127

Langdon, T. G. (1994). A unified approach to grain boundary sliding in creep and superplasticity. *Acta Metallurgica Et Materialia*, *42*(7), 2437–2443. https://doi.org/10.1016/0956-7151(94)90322-0

Langdon, Terence G. (2006). Grain boundary sliding revisited: Developments in sliding over four decades. *Journal of Materials Science*, *41*(3), 597–609.

https://doi.org/10.1007/s10853-006-6476-0

Langone, A., Zanetti, A., Daczko, N. R., Piazolo, S., Tiepolo, M., & Mazzucchelli, M. (2018). Zircon U-Pb Dating of a Lower Crustal Shear Zone: A Case Study From the Northern Sector of the Ivrea-Verbano Zone (Val Cannobina, Italy). *Tectonics*, *37*(1), 322–342. https://doi.org/10.1002/2017TC004638

Langone, Antonio, Padrón-Navarta José, A., Ji, W. Q., Zanetti, A., Mazzucchelli, M., Tiepolo, M., et al. (2017). Ductile–brittle deformation effects on crystal-chemistry and U–Pb ages of magmatic and metasomatic zircons from a dyke of the Finero Mafic Complex (Ivrea–Verbano Zone, Italian Alps). *Lithos*, *284–285*, 493–511. https://doi.org/10.1016/j.lithos.2017.04.020

Lindsley, D. H. (1983). Pyroxene thermometry. *American Mineralogist*, *68*, 477–493.

Lu, M., Hofmann, A. W., Mazzucchelli, M., & Rivalenti, G. (1997). *The mafic-ultramafic complex near Finero (Ivrea-Verbano Zone), I. Chemistry of MORB-like magmas*. *Chemical Geology* (Vol. 140, pp. 207–222).

Masuti, S., Barbot, S. D., Karato, S. I., Feng, L., & Banerjee, P. (2016). Upper-mantle water stratification inferred from observations of the 2012 Indian Ocean earthquake. *Nature*, *538*(7625), 371–377. https://doi.org/10.1038/nature19783

Matysiak, A. K., & Trepmann, C. A. (2015). The deformation record of olivine in mylonitic peridotites from the Finero Complex, Ivrea Zone: Separate deformation cycles during exhumation. *Tectonics*, *34*(12), 2514–2533. https://doi.org/10.1002/2015TC003904

Maurice, C., Driver, J. H., & Fortunier, R. (2011). On solving the orientation gradient dependency of high angular resolution EBSD. *Ultramicroscopy*, *113*, 171–181. https://doi.org/10.1016/j.ultramic.2011.10.013

Mikami, Y., Oda, K., Kamaya, M., & Mochizuki, M. (2015). Effect of reference point selection on microscopic stress measurement using EBSD. *Materials Science and Engineering: A*, *647*, 256–264. https://doi.org/10.1016/j.msea.2015.09.004

Misra, A. K., & Murrell, S. A. F. (1965). An Experimental Study of the Effect of Temperature and Stress

on the Creep of Rocks. *Geophysical Journal of the Royal Astronomical Society*, *9*(5), 509–535. https://doi.org/10.1111/j.1365-246X.1965.tb06322.x

Moldover, M. R., Trusler, J. P. M., Edwards, T. J., Mehl, J. B., & Davis, R. S. (1988). Measurement of the Universal Gas Constant R Using a Spherical Acoustic Resonator. *Physical Review Letters*, *60*(4), 249–252. https://doi.org/10.1103/PhysRevLett.60.249

Muto, J., Moore, J. D. P., Barbot, S., Iinuma, T., Ohta, Y., & Iwamori, H. (2019). Coupled afterslip and transient mantle flow after the 2011 Tohoku earthquake. *Science Advances*, *5*(9). https://doi.org/10.1126/sciadv.aaw1164

Neubauer, F. (2014). The structure of the Eastern Alps: from Eduard Suess to present-day knowledge.

Nüchter, J. A., & Ellis, S. (2010). Complex states of stress during the normal faulting seismic cycle: Role of midcrustal postseismic creep. *Journal of Geophysical Research: Solid Earth*, *115*(12). https://doi.org/10.1029/2010JB007557

Nye, J. F. (1953). Some geometrical relations in dislocated crystals. *Acta Metallurgica*, *1*(2), 153–162. https://doi.org/10.1016/0001-6160(53)90054-6

Ohuchi, T., Karato, S. ichiro, & Fujino, K. (2011). Strength of single-crystal orthopyroxene under lithospheric conditions. *Contributions to Mineralogy and Petrology*, *161*(6), 961–975. https://doi.org/10.1007/s00410-010-0574-3

Ohuchi, T., Higo, Y., Tsujino, N., Seto, Y., Kakizawa, S., Tange, Y., et al. (2024). Transient Creep in Olivine at Shallow Mantle Pressures: Implications for Time‐Dependent Rheology in Post‐Seismic Deformation. *Geophysical Research Letters*, *51*(11), e2024GL108356. https://doi.org/10.1029/2024GL108356

Orowan, E. (1934). Zur Kristallplastizität. I - Tieftemperaturplastizität und Beckersche Formel. *Zeitschrift Für Physik*, *89*(9–10), 605–613. https://doi.org/10.1007/BF01341478

Poirier, J. P., & Nicolas, A. (1975). Deformation-Induced Recrystallization Due to Progressive Misorientation of Subgrains, with Special Reference to Mantle Peridotites. *The Journal of Geology*, *83*(6), 707–720. https://doi.org/10.1086/628163

Ponge, D., & Gottstein, G. (1998). Necklace formation during dynamic recrystallization: Mechanisms and impact on flow behavior. *Acta Materialia*, *46*(1), 69–80. https://doi.org/10.1016/S1359-6454(97)00233-4

Post, R. L. (1977). High-temperature creep of Mt. Burnet Dunite. *Tectonophysics*, *42*(2–4), 75–110. https://doi.org/10.1016/0040-1951(77)90162-7

Prior, D. J. (1999). Problems in determining the misorientation axes, for small angular misorientations, using electron backscatter diffraction in the SEM. *Journal of Microscopy*, *195*(3), 217–225. https://doi.org/10.1046/j.1365-2818.1999.00572.x

Qi, C., Zhao, Y. H., Zimmerman, M. E., Kim, D., & Kohlstedt, D. L. (2021). Evolution of Microstructural Properties in Sheared Iron-Rich Olivine. *Journal of Geophysical Research: Solid Earth*, *126*(3). https://doi.org/10.1029/2020JB019629

Quick, J. E., Sinigoi, S., & Mayer, A. (1995). Emplacement of mantle peridotite in the lower continental crust, Ivrea-Verbano zone, northwest Italy. *Geology*, *23*(8), 739. https://doi.org/10.1130/0091-7613(1995)023%3C0739:EOMPIT%3E2.3.CO;2

Raj, R., & Ashby, M. F. (1971). On grain boundary sliding and diffusional creep. *Metallurgical Transactions*, *2*(4), 1113–1127. https://doi.org/10.1007/BF02664244

Ruggles, T. J., Rampton, T. M., Khosravani, A., & Fullwood, D. T. (2016). The effect of length scale on the determination of geometrically necessary dislocations via EBSD continuum dislocation microscopy. *Ultramicroscopy*, *164*, 1–10. https://doi.org/10.1016/j.ultramic.2016.03.003

Rutter, E. H., Brodie, K. H., & Evans, P. J. (1993). Structural geometry, lower crustal magmatic underplating and lithospheric stretching in the Ivrea-Verbano zone, northern Italy. *Journal of Structural Geology*, *15*(3–5), 647–662. https://doi.org/10.1016/0191-8141(93)90153-2

Schmid, S. M., Zingg, A., & Handy, M. (1987). The kinematics of movements along the Insubric Line and the emplacement of the Ivrea Zone. *Tectonophysics*, *135*(1–3), 47–66. https://doi.org/10.1016/0040-1951(87)90151-X

Siena, F., & Coltorti, M. (1989). The Petrogenesis Of A Hydrated Mafic Ultramafic Complex And The

Role Of Amphibole Fractionation At Finero (Italian Western Alps). *Neues Jahrbuch Fur Mineralogie-Monatshefte*, (6), 255–274.

Skemer, P., Katayama, I., Jiang, Z., & Karato, S. I. (2005). The misorientation index: Development of a new method for calculating the strength of lattice-preferred orientation. *Tectonophysics*, *411*(1–4), 157–167. https://doi.org/10.1016/j.tecto.2005.08.023

Smith, B. K., & Carpenter, F. O. (1987). Transient creep in orthosilicates. *Physics of the Earth and Planetary Interiors*, *49*(3–4), 314–324. https://doi.org/10.1016/0031-9201(87)90033-1

Spear, F. S. (1980). NaSi?CaAl exchange equilibrium between plagioclase and amphibole. *Contributions to Mineralogy and Petrology*, *72*(1), 33–41. https://doi.org/10.1007/BF00375566

Stipp, M., Tullis, J., Scherwath, M., & Behrmann, J. H. (2010). A new perspective on paleopiezometry: Dynamically recrystallized grain size distributions indicate mechanism changes. *Geology*, *38*(8), 759–762. https://doi.org/10.1130/G31162.1

Storey, C. D., & Prior, D. J. (2005). Plastic deformation and recrystallization of garnet: A mechanism to facilitate diffusion creep. *Journal of Petrology*, *46*(12), 2593–2613. https://doi.org/10.1093/petrology/egi067

Tasaka, M., Zimmerman, M. E., & Kohlstedt, D. L. (2017). Rheological Weakening of Olivine + Orthopyroxene Aggregates Due to Phase Mixing: 1. Mechanical Behavior. *Journal of Geophysical Research: Solid Earth*, *122*(10), 7584–7596. https://doi.org/10.1002/2017JB014333

Taylor, G. I. (1934). The mechanism of plastic deformation of crystals. Part I.—Theoretical. *Proceedings of the Royal Society of London. Series A, Containing Papers of a Mathematical and Physical Character*, *145*(855), 362–387. https://doi.org/10.1098/rspa.1934.0106

Tommasi, A., Langone, A., Padrón-Navarta, J. A., Zanetti, A., & Vauchez, A. (2017). Hydrous melts weaken the mantle, crystallization of pargasite and phlogopite does not: Insights from a petrostructural study of the Finero peridotites, southern Alps. *Earth and Planetary Science Letters*, *477*, 59–72. https://doi.org/10.1016/j.epsl.2017.08.015

Trepmann, C. A., Renner, J., & Druiventak, A. (2013). Experimental deformation and recrystallization of

olivine-processes and timescales of damage healing during postseismic relaxation at mantle depths. *Solid Earth*, *4*(2), 423–450. https://doi.org/10.5194/se-4-423-2013

Trepmann, Claudia A., & Seybold, L. (2019). Deformation at low and high stress-loading rates. *Geoscience Frontiers*, *10*(1), 43–54. https://doi.org/10.1016/j.gsf.2018.05.002

Trommsdorff, V., & Connolly, J. A. D. (1990). Constraints on phase diagram topology for the system CaO-MgO-SiO2-CO2-H2O. *Contributions to Mineralogy and Petrology*, *104*(1), 1–7. https://doi.org/10.1007/BF00310641

Urai, J. L., Means, W. D., & Lister, G. S. (1986). Dynamic recrystallization of minerals. In *Mineral and Rock Deformation: Laboratory Studies* (Vol. 36, pp. 161–199). https://doi.org/10.1029/GM036p0161

Vogt, P. (1962). Geologisch-petrographische Untersuchungen im Peridotitstock von Finero. *Schweiz. Mineral. Petrogr. Mitt.*, *42*, 59–125.

Wallis, D., Hansen, L. N., Britton, T. B., & Wilkinson, A. J. (2019). High-Angular Resolution Electron Backscatter Diffraction as a New Tool for Mapping Lattice Distortion in Geological Minerals. *Journal of Geophysical Research: Solid Earth*, *124*(7), 6337–6358. https://doi.org/10.1029/2019JB017867

Wallis, David, Hansen, L. N., Ben Britton, T., & Wilkinson, A. J. (2016). Geometrically necessary dislocation densities in olivine obtained using high-angular resolution electron backscatter diffraction. *Ultramicroscopy*, *168*(2016), 34–45. https://doi.org/10.1016/j.ultramic.2016.06.002

Wallis, David, Hansen, L. N., Britton, T. B., & Wilkinson, A. J. (2017). Dislocation Interactions in Olivine Revealed by HR-EBSD. *Journal of Geophysical Research: Solid Earth*, *122*(10), 7659–7678. https://doi.org/10.1002/2017JB014513

Wallis, David, Parsons, A. J., & Hansen, L. N. (2019). Quantifying geometrically necessary dislocations in quartz using HR-EBSD: Application to chessboard subgrain boundaries. *Journal of Structural Geology*, *125*(September 2017), 235–247. https://doi.org/10.1016/j.jsg.2017.12.012

Wallis, David, Hansen, L. N., Kumamoto, K. M., Thom, C. A., Plümper, O., Ohl, M., et al. (2020).

Dislocation interactions during low-temperature plasticity of olivine and their impact on the evolution of lithospheric strength. *Earth and Planetary Science Letters*, *543*(June), 116349. https://doi.org/10.1016/j.epsl.2020.116349

Wallis, David, Hansen, L. N., Wilkinson, A. J., & Lebensohn, R. A. (2021). Dislocation interactions in olivine control postseismic creep of the upper mantle. *Nature Communications*, *12*(1), 1–12. https://doi.org/10.1038/s41467-021-23633-8

Wallis, David, Sep, M., & Hansen, L. N. (2022). Transient Creep in Subduction Zones by Long‐Range Dislocation Interactions in Olivine. *Journal of Geophysical Research: Solid Earth*, *127*(1). https://doi.org/10.1029/2021jb022618

Wang, K., Hu, Y., & He, J. (2012). Deformation cycles of subduction earthquakes in a viscoelastic Earth. *Nature*, *484*(7394), 327–332. https://doi.org/10.1038/nature11032

Warren, J. M., & Hirth, G. (2006). Grain size sensitive deformation mechanisms in naturally deformed peridotites. *Earth and Planetary Science Letters*, *248*(1–2), 438–450. https://doi.org/10.1016/j.epsl.2006.06.006

Weertman, J., & Weertman, J. R. (1975). High Temperature Creep of Rock and Mantle Viscosity. *Annual Review of Earth and Planetary Sciences*, *3*(1), 293–315. https://doi.org/10.1146/annurev.ea.03.050175.001453

Weertman, J. W. (1978). Creep laws for the mantle of the Earth. *Philosophical Transactions of the Royal Society of London. Series A, Mathematical and Physical Sciences*, *288*(1350), 9–26. https://doi.org/10.1098/rsta.1978.0003

Wells, P. R. A. (1977). Pyroxene thermometry in simple and complex systems. *Contributions to Mineralogy and Petrology*, *62*(2), 129–139. https://doi.org/10.1007/BF00372872

Wheeler, J. (2010). Anisotropic rheology during grain boundary diffusion creep and its relation to grain rotation, grain boundary sliding and superplasticity. *Philosophical Magazine*, *90*(21), 2841–2864. https://doi.org/10.1080/14786431003636097

White, S. (1976). The Effects of Strain on the Microstructures, Fabrics, and Deformation Mechanisms in

Quartzites. *Philosophical Transactions of the Royal Society A: Mathematical and Physical Sciences*, *283*(1312), 69–86.

Wiesman, H. S., & Wallis, D. (2026). The effect of pattern quality on measurements of stress heterogeneity and geometrically necessary dislocation density by high-angular resolution electron backscatter diffraction. *Ultramicroscopy*, *282*, 114330. https://doi.org/10.1016/j.ultramic.2026.114330

Wiesman, H. S., Zimmerman, M. E., & Kohlstedt, D. L. (2023). The Effect of Secondary‐Phase Fraction on the Deformation of Olivine + Ferropericlase Aggregates: 2. Mechanical Behavior. *Journal of Geophysical Research: Solid Earth*, *128*(4), e2022JB025724. https://doi.org/10.1029/2022JB025724

Wiesman, H. S., Breithaupt, T., Wallis, D., & Hansen, L. N. (2024). Microstructural and Micromechanical Evolution of Olivine Aggregates During Transient Creep. *Journal of Geophysical Research: Solid Earth*, *129*(12), e2024JB029812. https://doi.org/10.1029/2024JB029812

Wilkinson, A. J., Meaden, G., & Dingley, D. J. (2006). High-resolution elastic strain measurement from electron backscatter diffraction patterns: New levels of sensitivity. *Ultramicroscopy*, *106*(4–5), 307–313. https://doi.org/10.1016/j.ultramic.2005.10.001

Wilkinson, A. J., Tarleton, E., Vilalta-Clemente, A., Jiang, J., Britton, T. B., & Collins, D. M. (2014). Measurement of probability distributions for internal stresses in dislocated crystals. *Applied Physics Letters*, *105*(18). https://doi.org/10.1063/1.4901219

Yabe, K., Sueyoshi, K., & Hiraga, T. (2020). Grain-Boundary Diffusion Creep of Olivine: 1. Experiments at 1 atm. *Journal of Geophysical Research: Solid Earth*, *125*(8). https://doi.org/10.1029/2020JB019415

Appendix A. List of symbols used in this paper, ordered by first appearance

Symbol	Name
Ψ	Grain-boundary sphericity parameter
A	Grain area
P	Grain-boundary Perimeter
σ_{ij}	Residual stress tensor
$\hat{\sigma}_{ij}$	Normalised residual stress tensor
G	Shear modulus
b	Burgers vector
ρ	Dislocation density
C_σ	Shear contrast factor
$\dot{\varepsilon}_{\mathrm{disl}}$	Strain rate of dislocation creep
v	Glide dislocation velocity
σ_{eff}	Effective stress
σ	Applied stress
σ_ρ	Taylor stress
σ_d	Threshold stress
α	Constant for calculating σ_ρ
μ	Elastic shear modulus
β	Constant for calculating σ_d

d	Grain size
$A'(T)$	Temperature-dependent rate coefficient
A'^{*}	Pre-exponential constant for calculating $A'(T)$
Q_{disl}	Activation energy of dislocation creep in the absence of an effective stress
R	Gas constant
$\sigma_{\text{ref}}(T)$	Temperature dependent reference stress
σ_P^*	Peierls stress
$\dot{\sigma}_\rho$	Rate of change of σ_ρ
$\dot{\sigma}_{\text{store}}$	Rate of change of bulk stress due to dislocation storage
$\dot{\sigma}_{\text{recovery}}$	Rate of change of bulk stress due to recovery of dislocations
M	Modulus associated with the evolution of $\dot{\sigma}_\rho$
$R'_{\text{pipe}}(T)$	Temperature-dependant rate coefficients for static recovery facilitated by pipe diffusion
$R'_{\text{gb}}(T)$	Temperature-dependant rate coefficients for static recovery facilitated by boundary diffusion
R'^{*}_X	Pre-exponential constant for pipe diffusion and grain-boundary diffusion
$\dot{\varepsilon}_{\text{dif}}$	Strain rate of diffusion creep
A_{dif}	Pre-exponential constant for diffusion creep
Q_{dif}	Activation energy for diffusion creep

$\dot{\sigma}$	Change rate of σ
$\dot{\varepsilon}_e$	Elastic strain rate
$\dot{\varepsilon}_p$	Plastic strain rate
$\dot{\varepsilon}_{bg}$	Background strain rate
$\Delta\sigma$	Additional applied stress

Journal of Geophysical Research - Solid Earth

Supporting information for

Backstress governs transient postseismic creep in the continental lithospheric mantle

Sheng Fan[1,2,3], Thomas Breithaupt[2], Claudia A. Trepmann[4], David Wallis[2]

[1]Center for High Pressure Science and Technology Advanced Research (HPSTAR), Beijing 100193, P. R. China

[2]Department of Earth Sciences, University of Cambridge, Cambridge CB2 3EQ, United Kingdom

[3]Department of Geology, University of Otago, Dunedin 9016, New Zealand

[4]Department of Earth and Environmental Sciences, Ludwig-Maximilians-Universität München, Munich 80333, Germany

Correspondence: Sheng Fan (sheng.fan@hpstar.ac.cn)

Contents

1. Description
2. Section S1 (Figures S1–S4)
3. Section S2 (Figures S14–S18)

Description

This supplementary material provides details of the electron backscatter diffraction (EBSD) datasets and processed high-angular resolution electron backscatter diffraction (HR-EBSD) data in Sections S1 and S2, respectively, for the different microstructural domains.

S1 Complete EBSD maps

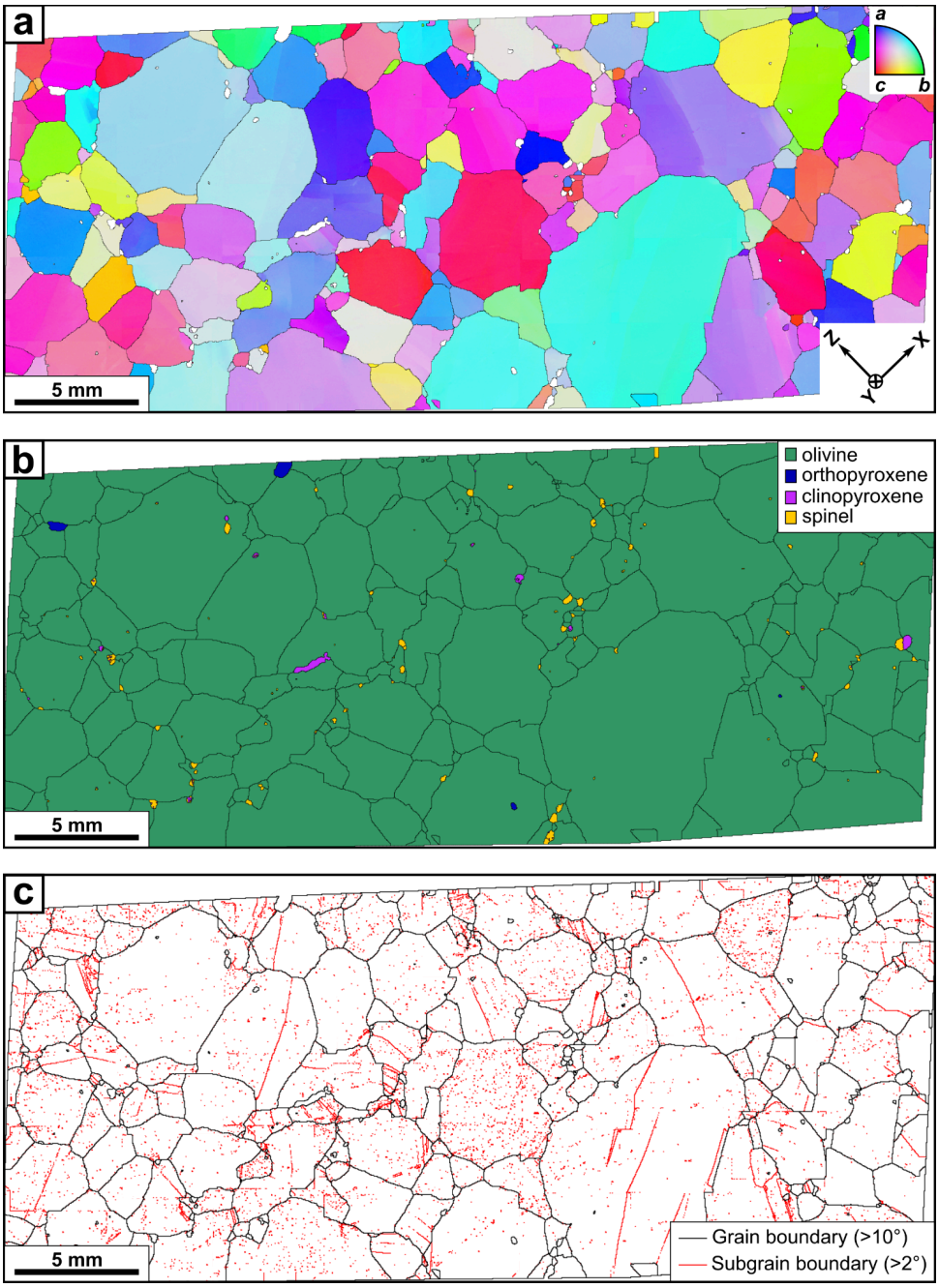

Figure S1. Complete microstructural maps of host rock. (**a**) Orientation map, in which the colour indicates the crystallographic direction (top right) that is parallel to the inferred Y-axis of the finite strain ellipsoid (indicated in the lower right). (**b**) Phase map. **(c)** Boundary map.

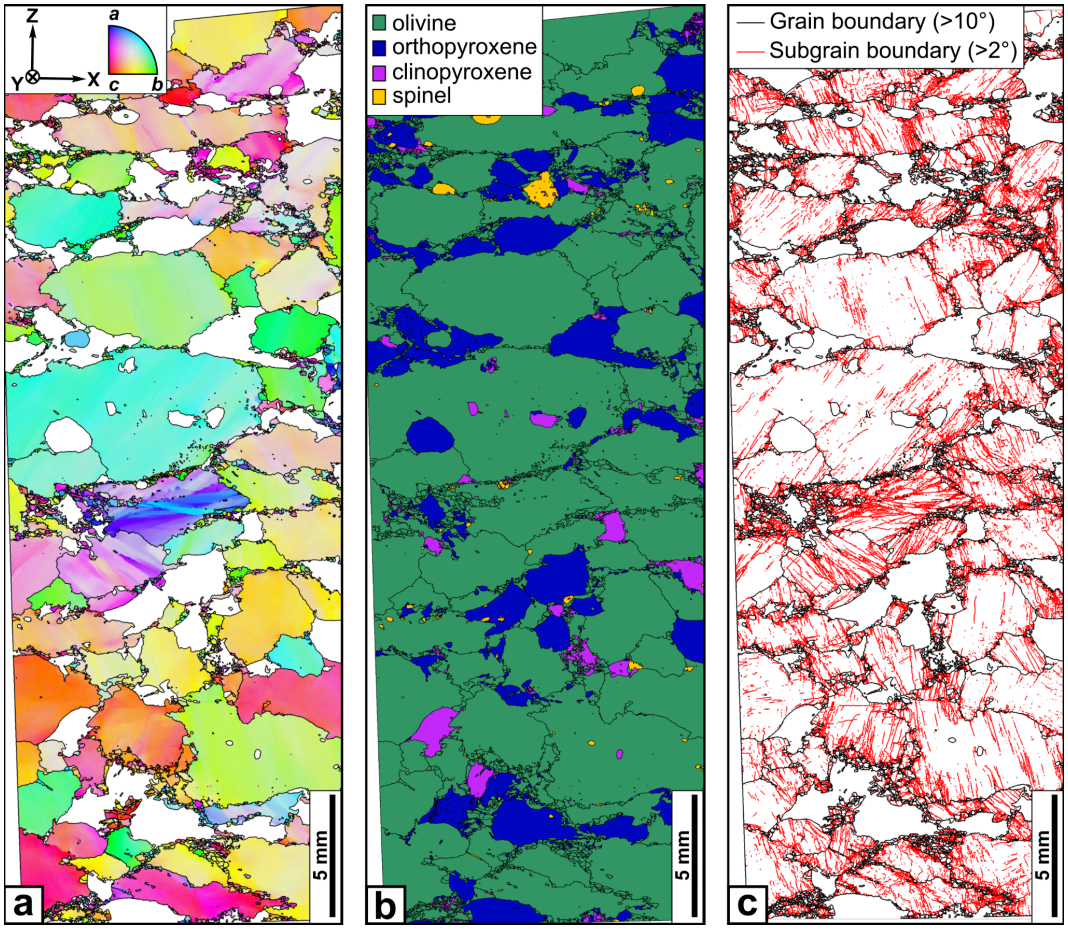

Figure S2. Complete microstructural maps of protomylonite. (**a**) Orientation map, in which the colour indicates the crystallographic direction (top left) that is parallel to the inferred Z-axis of the finite strain ellipsoid (indicated in the top left). (**b**) Phase map. **(c)** Boundary map.

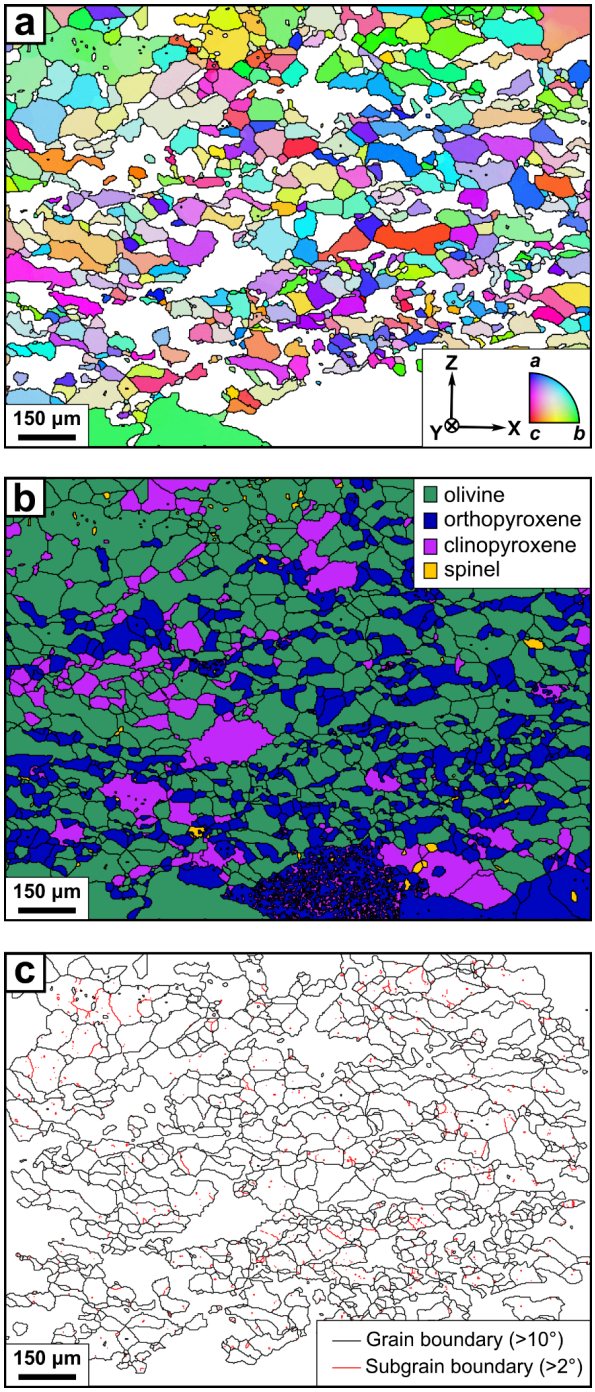

Figure S3. Complete microstructural maps of mylonite. (**a**) Orientation map, in which the colour indicates the crystallographic direction (bottom right) that is parallel to the inferred Z-axis of the finite strain ellipsoid (indicated in the bottom right). (**b**) Phase map. **(c)** Boundary map.

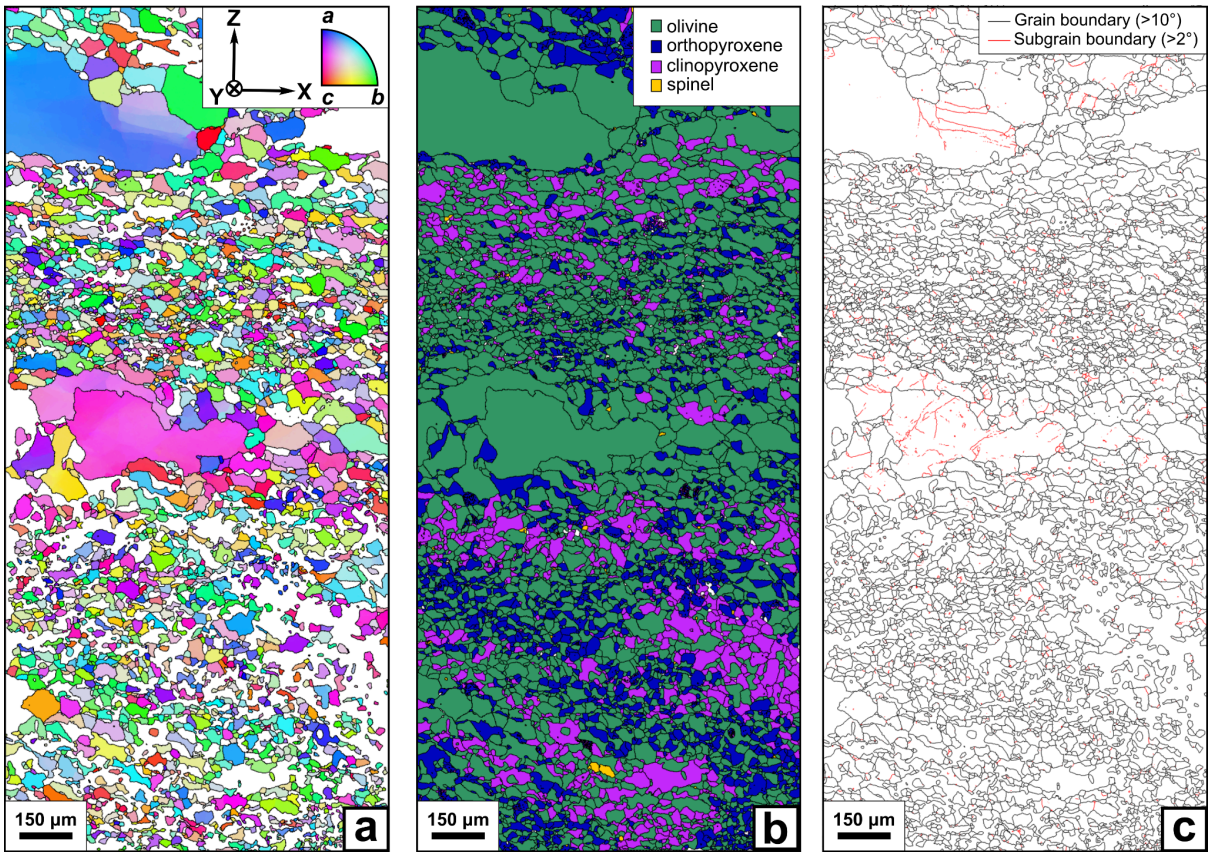

Figure S4. Complete microstructural maps of ultramylonite. (**a**) Orientation map, in which the colour indicates the crystallographic direction (top right) that is parallel to the inferred Z-axis of the finite strain ellipsoid (indicated in the top right). (**b**) Phase map. **(c)** Boundary map.

S2 HR-EBSD datasets

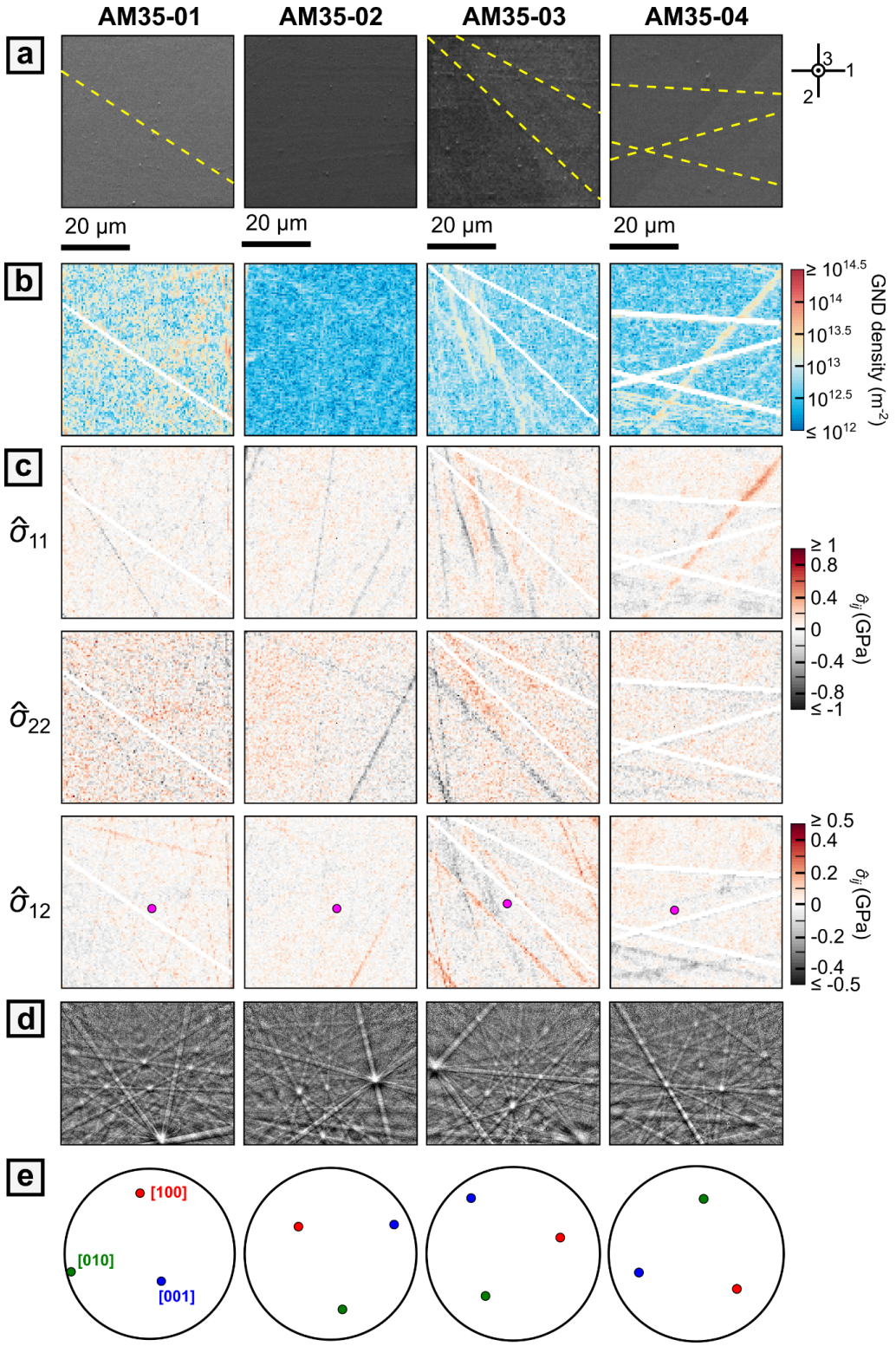

Figure S5. HR-EBSD data collected from the host rock. (**a**) Forescattered electron images. Dashed yellow lines indicate surface scratches with corresponding pixels removed from analyses. (**b**) The

logarithm of the total densities of geometrically necessary dislocations (GNDs) estimated from lattice rotations measured by HR-EBSD. (**c**) Maps of each component of the normalised residual stress tensors ($\hat{\sigma}_{11}$, $\hat{\sigma}_{22}$, and $\hat{\sigma}_{12}$) calculated by subtracting the mean value within each grain. In (**b**) and (**c**), white areas indicate pixels corresponding to surface scratches or pixels that failed the quality criteria for the cross-correlation analysis (Britton & Wilkinson, 2011); these pixels were removed from our analysis. (**d**) Raw diffraction patterns of the reference points marked by pink dots in (**c**). (**e**) Pole figures illustrating crystal orientations.

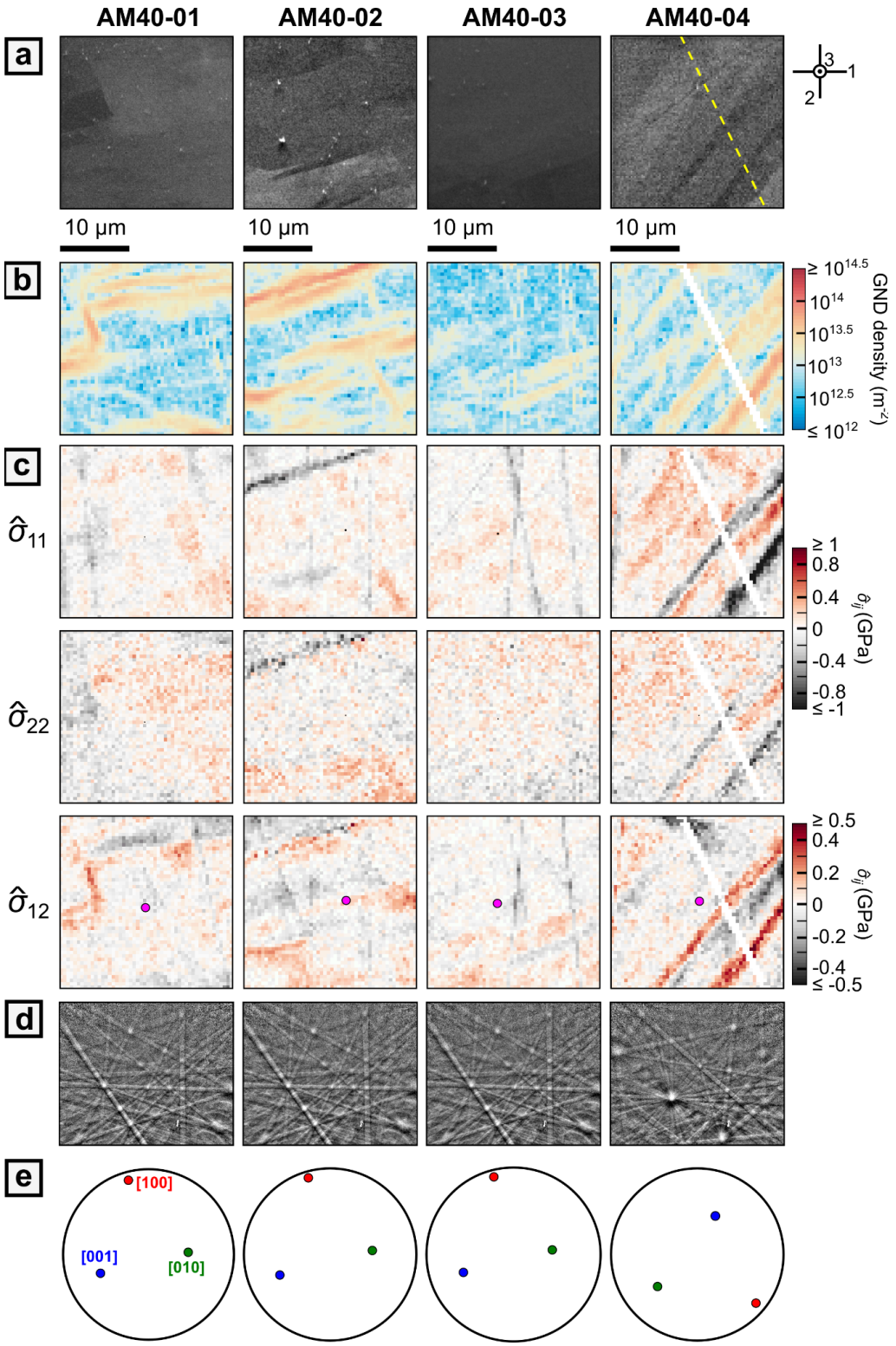

Figure S6. HR-EBSD data collected from the protomylonite. Descriptions of (**a**)–(**e**) are the same as Fig. S5.

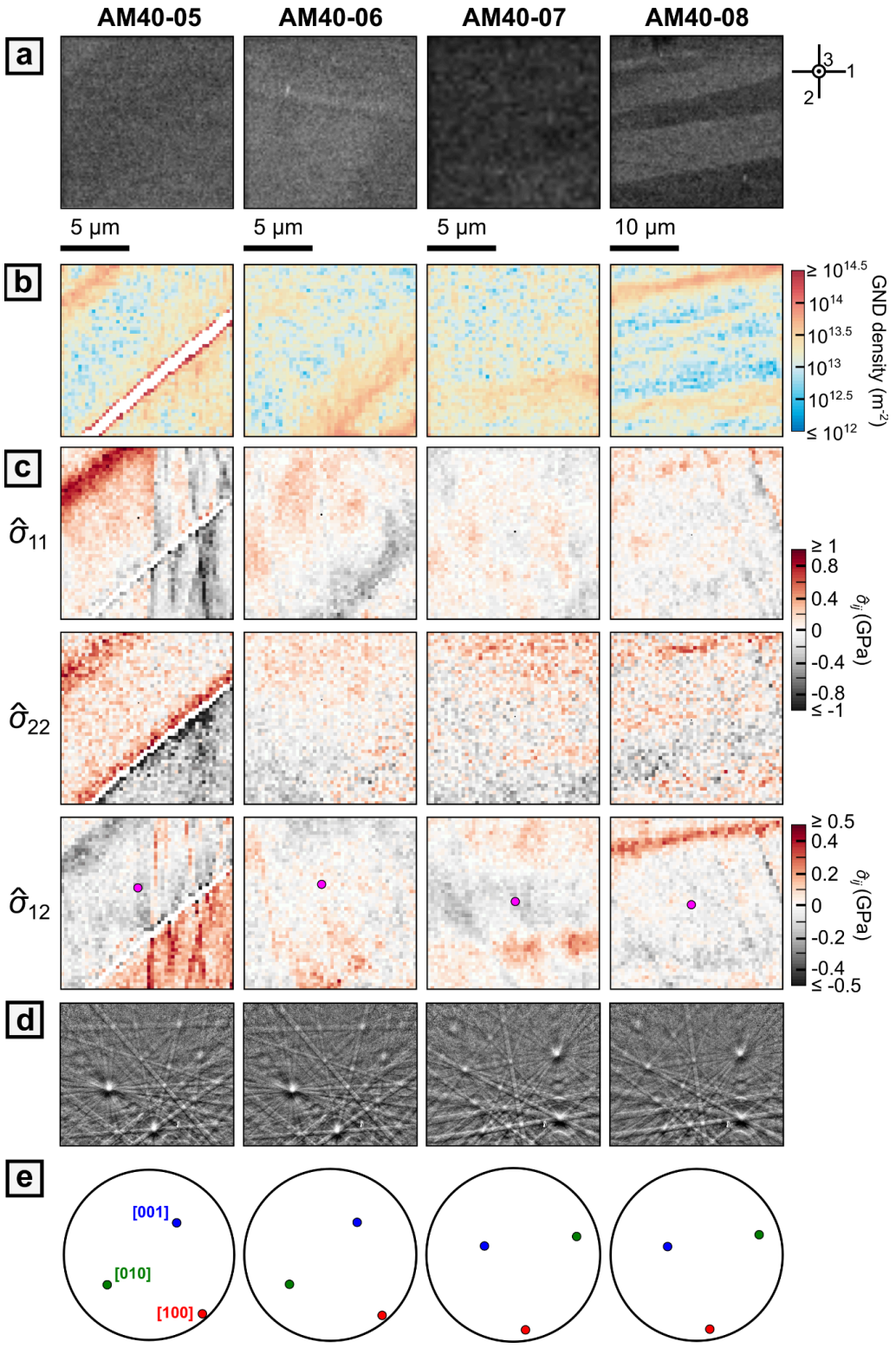

Figure S7. HR-EBSD data collected from the protomylonite. Descriptions of (**a**)–(**e**) are the same as Fig. S5.

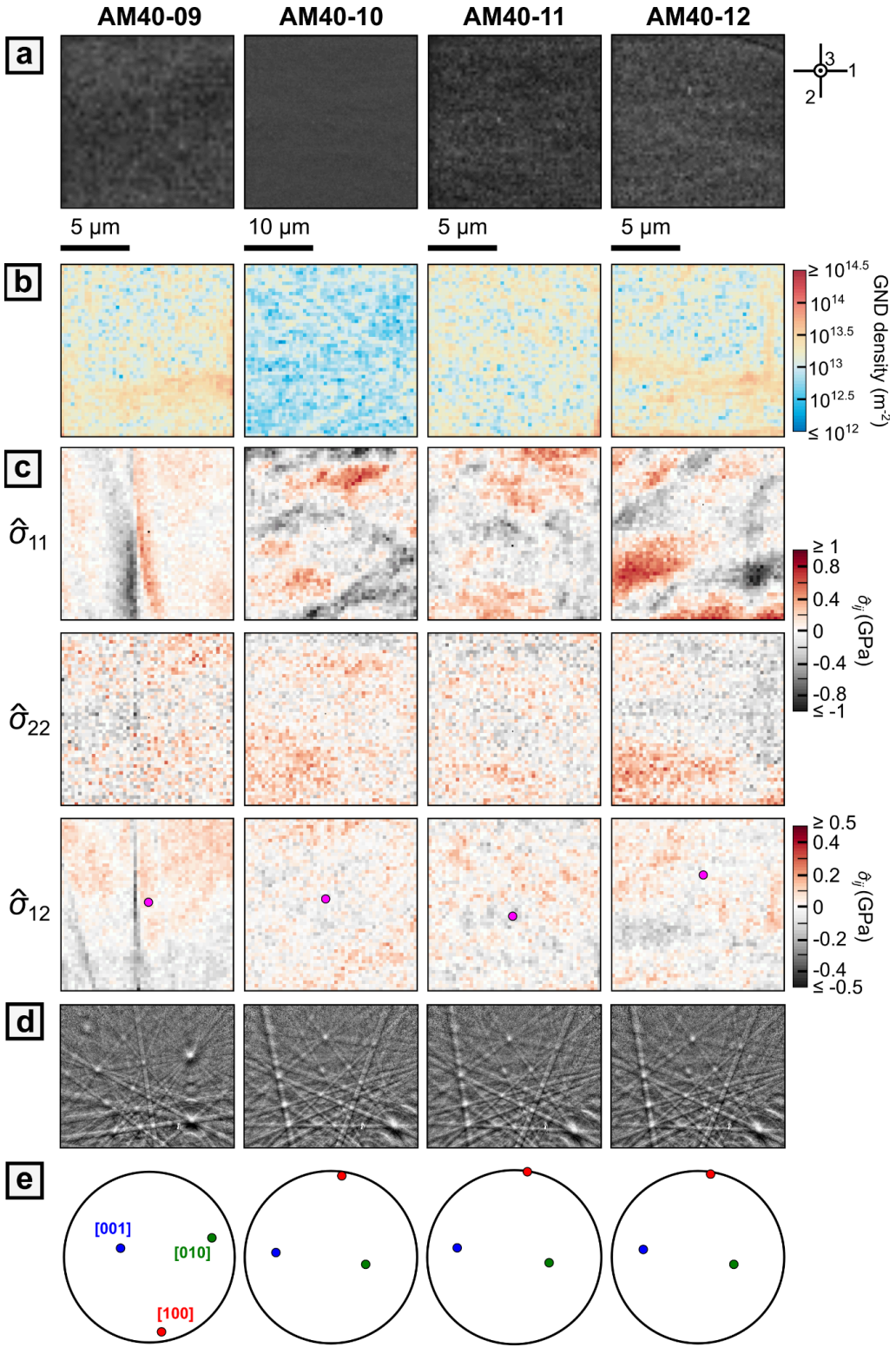
AM40-09
AM40-10
AM40-11
AM40-12
a
3
1
2
5 μm
10 μm
5 μm
5 μm
b
≥ 10^14.5
10^14
10^13.5
10^13
10^12.5
< 10^12
GND density (m^-2)
c
σ̂11
σ̂22
σ̂12
≥ 1
0.8
0.4
0
-0.4
-0.8
< -1
σ̂ij (GPa)
≥ 0.5
0.4
0.2
0
-0.2
-0.4
< -0.5
σ̂ij (GPa)
d
e
[001]
[010]
[100]

Figure S8. HR-EBSD data collected from the protomylonite. Descriptions of (**a**)–(**e**) are the same as Fig. S5.

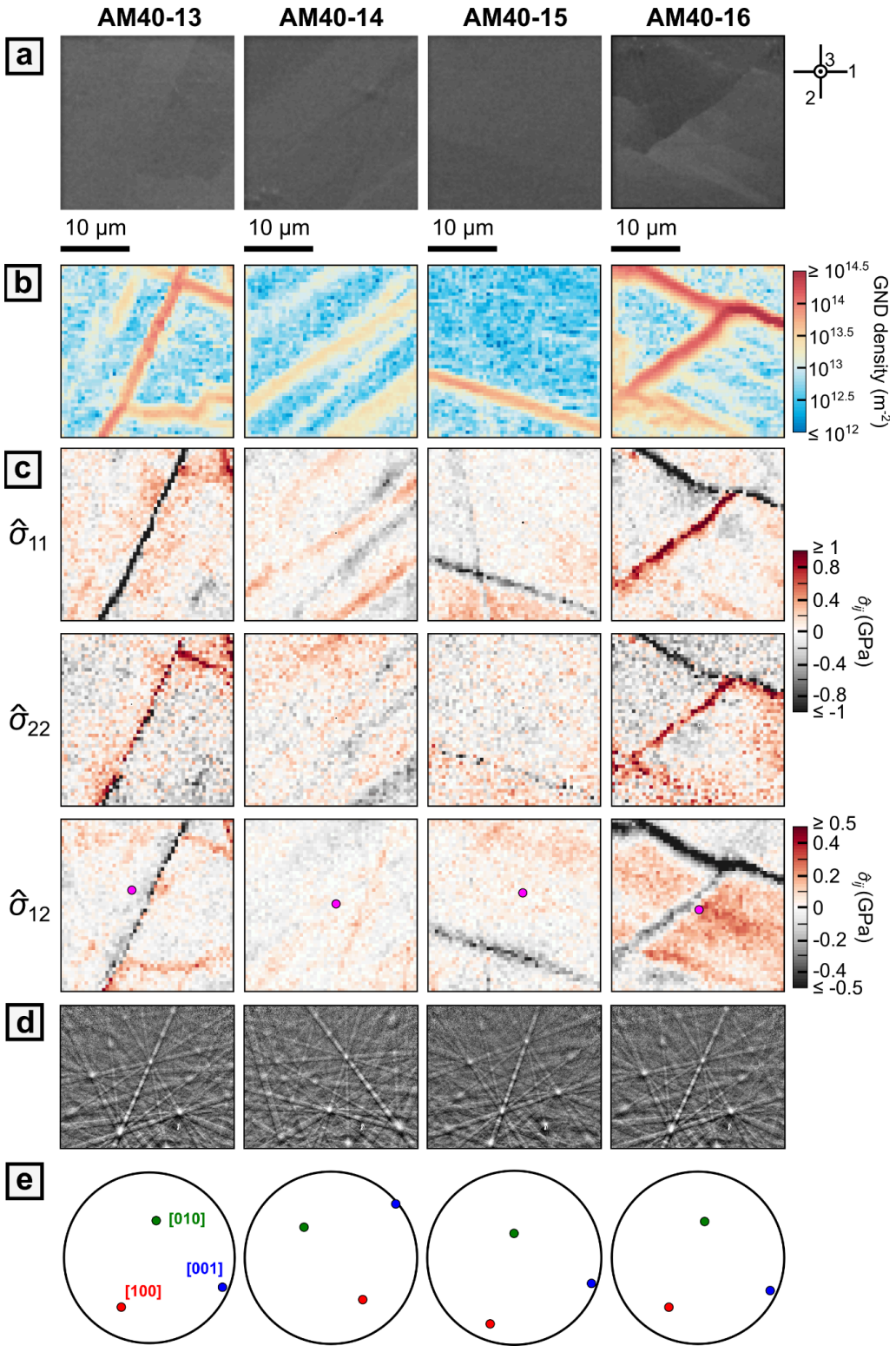

Figure S9. HR-EBSD data collected from the protomylonite. Descriptions of (**a**)–(**e**) are the same as Fig. S5.

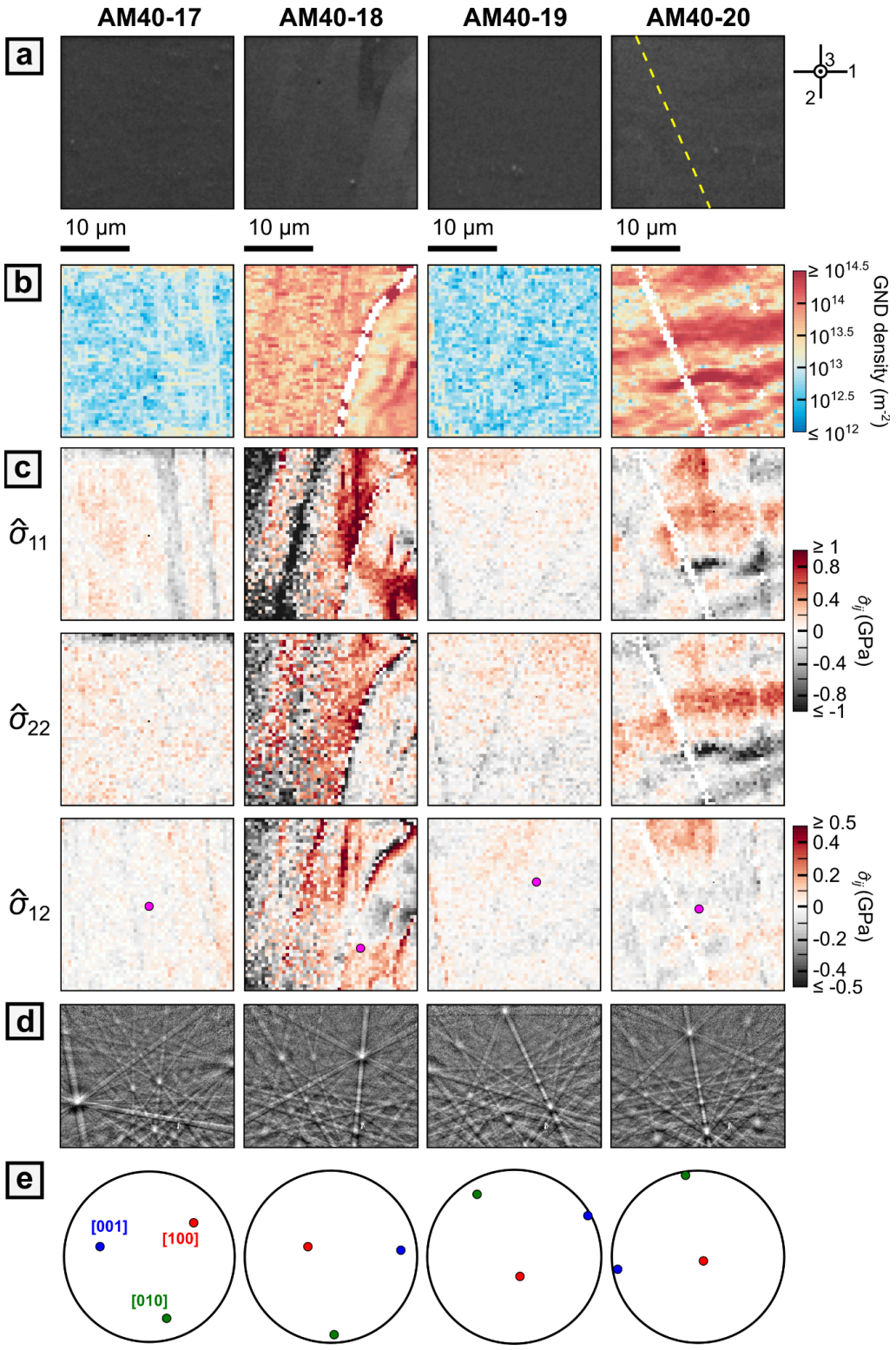

Figure S10. HR-EBSD data collected from the protomylonite. Descriptions of (**a**)–(**e**) are the same as Fig. S5.

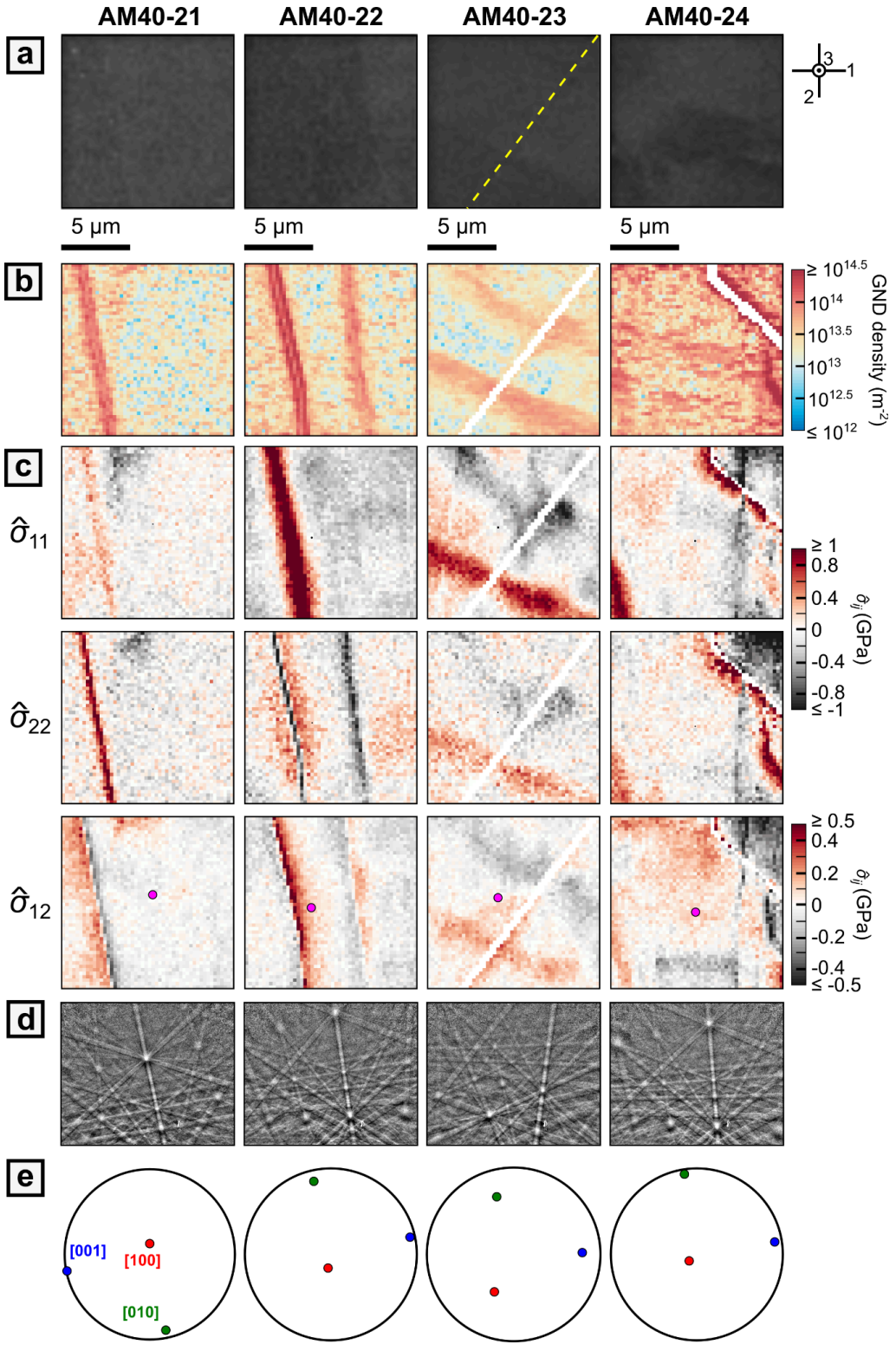

Figure S11. HR-EBSD data collected from the protomylonite. Descriptions of (**a**)–(**e**) are the same as Fig. S5.

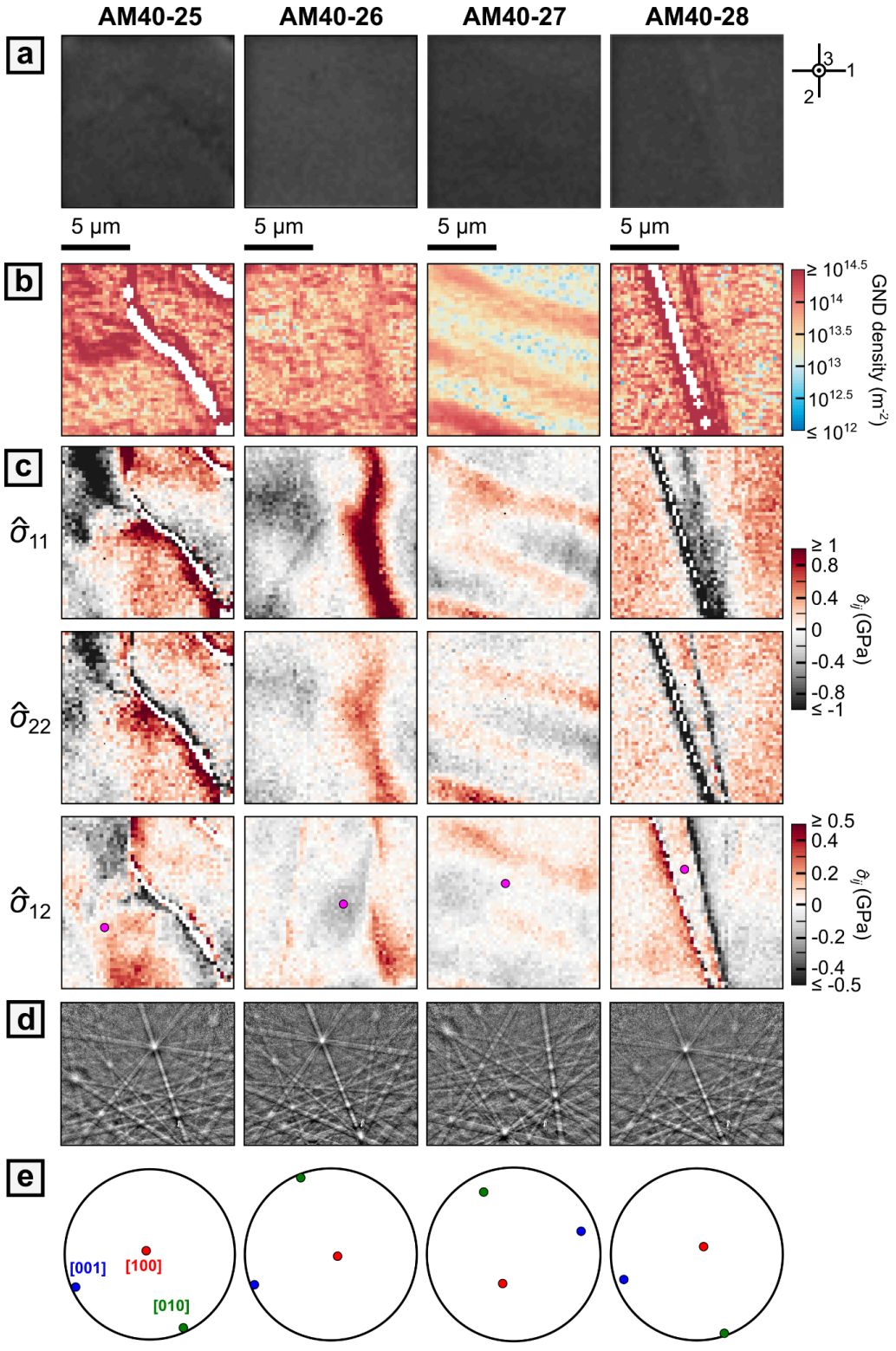

Figure S12. HR-EBSD data collected from the protomylonite. Descriptions of (**a**)–(**e**) are the same as Fig. S5.

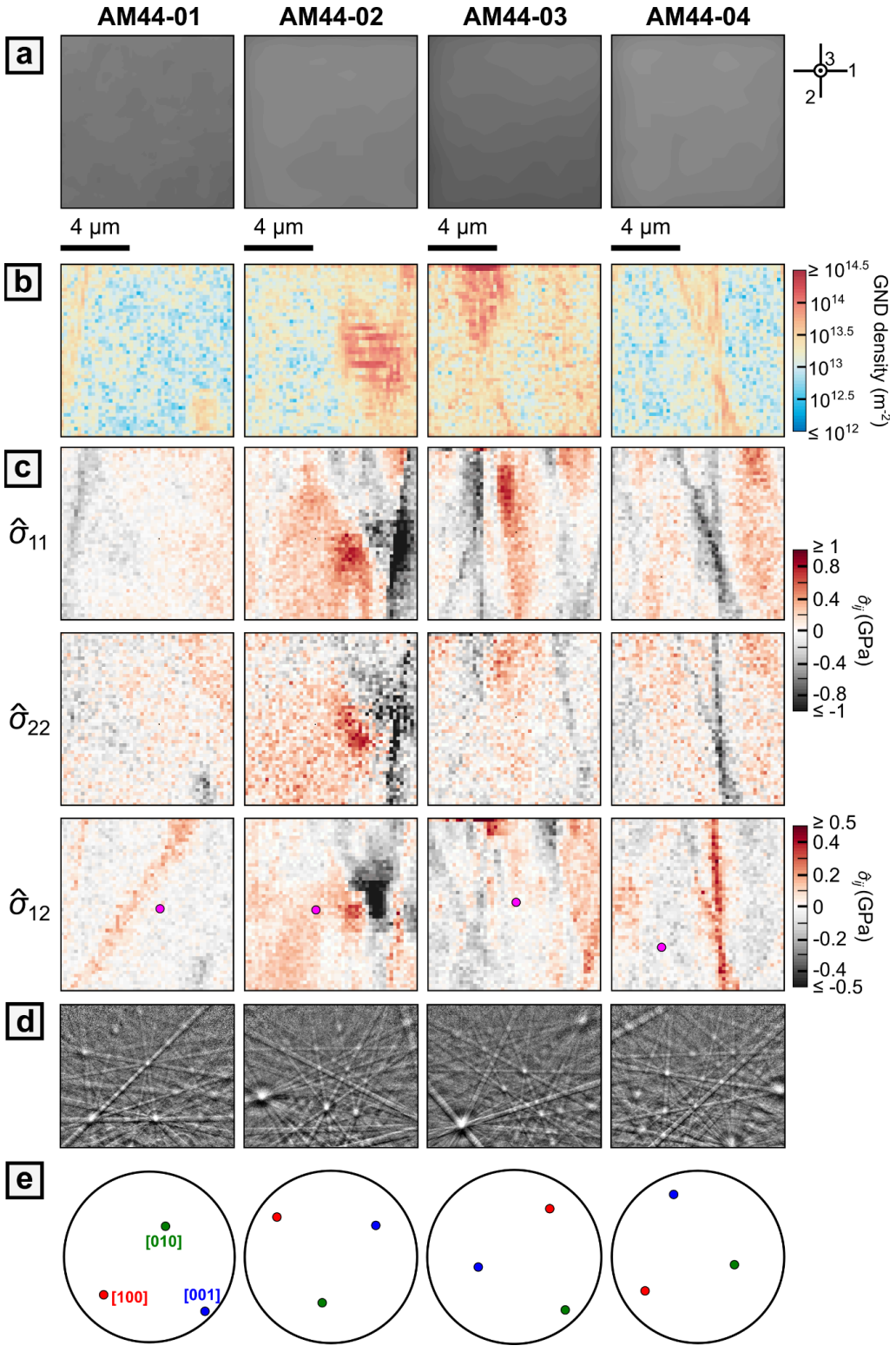

Figure S13. HR-EBSD data collected from the mylonite. Descriptions of (**a**)–(**e**) are the same as Fig. S5.

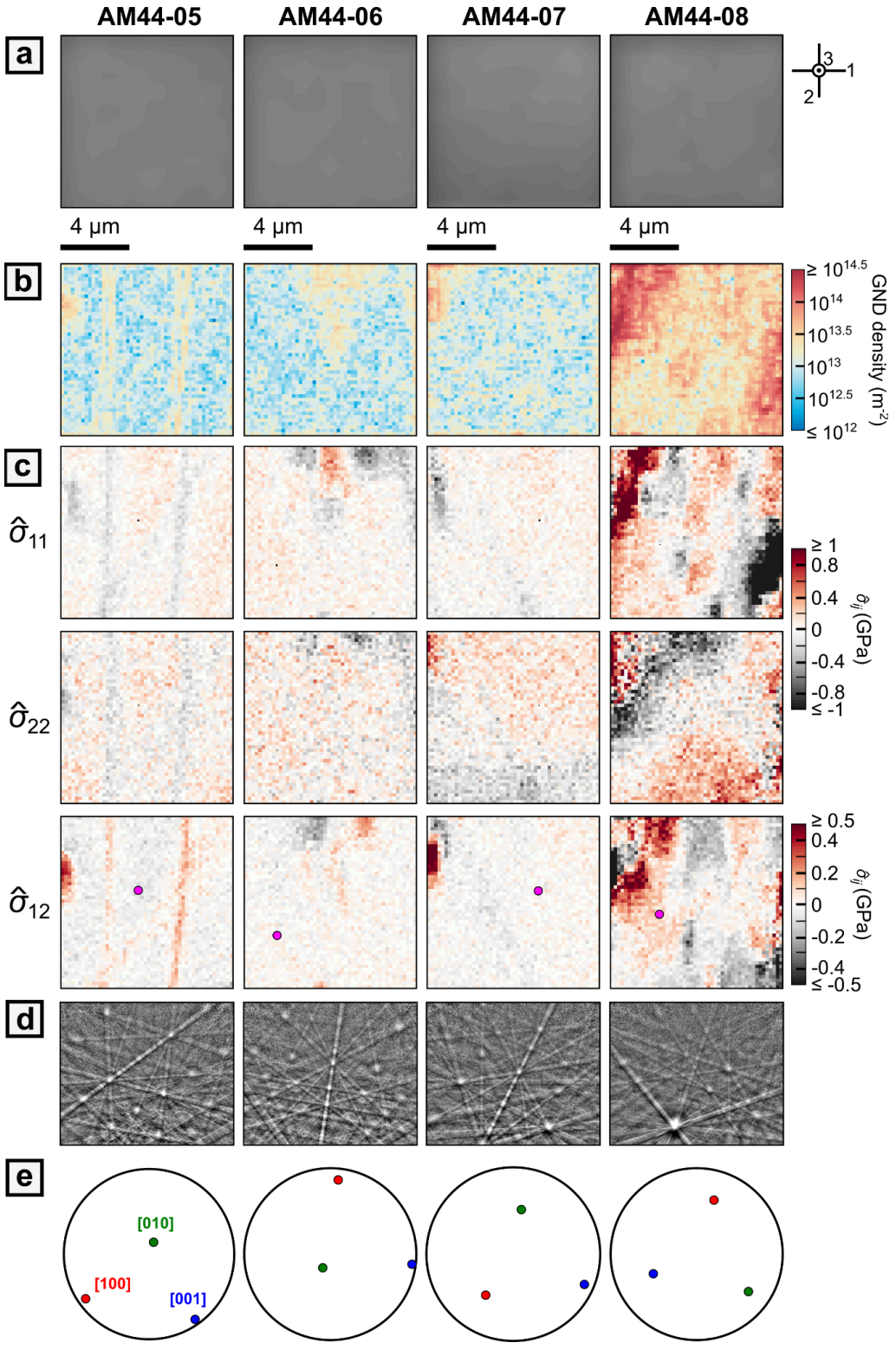

Figure S14. HR-EBSD data collected from the mylonite. Descriptions of (**a**)–(**e**) are the same as Fig. S5.

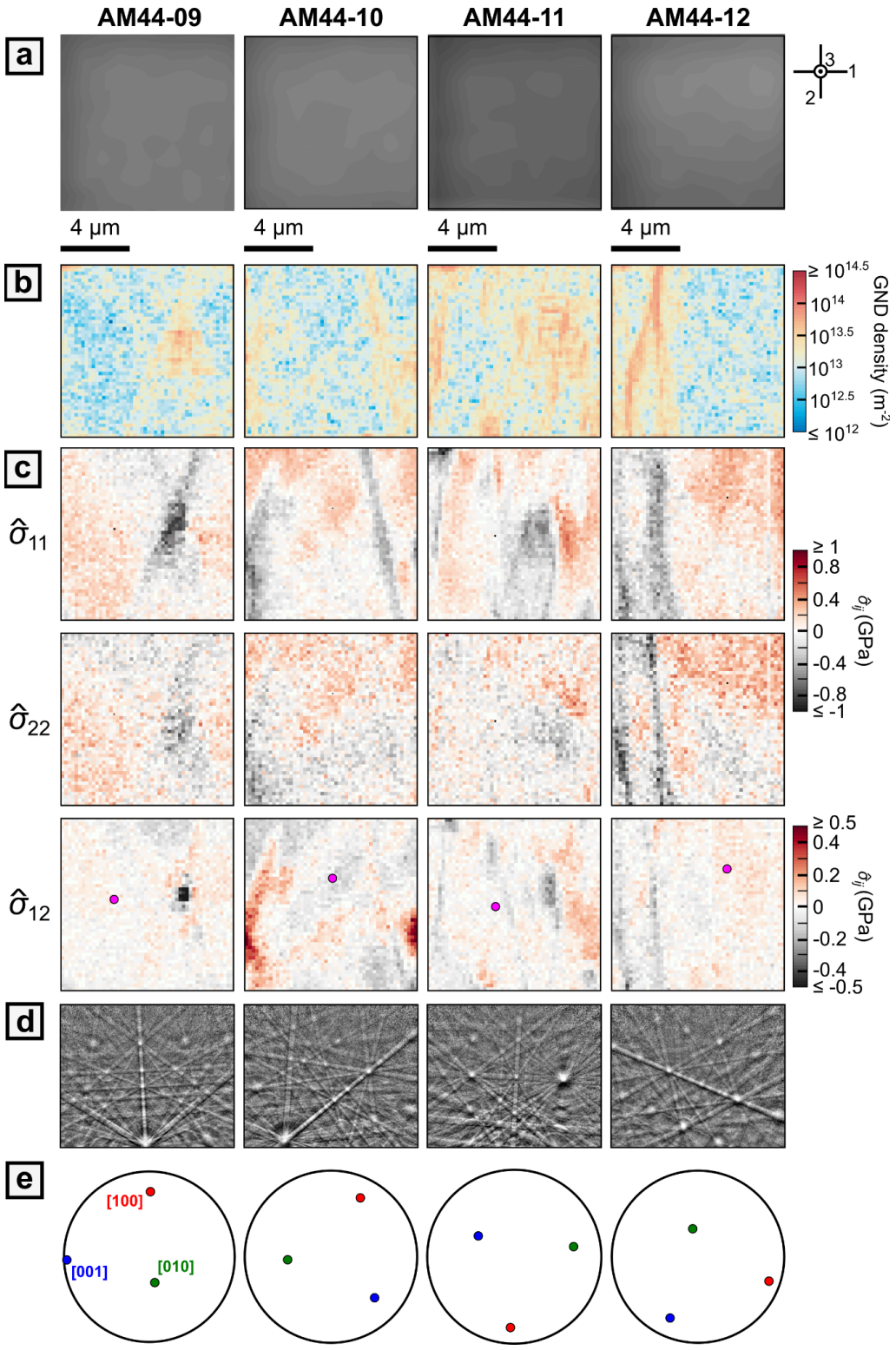

Figure S15. HR-EBSD data collected from the mylonite. Descriptions of (**a**)–(**e**) are the same as Fig. S5.

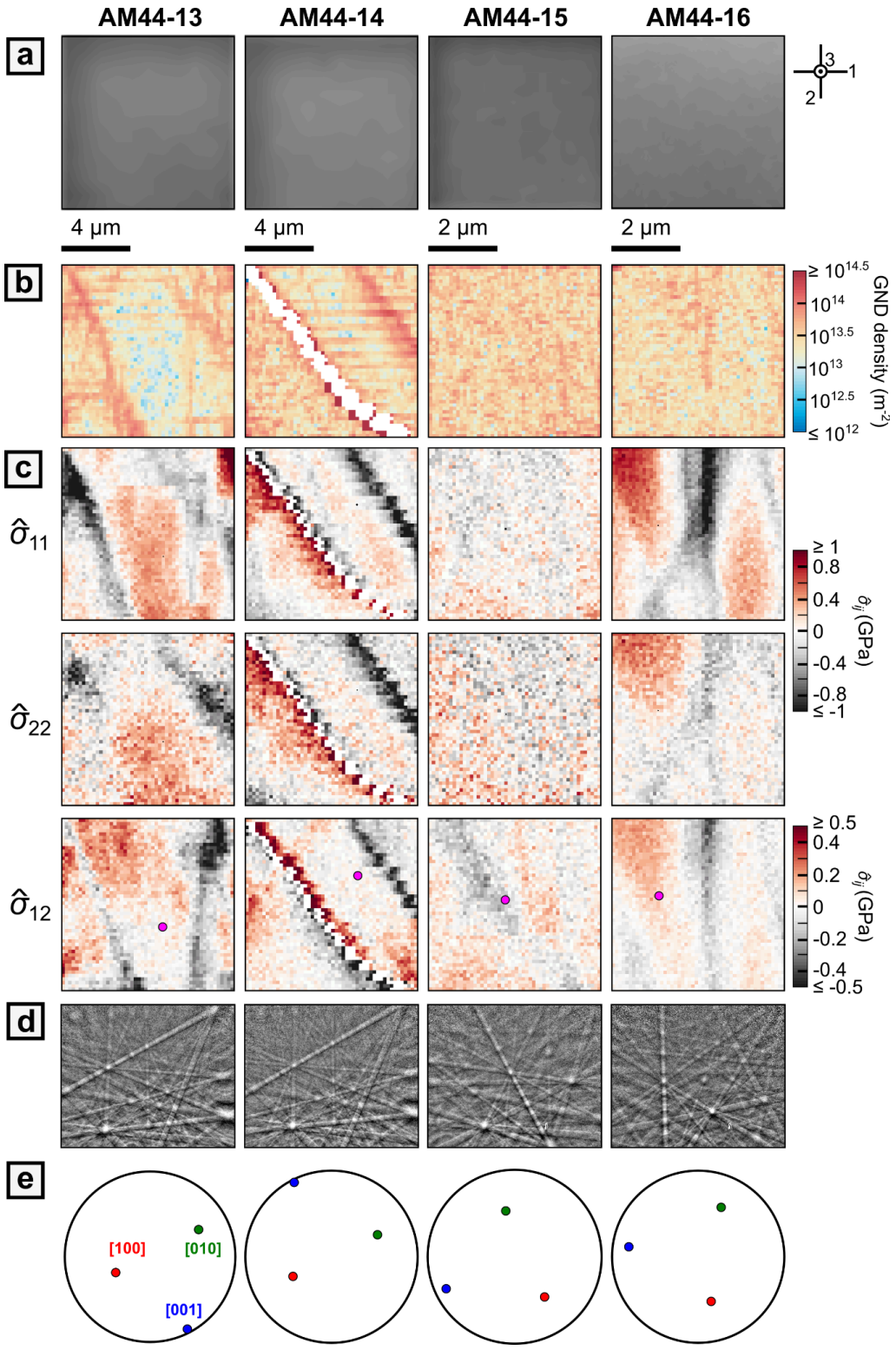

Figure S16. HR-EBSD data collected from the mylonite (AM44-13 and AM44-14) and the ultramylonite (AM44-15 and AM44-16). Descriptions of (**a**)–(**e**) are the same as Fig. S5.

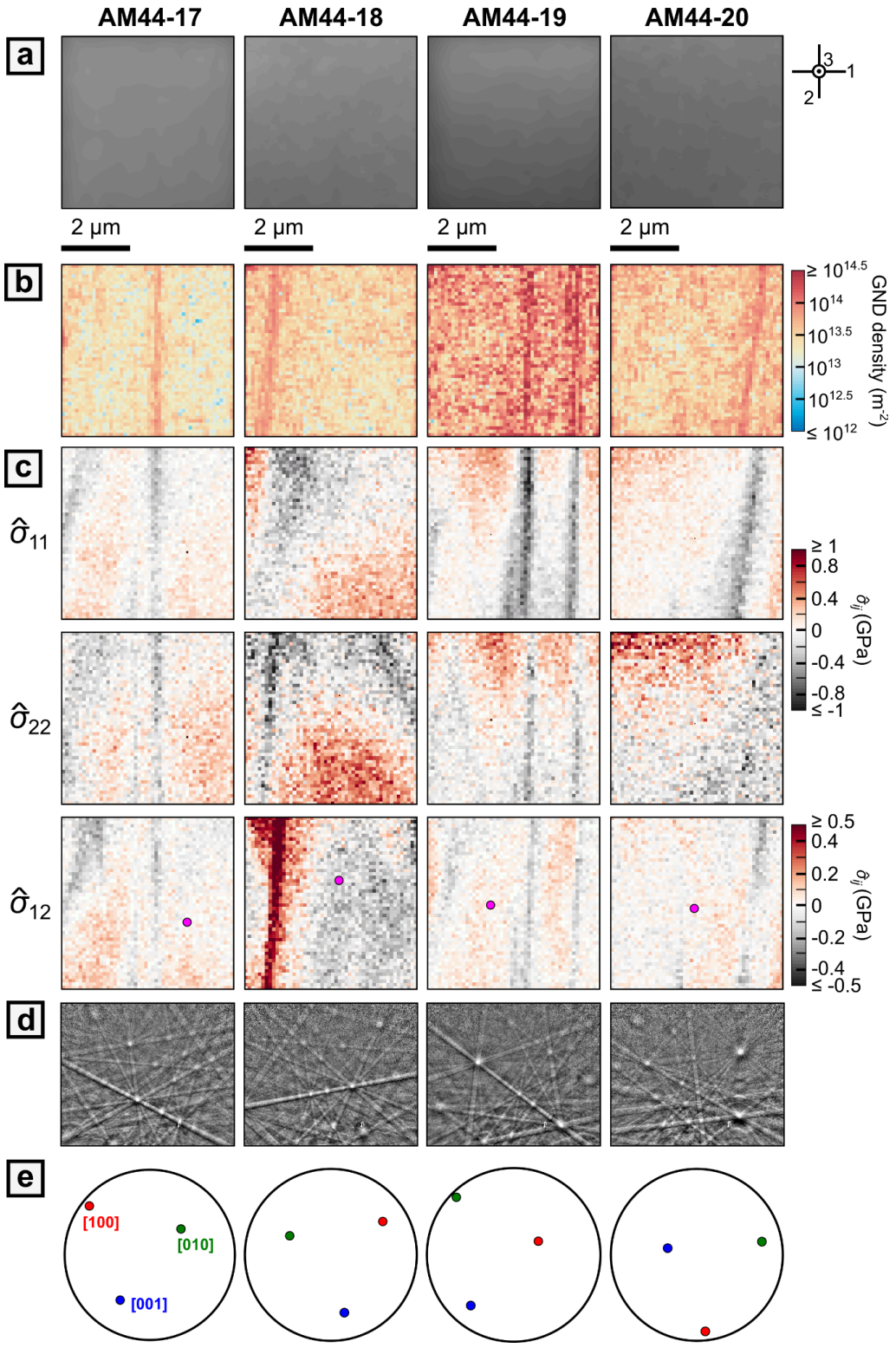

Figure S17. HR-EBSD data collected from the ultramylonite. Descriptions of (**a**)–(**e**) are the same as Fig. S5.

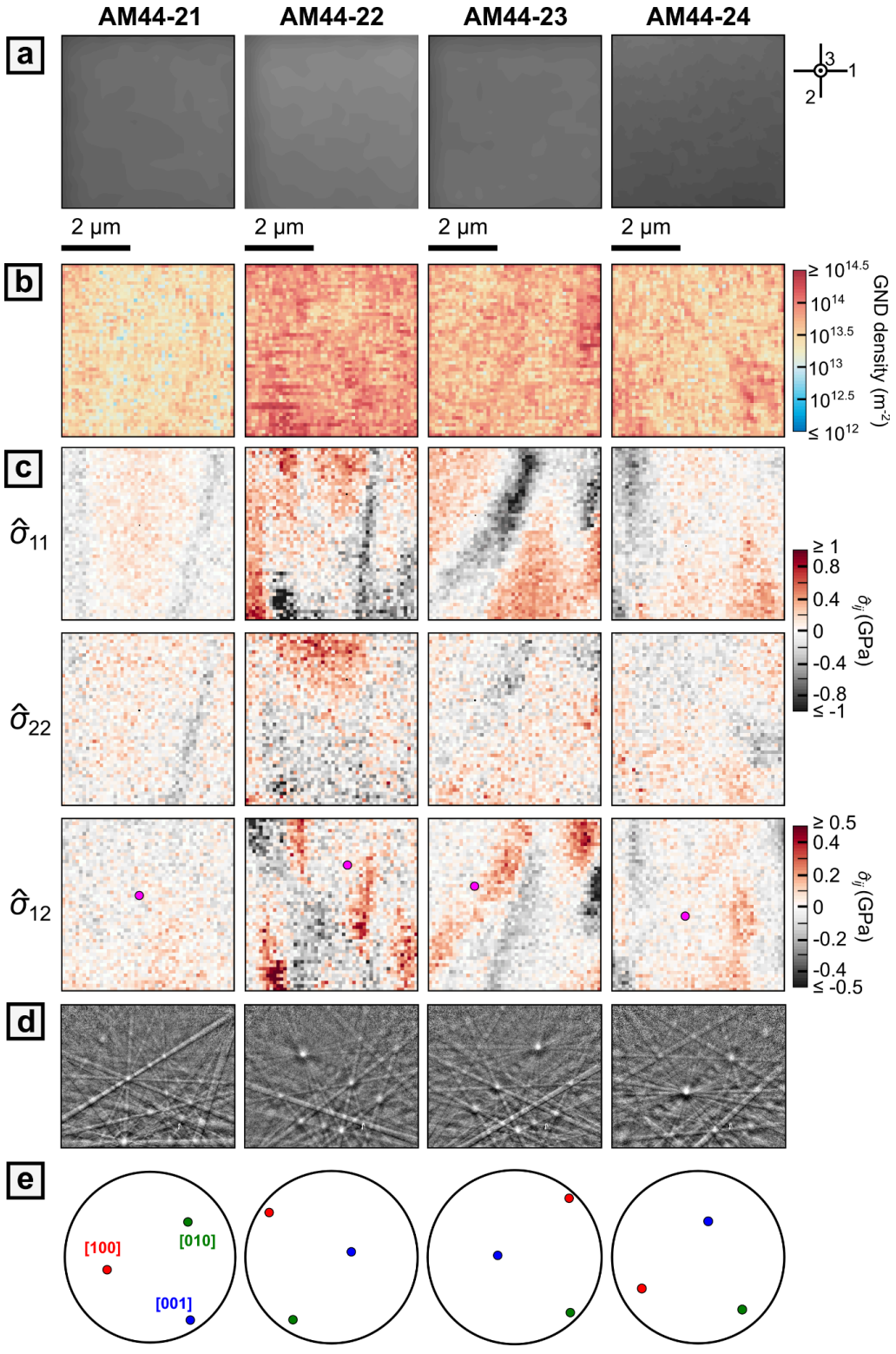

Figure S18. HR-EBSD data collected from the ultramylonite. Descriptions of (**a**)–(**e**) are the same as Fig. S5.

Reference

Britton, T. B., & Wilkinson, A. J. (2011). Measurement of residual elastic strain and lattice rotations with high resolution electron backscatter diffraction. *Ultramicroscopy*, *111*(8), 1395–1404. https://doi.org/10.1016/j.ultramic.2011.05.007